CORNELIA BAYER

About the Improvement of High Capacity Silicon Anodes for Lithium-Ion Batteries

---

Doctoral Thesis

Submitted in fulfillment for doctors degree of technical science

at

Graz University of Technology

Institute for Chemistry and Technology of Materials

2011

Deutsche Fassung:

Beschluss der Curricula-Kommission für Bachelor-, Master- und Diplomstudien vom 10.11.2008

Genehmigung des Senates am 1.12.2008

Eidesstattliche Erklärung

Ich erkläre an Eides statt, dass ich die vorliegende Arbeit selbstständig verfasst, andere als die angegebenen Quellen/Hilfsmittel nicht benutzt, und die den benutzten Quellen wörtlich und inhaltlich entnommene Stellen als solche kenntlich gemacht habe.

Graz, am …… ……..

(Unterschrift)

Englische Fassung:

Statutory Declaration

I declare that I have authored this thesis independently, that I have not used other than the declared sources/resources, and that I have explicitly marked all material which has been quoted either literally or by content from the used sources.

…… ……..

(date) (signature)

Acknowledgement

First of all, I would like to express my gratitude to my supervisor Univ.-Prof. Dipl.-Ing. Dr.techn. Franz Stelzer for his guidance and support during my graduate studies.

I also want to thank Dipl.-Ing. Dr.techn. Stefan Koller for his untiring effort, guidance and support, the numerous discussions and his tireless patience.

A special thank goes to "MAGNA Steyr" and "Varta Micro Innovation" for the financial support of this thesis. Sincere thanks especially to Dipl.-Ing. Dr.techn. Nikolaus Hochgatterer and Dipl.-Ing. Heimo Kreimaier from "MAGNA Steyr" and Dipl.-Ing. Christoph Stangl and Dipl.-Ing. Dr.techn. Harald Kren from "Varta Micro Innovation" for their kind and helpful support.

Also particular thanks to Johann Schlegl and Ao.Univ.-Prof. Dipl.-Ing. Dr.techn. Franz Mautner for his capable objections and his tireless patience.

Special thanks also to Dr.techn. Mihaela Albu from the Austrian Centre for Microscopy and Nanoanalysis (FELMI-ZFE) for her kind and helpful support.

I am also greatly appreciative of all people, who took part in my daily research/working life: Andrea Droisner, Katharina Gruber, Dipl.-Ing. BSc Laura Kaltenböck, MSc Sandra Pötz, Dipl.-Ing. Dr.techn. Barbara Rupp, Dipl.-Ing. BSc Michaela Scharfegger, Liane Hochgatterer, Manuela Pögl, Mathilde Frießnegg, Margaretha Maierhofer, Rosina Kerschbaumer, Angela Hampl, Christina Albering, Diana Cujez, Stephania Toulis, Dipl.-Ing. Dr.techn. Martin Schmuck, Dipl.-Ing. Dr. techn. Bernd Fuchsbichler, Dipl.-Ing. Dr.techn. Michael Sternad.

Last but certainly not least I would like to thank my whole family and my friends for listening of several hours, for all good advice, for their patience and for the fact that they were always there for me. Especially, I would like to thank Dipl.-Ing. Colin God, my parents and my grandparents for the fact that my luck is an essential component of their own luck.

Abstract

In general, electrodes for lithium-ion batteries consist of an electrochemical active material, an additive to improve conductivity, a binder and a current collector.

In commercial lithium-ion batteries the widely used anode active materials are carbonaceous materials, especially graphite. A serious disadvantage of graphite is the relatively low theoretical specific capacity of 372 $mAh \cdot g^{-1}$ (LiC_6). In contrast, silicon shows a nearly ten times higher theoretical specific capacity of 4199 $mAh \cdot g^{-1}$ ($Li_{22}Si_5$) and constitutes for that reason one of the most attractive anode materials for lithium-ion batteries. Furthermore, silicon is also abundant, cheap and environmentally benign. But apart from all of these advantages the insertion/removal of lithium into/from silicon is associated with tremendous volume changes of the host matrix. To improve the electrochemical performance nano-scaled silicon powders, so called silicon/graphite composite materials and alternative binder systems were applied so far, but the high irreversible capacity in the first cycle and the bad cycling stability, especially by using very pure silicon, are unfavorable. Beyond that, the use of alternative binders implicates new problems, like for example the increasing brittleness of the electrodes and, thus, a difficult commercial manufacturing.

On the one hand, with the contribution of hetero-atoms into the pure nano-scaled silicon powder, like for example elements of the first and second main group, it was possible to enhance the electrochemical performance of silicon electrodes. The electrodes made out of the preliminary fractional alloyed silicon shows improved electrochemical properties, like higher specific charge and discharge capacities.

On the other hand, by the use of plasticizers during the electrode-paste preparation an improvement in the mechanical stability and, thus, a simplification of the electrode processing were attained.

Kurzfassung

Im Allgemeinen bestehen Elektroden für Lithium-Ionen Batterien aus einem elektrochemisch aktiven Material, einem Additiv zur Erhöhung der Leitfähigkeit, einem Binder und einem Stromsammler.

In kommerziellen Lithium-Ionen Batterien stellen kohlenstoffartige Materialien, insbesondere Graphit, die meist genutzten Anodenaktivmaterial dar. Einer der Hauptnachteile des Graphits ist die relativ niedrige theoretische spezifische Kapazität von 372 $mAh \cdot g^{-1}$ (LiC_6). Im Gegensatz dazu, weist Silizium eine rund zehnmal höhere theoretische spezifische Kapazität von rund 4199 $mAh \cdot g^{-1}$ ($Li_{22}Si_5$) auf und stellt somit eine attraktive Alternative als Anodenaktivmaterial dar. Darüber hinaus ist Silizium in reichlichen Mengen vorhanden, es ist preiswert und auch nicht als umweltbedenkliches Material einzustufen. Aber, abgesehen von all diesen Vorteilen, geht die Insertion bzw. Extraktion des Lithiums in bzw. aus Silizium mit enormen Volumenänderungen der Wirtsmatrix einher. Um das elektrochemische Verhalten zu verbessern wurden bisweilen nano-strukturierte Silizium Pulver, so genannte Silizium/Graphit Komposit-Materialien und alternative Binder Systeme eingeführt, aber die hohe irreversible Kapazität in den ersten Zyklen und die daraus resultierende schlechte Effizienz in den Folgezyklen, sowie die schlechte Zyklenstabilität, insbesondere bei der Verwendung von hochreinem Silizium, stellen nach wie vor ein großes Problem dar. Weiters bringt die Verwendung von alternativen Bindersystemen neue Probleme, wie zum Beispiel eine erhöhte Sprödheit der Elektrode und somit eine erschwerte großtechnische Herstellung, mit sich.

Auf der einen Seite war es möglich durch das Einbringen von Hetero-Atomen in das hochreine nano-teilige Silizium Pulver, wie zum Beispiel Elemente der ersten und zweiten Hauptgruppe, eine Verbesserung des elektrochemischen Verhaltens von Silizium Elektroden zu bewirken. Die aus diesem partiell vorablegierten Silizium hergestellten Elektroden zeigten verbesserte elektrochemische Eigenschaften, wie eine höhere spezifische Lade- und Entladekapazität. Auf der anderen Seite konnte durch die Verwendung eines Weichmachers während der Elektrodenpasten-Präparation eine Verbesserung der mechanischen Stabilität und somit eine Vereinfachung der Weiterverarbeitung der Elektrode erzielt werden.

Table of Contents

Table of Figures

List of Tables

1 Introduction

The steadily increasing global requirement on energy, CO_2-emmission directives and the limited supply on fossil fuels lead to a growing demand on alternative, renewable energy sources, such as solar energy, wind power, hydro power and biomass-derived energy. Unfortunately, these renewable sources provide an inherent intermittent energy supply and an immediate provision of energy to the demand is not possible. For that reason the topic “energy storage” becomes of increasing importance. In this connection the lithium-ion battery technology turns out to be a key technology in the range of energy storage.

Lithium-ion batteries are already steady companions in our daily life´s - they can be found in most of the portable electronic devices, like mobile phones, laptops and digital cameras. Lithium-ion batteries show compared to other secondary battery systems several advantages, like a higher energy density (Figure 1), higher operating voltages, lower self discharge and a good cycleability.

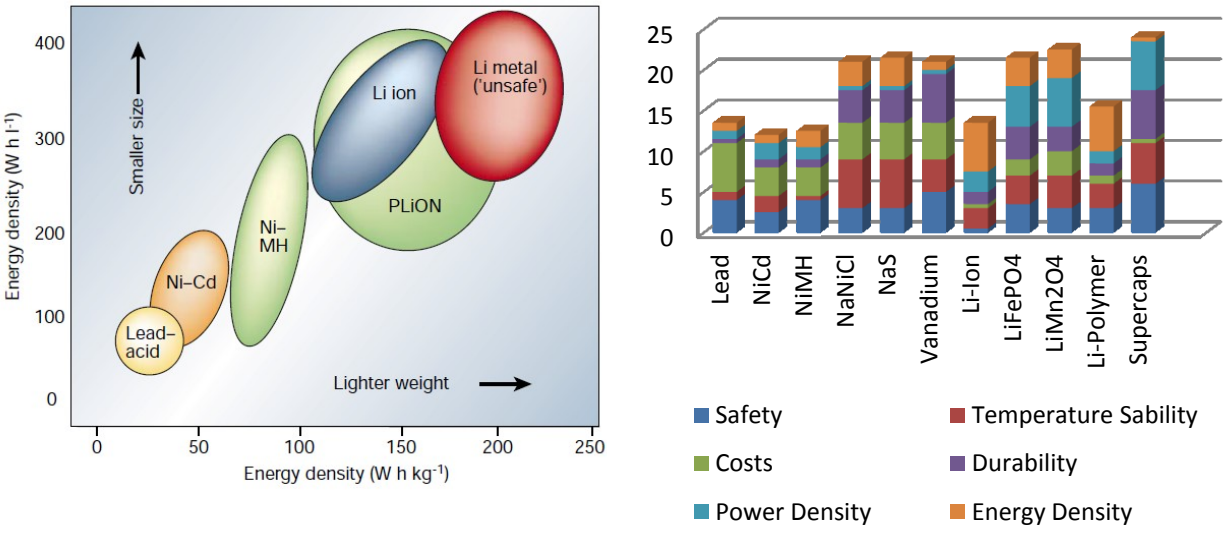

Figure 1: Comparison of different secondary battery systems[(1),(2)]

Furthermore, they can be manufactured in a flexible and lightweight design and among the other benefits of this system especially this fact makes them also attractive for the application in the field of electro-mobility. In this regard designated political targets in terms of fossil oil autonomy and the reduction of emissions of the daily traffic can be achieved. Currently, so called hybrid electric vehicles (HEV; a combination between a combustion engine and an electro-drive train) as well as electric vehicles (EV) are developed by the automotive industry.

But to get comparable ranges to the combustion engine a specific energy of around 1500 Wh·kg^{-1} would be necessary. Current lithium-ion batteries provide an average specific energy of 160 Wh·kg^{-1} (Figure 2)[3].

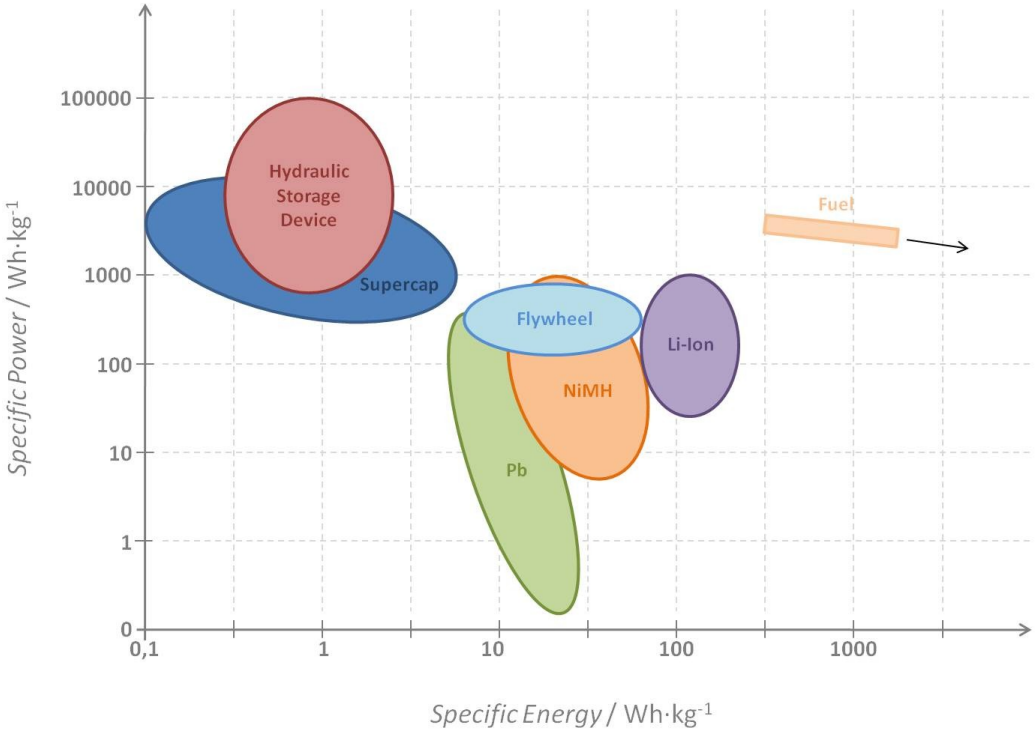

Figure 2: Comparison of specific energy and specific power of several energy storage systems[4]

Hence, to enlarge the energy densities of a lithium-ion battery and to overcome the growing performance demands in the different fields of application it is necessary to make further improvements.

The capacity of a lithium-ion cell depends on the capacity of the cathode as well as on the capacity of the anode. Kasavajjula et al. reported that the whole cell capacity increases until the anode reaches a specific capacity of 1200 mAh·g^{-1}, whereby the current cathode capacity limit is about 140-200 mAh·g^{-1} (Figure 3)[5].

In other words it is desirable to replace the common carbonaceous anode materials with anodes, which are able to offer capacities of around 1200 mAh·g^{-1}. In this connection silicon with a theoretical specific capacity of 4199 mAh·g^{-1} is the most attractive candidate as anode material for prospective lithium-ion batteries. Unfortunately, the lithiation and delithiation of silicon comes along with enormous volume changes, which induce a disintegration of the active material particles and subsequent a loss of contact to the ionic and electric conductor occurs. As a result a significant capacity fading during the cycling of the electrode is observable.

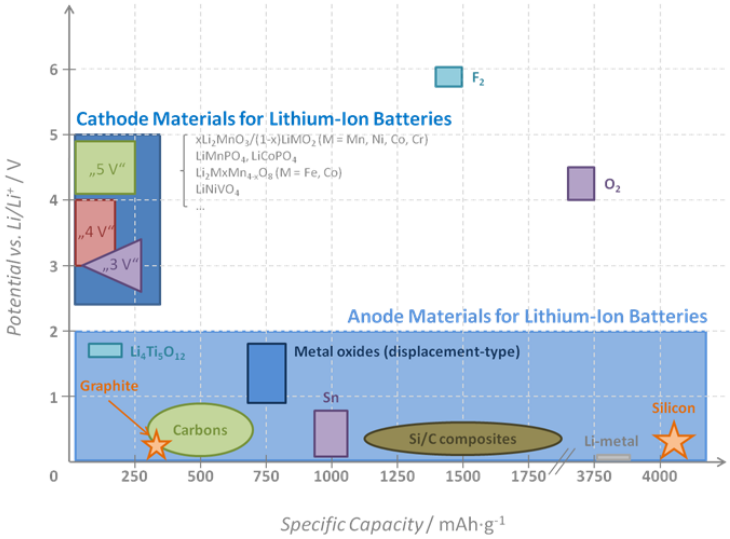

Figure 3: Potential vs. capacity diagram of different electrode materials

A further problem in the range of silicon anodes constitutes the desirable aqueous electrode processing with cellulose based binders. The silicon electrode shows an unfavorable brittleness after the drying steps and, thus, a further processing of the electrode is difficult due to their mechanical instability.

The present work focuses on the advancement of silicon anodes by treatment of pure nano-scaled silicon materials as well as by variation of the electrode preparation technique. Thus, the reader can expect, besides a general introduction to the world of (lithium-ion) batteries, two experimental parts. Figure 4 should illustrate the content of these two experimental parts.

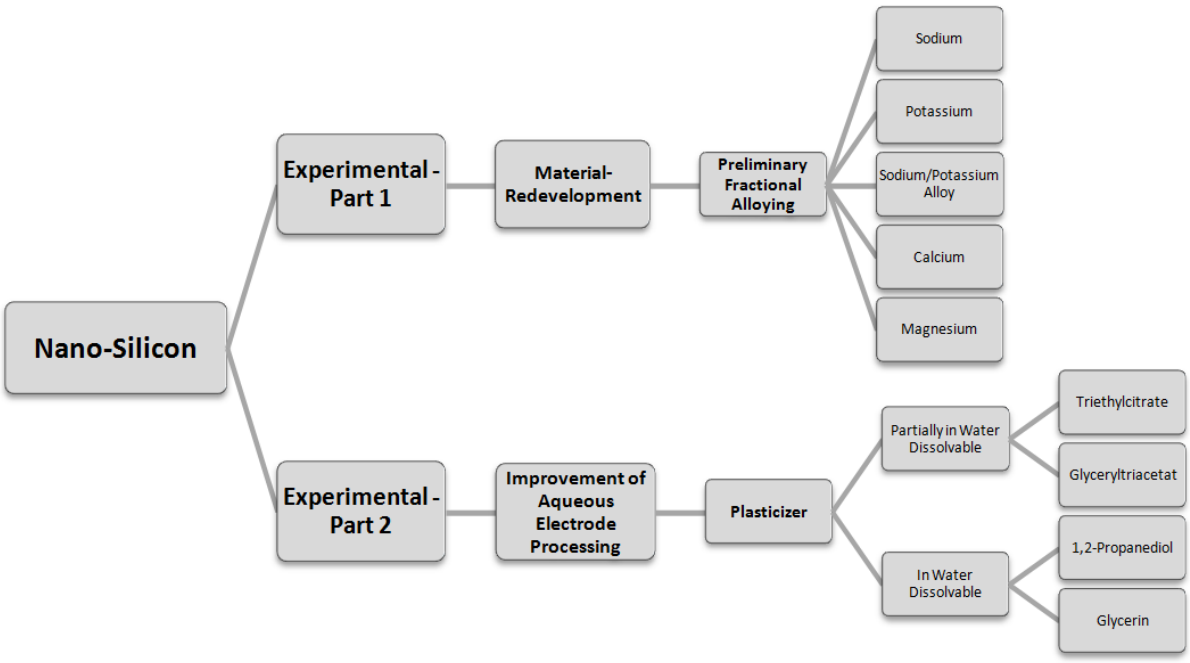

Figure 4: Content of the experimental part

The first experimental part (chapter 5, page 58) deals with the material redevelopment in the field of nano-scaled silicon. By preliminary fractional alloying of nano-scaled silicon powders with elements like sodium, potassium, a sodium/potassium alloy, calcium and magnesium an improvement of the electrochemical performance of silicon-electrodes were observed.

The second experimental part (chapter 6, page 92) deals with the improvement of aqueous electrode processing by using partial in water dissolvable and in water dissolvable plasticizers during the preparation of the electrode-paste. The used plasticizers are triethylcitrate, glyceryltriacetate, 1,2-propanediol and glycerin. They show neither pollutive nor deleterious properties and improve the aqueous electrode processing.

2 Electrochemical Energy Systems – the Past and Nowadays

In 1786 in Italy Luigi Galvani (1737 - 1798) made a prominent discovery. During the dissection of a frog he could observe a contraction of the muscular tissue of a frog´s leg when he touched it with two different metals. In 1794 Alessandro Conti di Volta (1745 - 1827) started to investigate this "animal electricity" and found out that the origin of the electricity arose from the use of two different metals which are connected through the acid medium of the animal tissue. This knowledge formed the basis of the construction of the first electrical battery – Volta´s electric battery. Volta´s electric battery consisted of alternately one superimposed on the other copper- and tin-plates or silver- and zinc-plates. These plates were separated by for example diluted sulfuric acid moistened plates of cardboard and connected in series. Volta´s electric battery was a primary cell (Figure 5)[6].

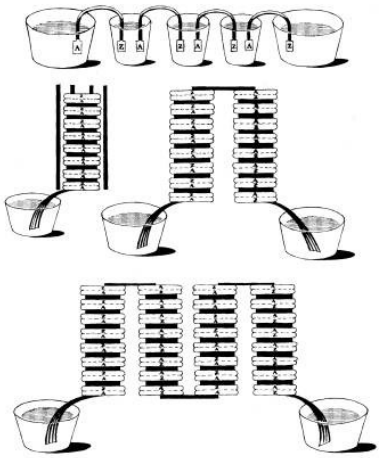

Figure 5: Four variations of Volta´s electric battery[7]

1801 Johann Wilhelm Ritter (1776 - 1810) developed the first secondary battery, the "Rittersche Säule" (Figure 6). The "Ritter´sche Säule" consisted of a vessel with sodium chloride solution and periodically one superimposed on the other silver-, zinc- and cardboard disks[6].

Figure 6: „Ritter´sche Säule"[8]

In 1936 John Daniell (1790 – 1845) invented the so called Daniell cell (chapter 3.1.3, page 10). The first design of the Daniell element consisted of a copper vessel filled with copper sulfate solution. In this vessel immersed a gullet of an ox, which contained a solution of sulfuric acid and a vertical zinc rod. The gullet of the ox acted as a separator. In further consequence the sulfuric acid were substituted with zinc sulfate (Figure 7)[9].

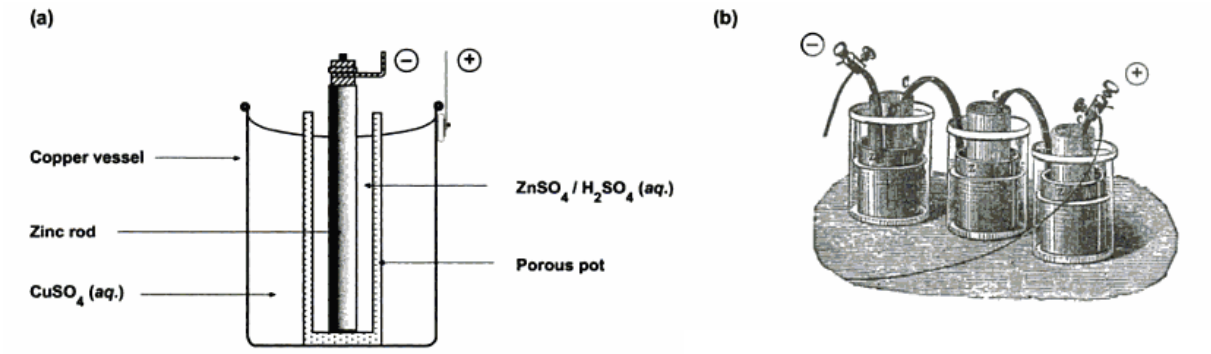

Figure 7: (a) Schematic setup of a Daniell cell; (b) early design of a Daniell cell[9]

In 1866 Georges Leclanché (1839 – 1882) presented a cell named after him – the Leclanché cell. This cell consisted of a glass receptacle filled with a solution of ammonium chloride. A zinc rod and a carbon rod were immersed in this solution. The zinc rod constituted the negative electrode and the carbon rod the positive one, which were housed in a porous ceramic pot and packed around with a mixture of manganese dioxide powder and carbon powder[9].

The French chemist Gaston Planté (1834 – 1889) presented in 1859 the first operative secondary cell (Figure 8). His secondary cell consisted of a cylindrical glass vessel filled with a dilute sulfuric acid, in which immersed two concentric spirals of lead sheet. A porous cloth acted as separator. This was the birth of the lead-acid battery, which importance increased over the next decades.

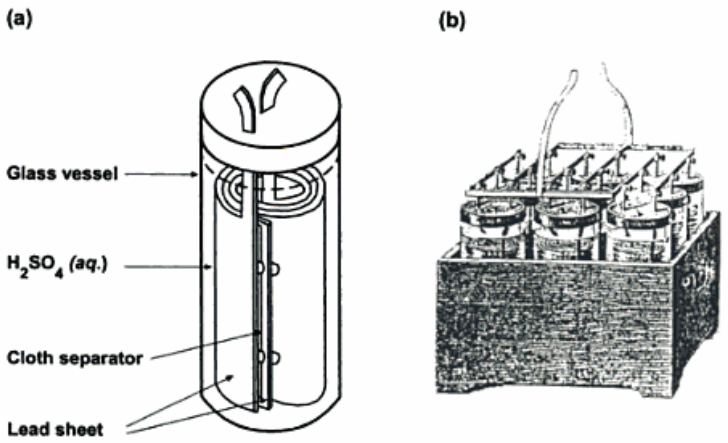

Figure 8: (a) Schematic setup of Planté´s lead-acid cell; (b) early design of a battery consisting of nine Planté cells[9]

In 1900 Thomas Alva Edison (1847 - 1931) and Waldemar Junger (1869 – 1924) developed the nickel-cadmium battery and the nickel-iron battery. Both systems consisted of a positive nickel hydroxide electrode and a concentrated solution of potassium hydroxide as electrolyte. What makes the difference was the negative electrode – within the nickel-cadmium battery a mixture of cadmium and iron constituted the anode and within the nickel-iron battery a all-iron anode. The proper sense of this invention was manifested in 1948, when a gas-proof casing was designed[9],[10],[11].

In 1912 the chemist Gilbert Newton Lewis (1875 – 1946) laid the foundation of an outstanding technology with his pioneer work on lithium batteries. Among the various other rechargeable cells, like for example the nickel-cadmium cells or the nickel-metal hydride cells, lithium-based batteries seem to be the systems of choice because they provide higher energy densities and higher operating voltages. In the early 1970s the first non-rechargeable lithium battery became commercially available. In the 1980s the research dealed with rechargeable lithium battery systems and since Sony launched the first lithium-ion battery in 1991 these secondary battery systems took over the market of portable electronic devices, such as cell-phones, computers and much more.

Figure 9: Rechargeable lithium-ion battery produced by Sony[12]

3 Fundamentals

3.1 Electrochemical Energy Systems

Electrochemical energy systems convert chemical energy into electrical energy. In these devices, the chemical reactions are reduction-oxidation (redox) reactions and the gained energy of these reactions is, at least, available as electric current. In the simplest case an electrochemical energy system consists of one galvanic element. In series or/and parallel connected galvanic elements are called battery. In general, batteries are classified into[13],[14],[15]:

- **Primary cells** in which the electrochemical reactions proceed irreversibly. A primary cell is a non rechargeable battery.
- **Secondary cells** in which the electrochemical reactions are reversible. A secondary cell is a rechargeable battery and mainly known as accumulator.

3.1.1 Functional Principle of a Battery

The term “battery” usually describes two or more in series- or parallel-connected electrochemical cells, but in common usage, also single cells are called batteries.
In general, an electrochemical cell (battery) consists of two electrodes, a positive electrode and a negative electrode, an electrolyte, a separator and a housing. The electrodes immerse in the electrolyte, which acts as a medium for the ion transfer between the two electrodes. The for ions but not for electrons permeable separator is placed between the two electrodes and should be wetted with the electrolyte. The main function of the separator is the prevention of an internal short circuit.
The particular electrodes contain the redox-active species, which store the chemical energy. When the battery is discharged, the negative electrode (anode) contains the component that is oxidized – the negative electrode releases electrons. In parallel, the positive electrode (cathode) contains the component that is reduced – the positive electrode accepts electrons. The electrons flow via an external circuit from the anode to the cathode and simultaneously for each electron one ion migrates through the electrolyte from the anode to the cathode. Thus, this ion flow determines the electric current that the battery delivers. Eq. 1 and Eq. 2 show the reactions of the anode (A) and the cathode (C) during the discharging process of a cell. Eq. 3 illustrates the consequent cell reaction[15],[16].

$$A_{red} \rightarrow A_{ox} + e^-$$

Eq. 1

$$C_{ox} + e^- \rightarrow C_{red}$$

Eq. 2

$$A_{red} + C_{ox} \rightarrow A_{ox} + C_{red}$$

Eq. 3

In the case of a secondary cell for the charging process the redox-reactions at the electrodes are reversed and the previously gained amount of energy has to be provided to the cell.

3.1.2 Standard Electrode Potential

As already mentioned, two interconnected electrodes are a galvanic element. Each of both half cells delivers a typical contribution to the cell voltage. Nevertheless, these contributions are not measurable individually[17].

Therefore, to define a standard electrode potential for every redox active species the reduction of H^+(aq) to H_2(g) at standard conditions (1 M solution, 25°C) is fixed as reference half cell reaction and it is assigned a potential of 0 V (Eq. 4). The electrode on which this reaction occurs is called normal hydrogen electrode (NHE)[18],[17].

$$Pt/H_2(g)/H^+\ (aq)$$

Eq. 4

Thus, if we connect a metal electrode with the normal hydrogen electrode we obtain the so called normal potential or standard electrode (or redox) potential E^0 of this electrode. If $E^0 < 0$ the metal is denoted as base metal and if $E^0 > 0$ the metal is denoted as noble metal[15]. The standard electrode potentials of each metal can be listed in tabular form – the so called electrochemical series of metals, which is shown in Figure 10.

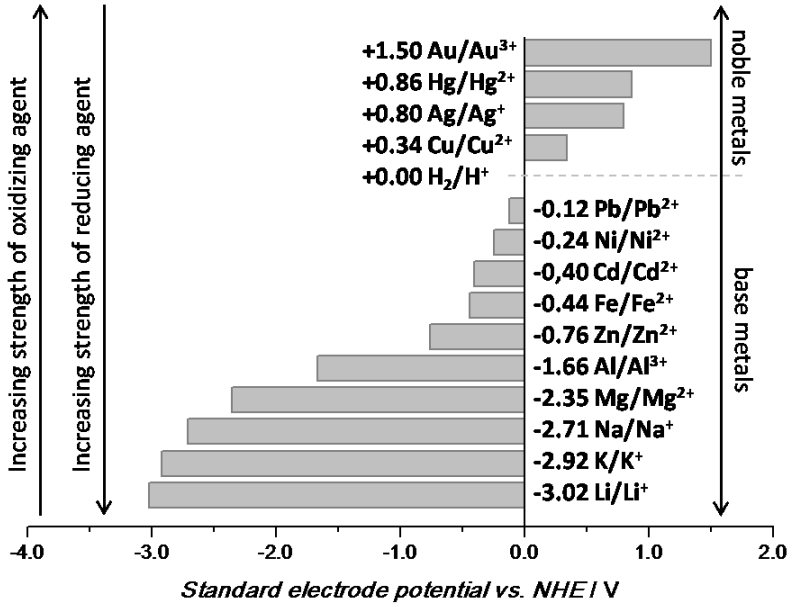

Figure 10: Electrochemical series of metals and their standard electrode potentials[19]

The standard cell voltage arises out of the difference of the standard redox potentials of the cathode- and the anode-reaction (Eq. 5)[18].

$$E_{Cell} = E^0_{Cathode} - E^0_{Anode}$$

E_{Cell} …standard cell voltage [V]
$E_{0,Cathode}$ …standard redox potential of the cathode [V]
$E_{0,Anode}$ …standard redox potential of the anode [V]

Eq. 5

3.1.3 The Daniell Element

The so called Daniell element is a simple example of an electrochemical cell. The Daniell element consists of two half cells. The negative electrode, a zinc anode, immerses in a 1 mol·l^{-1} solution of zinc sulfate [Zn/Zn^{2+}] and the positive electrode, a copper cathode, immerses in a 1 mol·l^{-1} solution of copper sulfate [Cu/Cu^{2+}] (Figure 11)[20]. A salt bridge officiates as an ion conducting connection between the two half cells to ensure charge equilibration. When the external circuit is closed, an oxidation of the metallic zinc and a formation of Zn-ions occur. In parallel, the excess electrons within the oxidizing zinc electrode migrate across the external circuit to the copper electrode and copper-ions are reduced and metallic copper is deposited[15].

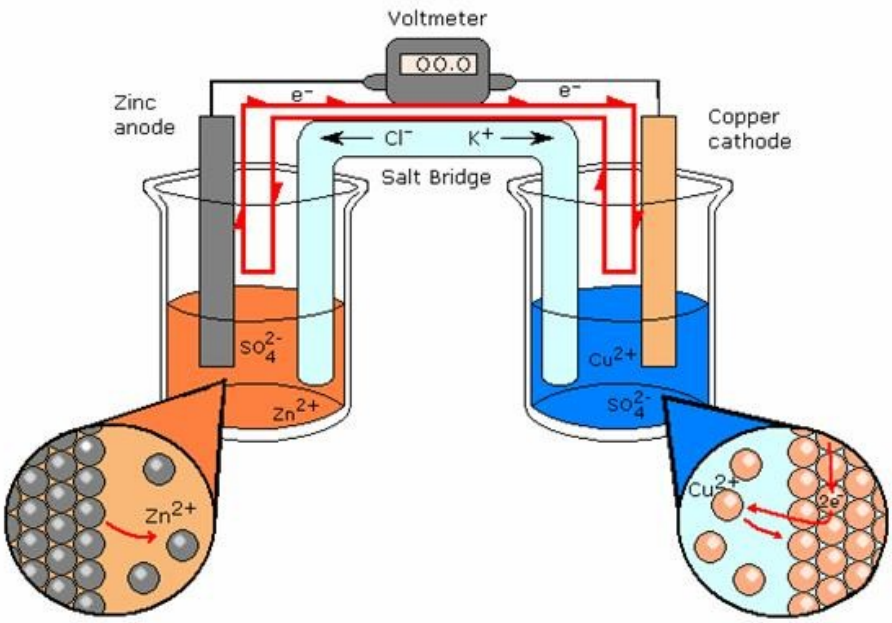

Figure 11: Schematic figure of a Daniell cell[21]

The implicated half cell reactions are shown in Eq. 6 and Eq. 7[18].

$$Anode: Zn(s) \rightarrow Zn^{2+}(aq) + 2e^- \quad E^0_{Zn/Zn^{2+}} = -0.76\,V$$

$E_{0,Zn/Zn2+}$ …standard redox potential of the half cell reaction Zn/Zn^{2+} (chapter 3.1.2, page 9)

Eq. 6

$$Cathode: Cu^{2+}(aq) + 2e^- \rightarrow Cu(s) \quad E^0_{Cu/Cu^{2+}} = +0.34\,V$$

$E_{0,Cu/Cu2+}$ …standard redox potential of the half cell reaction Cu/Cu^{2+} (chapter 3.1.2, page 9)

Eq. 7

As already described in the previous chapter (chapter 3.1.2, page 9) the difference between the cathode potential and the anode potential at standard conditions (1 M solutions, 25°C) provides standard voltage of a cell. Eq. 8 illustrates the standard cell voltage of the Daniell element[18]. This value accrues from the standard electrode potentials of copper and zinc (Eq. 6 and Eq. 7).

$$E_{Daniell\ element} = E^0_{Cu/Cu^{2+}} - E^0_{Zn/Zn^{2+}} = +0.34\,V - (-0.76\,V) = 1.10\,V$$

Eq. 8

3.1.4 Thermodynamic Fundamentals

3.1.4.1 Basic Considerations at Equilibrium State

If it is not possible to measure the standard potential, for example because there are no standard conditions (1 M solution, 25°C), the potentials can be investigated by thermodynamic calculations. This determination requires an electrochemical equilibrium within the electrolyte and at the phase boundary electrode/electrolyte, which actually means that no external current flow and no linked reactions occur. Figure 12 shows such equilibrium at the interphase electrode/electrolyte by taking the example of the Daniell cell[15],[17].

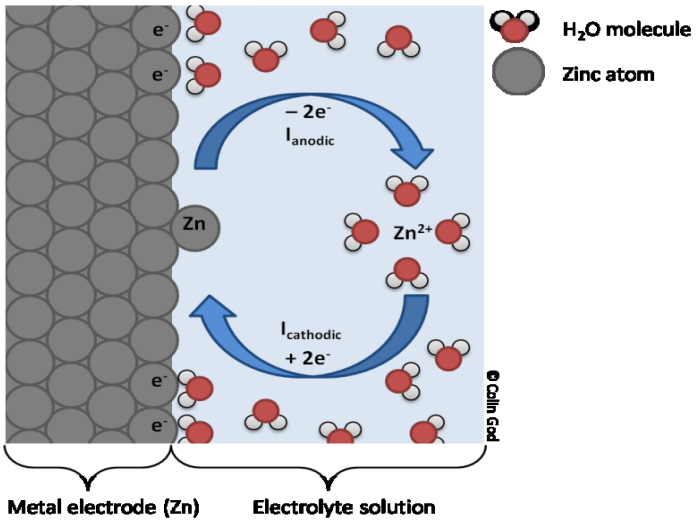

Figure 12: The electrode/electrolyte interphase at equilibrium state[19]

The three thermodynamic parameters of an electrochemical reaction in equilibrium state are[16]:

- **The enthalpy ΔH.** ΔH corresponds to the theoretical available amount of energy which is released or absorbed during the electrochemical reaction.
- **The free enthalpy ΔG.** ΔG corresponds to the amount of chemical energy which can be converted into electrical energy and conversely. Thus, ΔG represents the utilizable energy.
- **The entropy ΔS.** ΔS corresponds to the reversible energy loss or gain during the chemical/electrochemical process.

A fundamental relation between these three parameters constitutes the Gibbs-Helmholtz relation (Eq. 9). TΔS corresponds to the amount of heat released or consumed during the electrochemical reaction[15].

$$\Delta G = \Delta H - T\Delta S$$

ΔG …reaction enthalpy [J]
ΔH …reaction enthalpy [J]
T …temperature [K]
ΔS …reaction entropy [J]

Eq. 9

So as to connect the dots between the equilibrium cell voltage and the free reaction enthalpy, a few fundamental considerations have to be made. The equilibrium cell voltage depends on four parameters – the concentration, the temperature, the pressure and the pH-value[15].

The chemical potential of a substance J in a composition is defined as shown in Eq. 10.

$$\mu_J = \left(\frac{\partial G}{\partial n_J}\right)_{p,T,n'}$$

μ_J …chemical potential of a substance J
ΔG …reaction enthalpy [J]
Δn_J …amount of a substance J
p …pressure [Pa]
T …temperature [K]
n´ …constant amount of substance in the composition except substance J

Eq. 10

Thus, the chemical potential illustrates the change of the reaction enthalpy at constant pressure, temperature and amount of substance, whereby the amount of substance J is varied. Eq. 10 can be restated to Eq. 11.

$$dG = V \cdot dp - S \cdot dT + \sum_J \mu_J \cdot dn_J$$

V ...volume [m^3]

Eq. 11

At constant pressure and constant temperature Eq. 12 arise from Eq. 11.

$$dG = \sum_J \mu_J \cdot dn_J = dw_{e,max}$$

$w_{e,max}$ …electrical work (electrical energy) [$kg \cdot m^2 \cdot s^{-2}$], [J]

Eq. 12

Deduced from Eq. 12 it can be determined that a system, if is not at equilibrium state, can generate not only volumetric work, but also electrical work through the change of composition.

If we assume a one formula conversion with no changes of composition the free reaction enthalpy can be defined (Eq. 13).

$$1mol\ A \rightarrow 1mol\ B$$

$$\Delta_R G = \left(\frac{\partial G}{\partial \xi}\right)_{p,T} = \mu_B - \mu_A = \sum_J \nu_J \cdot \mu_J$$

$\Delta_R G$ …free reaction enthalpy [J]
ξ …reaction duration
ν …stoichiometry factor

Eq. 13

Thus, the relationship between the equilibrium cell voltage and the free reaction enthalpy can be formulated (Eq. 14).

$$-\nu \cdot F \cdot E = \Delta_R G$$

ν …number of exchanged electrons
F …Faraday constant (96485 $C \cdot mol^{-1}$)
E …equilibrium cell voltage [V]
$\Delta_R G$ …free reaction enthalpy [J]

Eq. 14

A voluntary reaction always runs in the direction of a state of minimally free reaction enthalpy. This direction corresponds to a positive value of the cell voltage (exergonic reaction). If the cell reaction is at equilibrium, the cell potential is zero (Figure 13) [17].

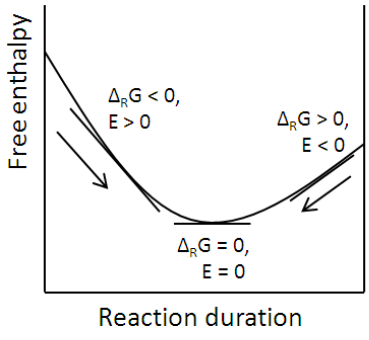

1. $\Delta_R G = 0$ and $E = 0$ → cell is located in equilibrium
2. $\Delta_R G < 0$ and $E > 0$ → exergonic or voluntary reaction (e.g. galvanic cell)
3. $\Delta_R G > 0$ and $E < 0$ → endergonic or forced reaction (e.g. electrolysis)

Figure 13: The free reaction enthalpy vs. the reaction duration [17]

The correlation between the free reaction enthalpy and the composition of the reaction mixture is shown in Eq. 15.

$$\Delta_R G = \Delta_R G^0 + RT \cdot ln \prod_J a_J^{\nu_J}$$

a_J …activity of a substance

Eq. 15

Dividing both sides of by „-ν·F" leads to Eq. 16.

$$-\frac{\Delta_R G}{\nu \cdot F} = -\frac{\Delta_R G^0}{\nu \cdot F} - \frac{R \cdot T}{\nu \cdot F} \cdot ln \prod_J a_J^{\nu_J}$$

Eq. 16

Recalling Eq. 14 we can formulate Eq. 17 – the Nernst equation.

$$E = E^0 - \frac{R \cdot T}{\nu \cdot F} \cdot lnQ \qquad with\ Q = \prod_J a_J^{\nu_J}$$

Eq. 17

The concentration of the compounds which react at the electrode influences the chemical potential of one half-cell (Eq. 18)[(15)].

$$\mu = \mu_0 + RT \cdot lnc_i$$

c_i …concentration of the compounds
R …universal gas constant (8,314 J·mol^{-1}·K^{-1})

Eq. 18

Thus, we can modify the Nernst equation (Eq. 17) regarding the concentrations or the activities of the relevant species (Eq. 19).

$$E = E^0 + \frac{R \cdot T}{\nu \cdot F} \cdot ln\left(\frac{c_{Ox}}{c_{Red}}\right) \quad or \quad E = E^0 + \frac{R \cdot T}{\nu \cdot F} \cdot ln\left(\frac{a_{Ox}}{a_{Red}}\right)$$

Eq. 19

3.1.4.2 The Electric Double Layer

The phase boundary electrode/electrolyte plays an important role to consider electrochemical processes. At this phase boundary the gradients of the chemical and electrical potentials are the greatest and it´s the place, where the charge transfer occurs.

If a metal electrode immerses into an aqueous solution containing positive and negative charge carrier, through the electrochemical potential of the metal electrode, a charge balancing movement of the cations and anions proceeds within the electrolyte. Thus, a double layer arises at the phase boundary electrode/electrolyte. The Helmholtz layer model, or also called the Helmholtz double layer, is a simple principle to illustrate the proceedings at the phase boundary electrode (metal)/electrolyte (Figure 14)[22].

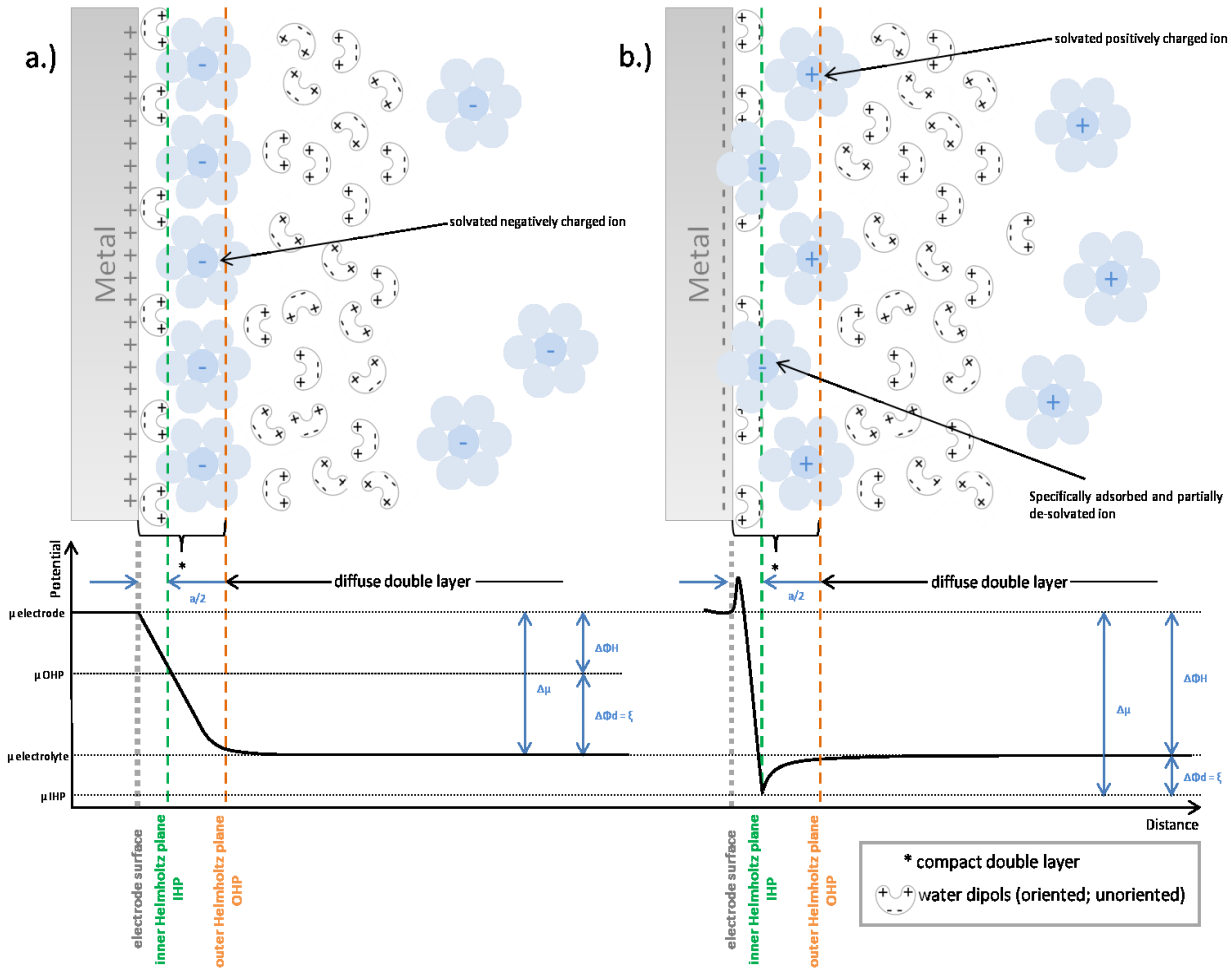

Figure 14: Schematic representation of the Helmholtz double layer for a.) a positively and b.) a negatively charged electrode[23],[24]

The model proceeds from the assumption, that the solvated ions and electrical dipoles approach the electrode-surface as close as possible. From this it follows that the Helmholtz double layer consists of two parallel layers of opposite charge – one constitutes the metal surface and the other constitutes the solvated contrary charged ions. The closest approach of the solvated ions is defined as the half diameter of the ions (a/2)[(23)].

An extension of the Helmholtz layer model constitutes the Goüy-Chapman model, which include the thermal motion of the ions. This leads to the definition of a diffuse double layer, which consists of anions and cations in a spatially extended region near the electrode surface (from the outer Helmholtz plane to the bulk of the solution).

A further extension is the so called Stern model. It is a combination of the Helmholtz layer model and the Goüy-Chapman model and is the most realistic description of the double layer. Stern appears that the Helmholtz plane will vary with the ion-type attracted to the electrode-surface. Hence, the distance between the ions and the electrode is determined by the type of ions – some ions may are able to lose their solvated sheaths and approach very closely to the electrode-surface, others are not able to remove their solvated sheaths and the distance between them and the electrode surface is greater. Out of this consideration Stern defines an inner Helmholtz plane (IHP) and an outer Helmholtz plane (OHP)[(23)].

Summarizing, the electric double layer consists of[(25)]:

- **An inner Helmholtz plane (IHP).**
  Within the IHP the potential changes linearly with the distance. These considerations involve the adsorbed water molecules and in the case of a negatively charged metal electrode the specifically adsorbed and partially de-solvated anions.
- **An outer Helmholtz plane (OHP).**
  Within the outer Helmholtz plane the potential varies linearly with the distance and it comprises the solvated ions.
- **An outer diffuse layer (Goüy-Chapman layer).**
  In the diffuse layer the potential varies exponentially with the distance and it contains the distributed ions.

3.1.4.3 Basic Considerations at Current Flow

At the preassigned discussions we assume from an electrochemical equilibrium state within the electrolyte and at the phase boundary electrode/electrolyte, but if an electrical current flows through the cell, for example while discharging a battery, a deviation in the measured potential (terminal voltage) and the equilibrium potential (open circuit voltage) of the single half cell is observable. This difference is called overpotential η (Eq. 20)[(15),(26),(23)]. The measured open circuit voltage (OCV) slightly differs from the equilibrium voltage due to the reason that at any time diffusion gradients and side reactions (self discharge) occur within the cell.

$$\eta = E - E_r$$

η …overpotential [V]
E_r …equilibrium potential [V]
E …measured potential [V]

Eq. 20

In principle, we distinguish between four different types of overpotentials:

- **The charge transfer overpotential.**
  The charge transfer overpotential is caused by the reduced speed of the charge transfer through the phase boundary electrode/electrolyte. The nature of the reacting substances, the kind of electrode material and the conditions within the electrolyte influence the charge transfer overpotential [(15),(23),(27)].
- **The diffusion overpotential.**
  The diffusion overpotential describes the impoverishment of reacting substances at high current densities at the phase boundary electrode/electrolyte. This zone is called the Nernst layer and the reaction kinetics is determined only by diffusion through this zone[(15),(23),(27)]
- **The reaction overpotential.**
  The reaction overpotential arise when the speed-limiting factor is the overall electrode reaction, like adsorption and desorption, or other phenomena, which occur on the electrode surface[(15),(23),(27)].
- **The crystallization overpotential.**
  The crystallization overpotential arises when metal-ions accomplish an inhibited intercalation into the lattice[(15),(27)].

Figure 15 illustrates the difference in the measured terminal voltage and the open circuit voltage of a cell, whereby the ohmic resistance, the charge transfer overpotential and the diffusion potential are considered.

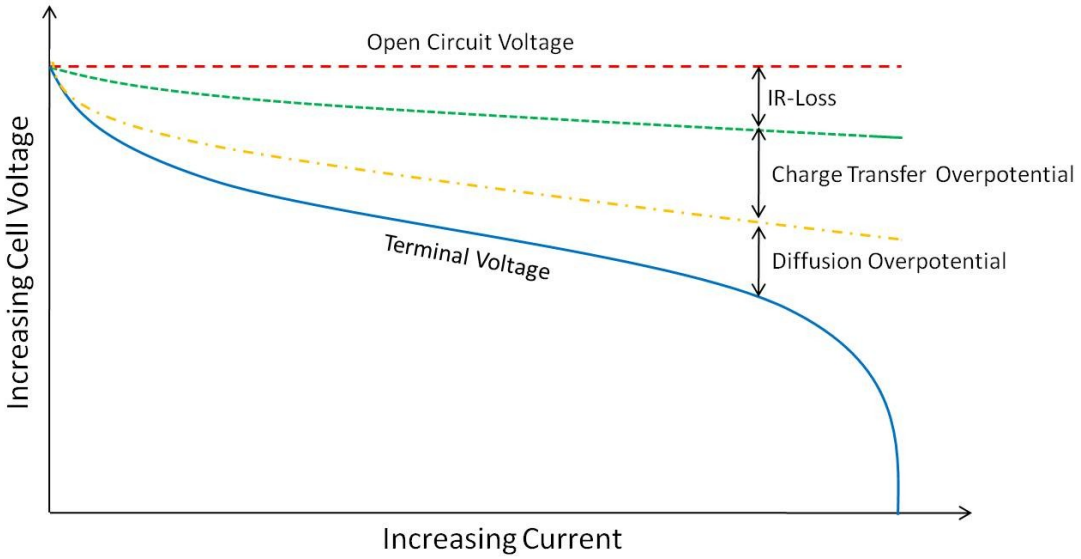

Figure 15: Schematic illustration of the internal voltage drop of a cell[28]

3.1.5 Important Parameters

The **energy** content of a battery arises out of the integration of the capacity for the voltage (Eq. 21).

$$E_{el} = U \cdot I \cdot t$$

E_{el} …electric energy [kg·m^2·s^{-2}], [J]
U …voltage [kg·m^2·A^{-1}·s^{-3}], [V]
I …electric current [A]
t …time [s]

Eq. 21

The **specific energy** [Wh·kg^{-1}] respectively the **energy density** [Wh·l^{-1}] maintain the stored energy content of a battery. This parameter depends on the specific charge/discharge density of the active materials as well as on the redox-potentials of the electrochemical reactions.

The **power** of a battery system can be calculated as described in Eq. 22[15].

$$P = \frac{E_{el}}{t} = U \cdot I$$

P …power [kg·m^2·s^{-3}], [W]
E_{el} …electric energy [J]
t …time [s]

Eq. 22

The power related to the battery weight or volume is denoted as **specific power** ($W \cdot kg^{-1}$) or **power density** ($W \cdot l^{-1}$). This parameter describes the maximum current carrying capacity.

The **capacity** describes the withdrawable charge of a battery system (Eq. 23)[29].

$$Q = I \cdot t$$

Q …electric charge [C]
I …electric current [A]
t …time [s]

Eq. 23

The capacity is dependent on the discharge conditions, like the discharge current, and the temperature. At current flow the capacity and the cell voltage are related to the cell resistance – the higher the cell resistance, the greater the voltage decrease at current flow (Figure 16).

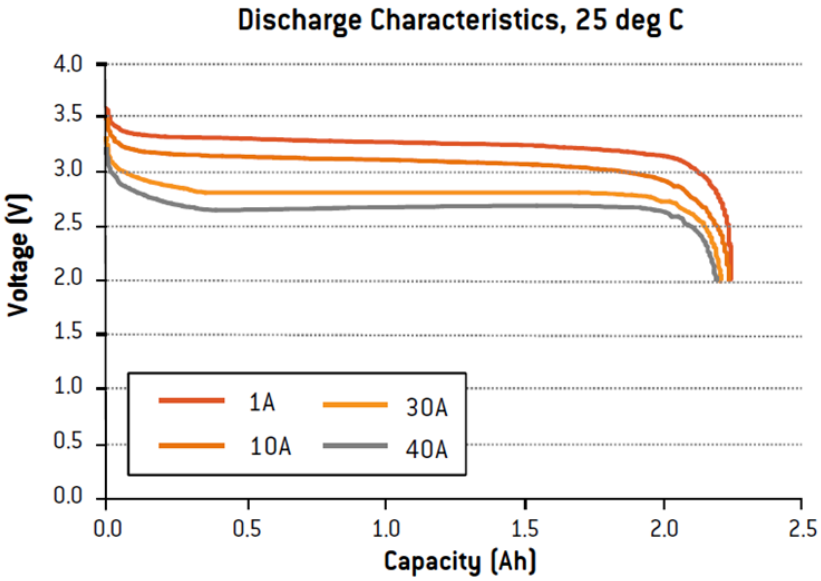

Figure 16: Discharge characteristics of a commercialized lithium-ion battery[30]

The storage capacity or capability of an active material arises from the number of electrons received or delivered per mass or per volume. This parameters are referred as **specific charge** ($Ah \cdot kg^{-1}$) or **charge density** ($Ah \cdot l^{-1}$).

The **C-rate** is the rate of electric current related to the cell capacity. For example 1 C is the equivalent current that charges or discharges a cell in 1 hour.

3.2 Theoretical Background on Lithium-Ion Batteries

3.2.1 Basic Concept of Rechargeable Lithium-Ion Batteries

Rechargeable lithium-ion batteries involve a reversible insertion/extraction of lithium-ions into/from the anode/cathode during the charge/discharge process. Hence, the two electrodes act as host matrices for the lithium-ions and are also called lithium insertion compounds.

The lithium-ions migrate across the electrolyte and the insertion/extraction of them into/from the host matrix is associated with a reduction/oxidation reaction of the compound assisted with a flow of electrons through an external circuit[31].

Two possibilities consist to configure rechargeable lithium-ion batteries. The first system is called the lithium-metal battery. The lithium-metal battery is comprised of a lithium-ion accepting insertion cathode material and a lithium-metal anode (Figure 17)[32]. Although metallic lithium is the anode material of choice due to its very negative standard electrode potential of -3,02 V vs. NHE (Figure 10) and its low equivalent weight, it is not possible to field metallic lithium as negative electrode material. During the cycling of metallic lithium extensive shape changes, side reactions with the electrolyte and consequential a corrosion of the lithium occur[1],[33].

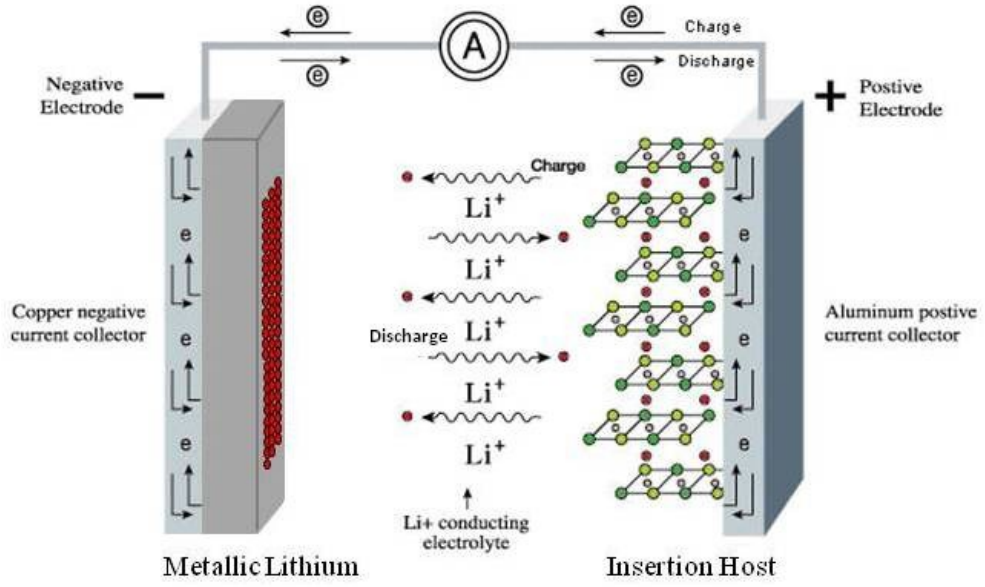

Figure 17: Schematic principle of a lithium-metal battery during charge and discharge

The second system, commonly known as lithium-ion battery, consists of two insertion materials which act as electrodes (Figure 18)[32]. One insertion electrode material releases lithium-ions, which are inserted into the other electrode insertion material (Eq. 24).

$$Cathode\ Reaction: \quad LiMeO_2 \leftrightarrow Li_{1-x}MeO_2 + xLi^+ + xe^-$$

$$Anode\ Reaction: \quad nA + xLi^+ + xe^- \leftrightarrow Li_xA_n$$

$$Cell\ Reaction: \quad LiMeO_2 + nA \leftrightarrow Li_xA_n + Li_{1-x}MeO_2$$

Me …for example Co, Ni or composites out of them
A …for example carbon

Eq. 24

The insertion/deinsertion of the Li^+-cations into/out of the host materials could cause an enormous expansion of the host materials. That results in mechanicals stress and finally the destruction of the material. Thus, the cycleability of a lithium-ion battery mainly depends on the dimensional stability of the insertion host materials during the charge and discharge process[33].

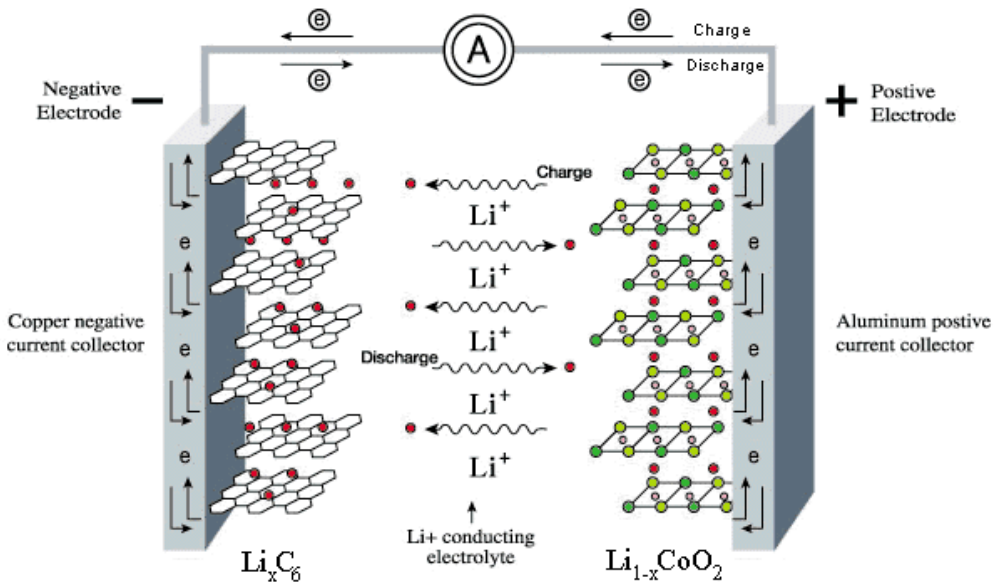

Figure 18: Schematic principle of a lithium-ion battery during charge and discharge[34]

3.2.1.1 Mass Transport in Lithium-Ion Batteries

In lithium-ion batteries the Li^+-cations do not represent the redox-active species - the lithium-ions are only responsible for the charge equilibration by transfer through the electrolyte. Figure 19 shows the three different transport types, which occur in a lithium-ion battery[35],[36]:

- The ion transport through the electrolyte.
- The ion transfer through the phase boundary electrolyte/electrode.
- The chemical diffusion within the active material particle.

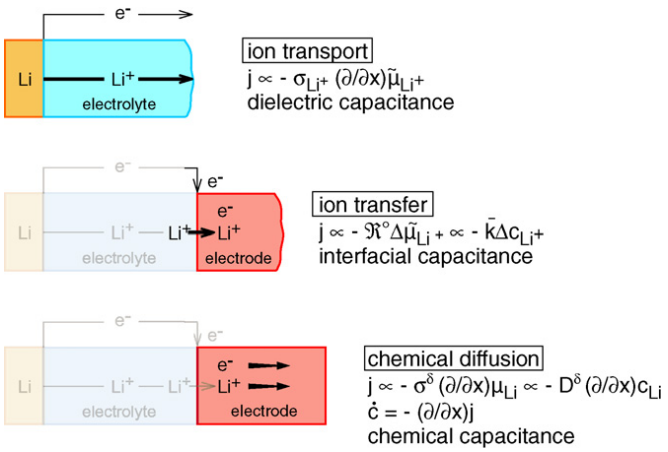

Figure 19: Schematic figure of the three different Li^+-ion transport types[35],[36]

The first step is the migration of charged Li^+-ions through the electrolyte. Transient processes within the electrolyte occur typically on the nanosecond scale and are usually dielectric phenomena (electrostatic storage). Hence, in order the ion transport within the electrolyte is a steady state process driven by the gradients in the electrochemical potential of the ion ($\tilde{\mu}$). The transport-coefficient arises out of the Li^+-ion conductivity within the electrolyte. At the electrode/electrolyte phase boundary the driving force for the Li^+-ion transition is the difference in $\tilde{\mu}_{Li+}$ at both sides. If we refer to the proximity to equilibrium state, the transport-coefficient arises out of the exchange rate of the transition process. The respective storage or insertion process depends on the interfacial capacitance and occur in a few micro-seconds. The time dependence has to be included, if the insertion of lithium-ions into the electrode is connected with the diffusion of Li^+ and e^-. The driving force is the gradient of the chemical potential of lithium $[(\delta/\delta x)\mu_{Li} = \delta/\delta x(\mu_{Li+}+\mu_{e-})]$ and the ambipolar conductivity σ^δ $[\sigma^\delta = \sigma^{-1}_{e-}+\sigma^{-1}_{Li+}]$. The chemical potential of lithium as well as the ambipolar conductivity is influenced by Li^+ and e^-. If the driving force is expressed in terms of lithium concentration gradients $[(\delta/\delta x)c_{Li}]$, then the concentration gradient becomes the chemical diffusion coefficient D^δ, which includes the ambipolar conductivity as well as the chemical capacity C^δ [i.e. $\delta_{cLi}/\delta_{\mu Li}$][37].

3.2.2 Anode Host Materials for Lithium-Ion Batteries

Metallic lithium shows many attractive properties as anode material in lithium-ion batteries. The two main advantages are the high theoretical specific capacity of 3862 $mAh \cdot g^{-1}$ and the high reachable cell voltage of >3 V, if it is used in cells which contain a non-aqueous electrolyte[38]. Unfortunately, lithium metal deposits as dentritic and highly reactive metal particles. Because this fact comes along with enormous security problems, like for example locally short circuits, lithium metal is substituted as negative electrode by carbonaceous materials, intermetallic anode materials and transition metal oxides.

3.2.2.1 Carbonaceous Materials

Nowadays, carbonaceous materials are the materials of choice as negative electrode material in commercial lithium-ion batteries due to their high specific charges and negative redox potentials. Furthermore, they deliver an excellent cycling performance caused by their dimensional stability. The insertion of lithium-ions into carbon is called intercalation (Eq. 24). We distinguish between three different types of carbons, which are capable of reversible lithium intercalation and used as anodes in lithium-ion batteries (Figure 20)[39],[40]:

- Graphite
- Hard carbon (non-graphitizing carbon)
- Soft carbon

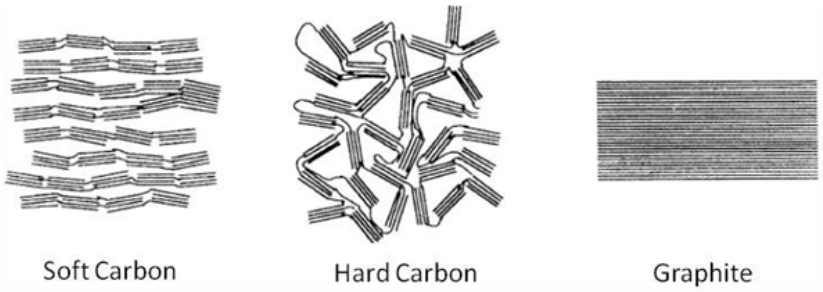

Figure 20: Schematic profile of the three different types of carbon[39]

In practice, especially graphite and hard carbon are used as materials for negative electrodes.

3.2.2.1.1 Graphite

At room temperature graphite is the most stable allotrope of carbon. The term “graphite” is only applicable to carbons having a layered lattice structure with a perfect stacking order of graphene layers. The two known modifications of graphite differ only by their stacking order (Figure 21)[33]:

- AB (hexagonal graphite; prevalent)
- ABC (rhombohedral graphite; rarer)

The layers are held together by van der Waals forces and each layer contains a conjugated sp^2 bond.

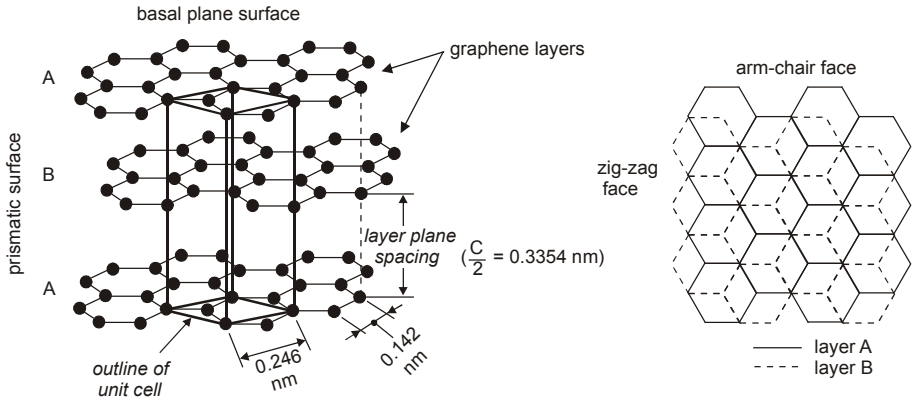

Figure 21: Hexagonal structure of graphite with the stacking order AB[33]

The lithiation of graphite is an intercalation process in which lithium-ions are inserted between the graphene layers. In general graphite accepts at room temperature that much lithium to form the LiC_6 phase, which delivers at delithiation a theoretical specific capacity of 372 $mAh \cdot g^{-1}$. The intercalation process of lithium into graphite occurs only at the arm-chair and zig-zag faces. An intercalation through the basal planes is only possible at defect sides. The intercalation of lithium into graphite leads to an increase of the layer distance from 0.335 nm through to 0.370 nm and the stacking order of the graphene layers shift from AB to AA (Figure 22)[33],[39].

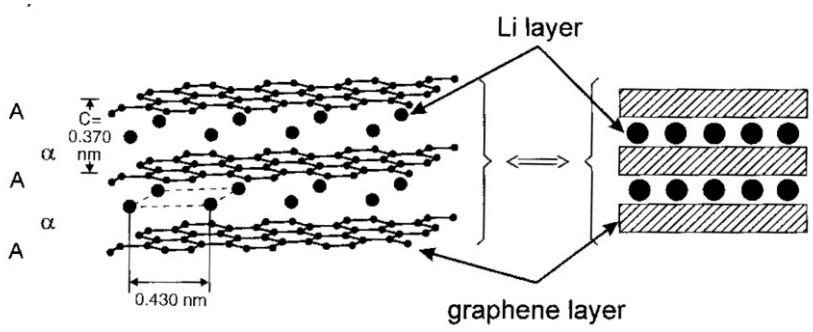

Figure 22: Schematic profile of the AA stacking layer sequence[33]

The intercalation of lithium into graphite proceeds stepwise and comes along with several stage formations (Figure 23). Every stage can be assigned to a current peak in a cyclovoltammogramm. The reversible intercalation of lithium-ions into graphite occurs in four steps provable by means of for example X-ray diffraction[41]. The investigated stoichiometries of $LixC_6$ are x = 0.20, 0.34, 0.50 and 1.0. This corresponds to the intercalation compounds LiC_{30}, LiC_{18}, LiC_{12} and LiC_6[33].

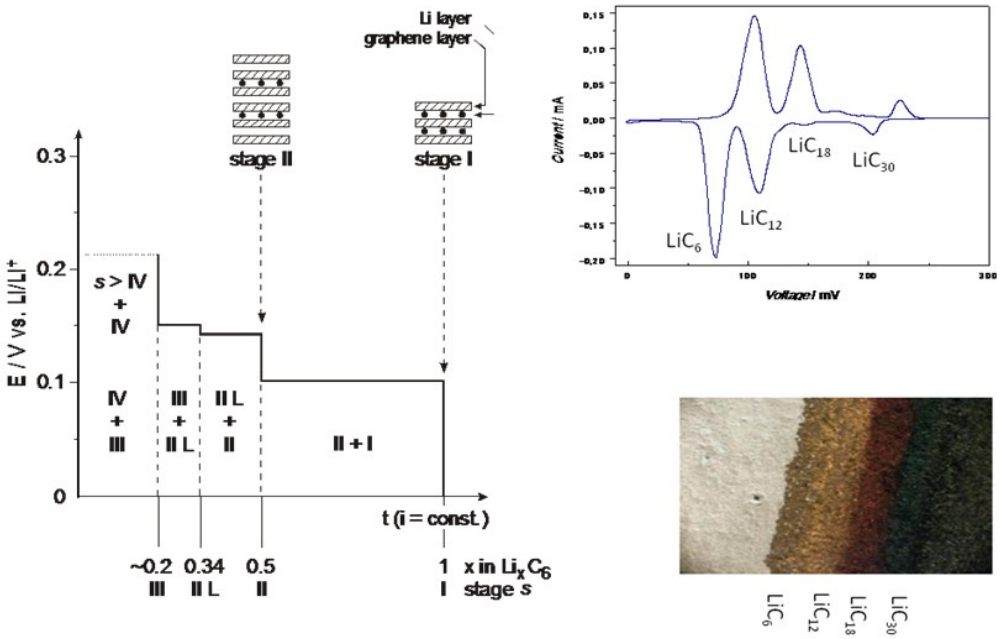

Figure 23: Stage formation during electrochemical intercalation of lithium-ions into graphite[33],[34],[42]

As already described above the delithiation process should deliver a theoretical specific capacity of 372 $mAh \cdot g^{-1}$. In practice the consumed charge during the first intercalation process even exceeds the theoretical specific capacity, but the deintercalation process only regains about 80-95 % of this charge. This charge loss C_{irr} is shown in Figure 24 and can be ascribed to the formation of the so called solid electrolyte interphase (chapter 3.2.6, page 44) and corrosion-like reactions of Li_xC_6. The subsequent cycles show a better charge consumption to charge recovery ratio[33].

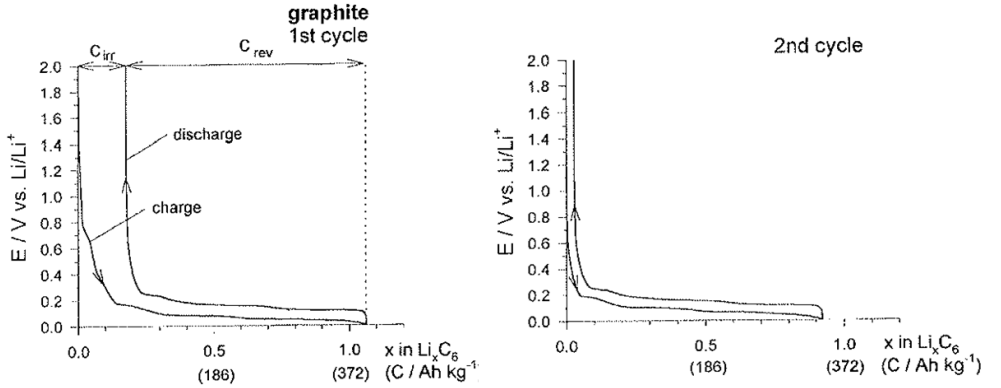

Figure 24: Constant current cycling curves (1st and 2nd cycle) of the graphite Timrex KS 44; electrolyte: $LiN(SO_2CF_3)_2$/ethylene carbonate/dimethyl carbonate[33]

A serious problem of highly graphitic matrices is the so called solvent co-intercalation. Using organic donor solvent electrolytes the intercalation of lithium-ions and other alkali-metal-ions into fairly crystalline graphitic carbons comes along with the formation of solvated, ternary graphite intercalation compounds $Li(solv)_yC_n$. The so called solvated intercalation is associated with an enormous expansion of the graphite host matrix up to 150 %. This leads to an exfoliation of the graphite and a decrease of the charge storage capability[33]. Host materials of high crystallinity are more damageable to solvated intercalation.

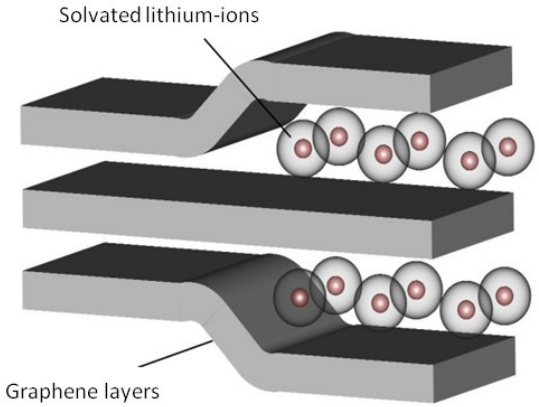

Figure 25: Schematic drawing of solvated intercalation into graphite[34]

The solid electrolyte interphase (chapter 3.2.6, page 44) enormously figures into the prevention of the solvated intercalation. She acts as a kind of sieve, which restrains the solvate shell of the solvated ions.

3.2.2.1.2 Hard Carbon and Soft Carbon

Hard carbon and soft carbon are so called non-graphitic carbons. They consist of carbon atoms that are mainly arranged in a planar hexagonal network but without far-reaching crystallographic order. These materials are characterized by amorphous areas embedding and crosslinking crystalline areas (Figure 26)[33].

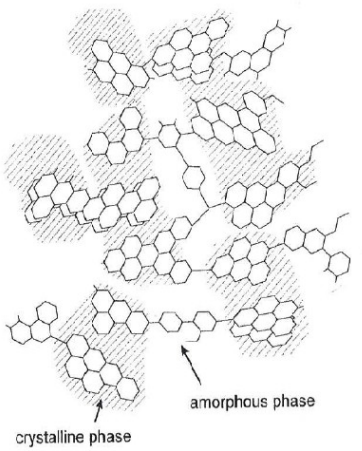

Figure 26: Schematic drawing of non-graphitic carbons[33]

Hard carbon doesn´t graphitize even under high temperature conditions. In contrast, soft carbon is easily changeable with heat treatment over 2000°C[43]. Figure 27 illustrates the dependence of the specific capacity on the heat treatment of non-graphitic carbons. Conspicuously are the differences in the specific capacities of the various carbon types at different temperatures. These differences can be explained by the different structures and chemistries of carbons, which are prepared by heating of organic precursors[44].

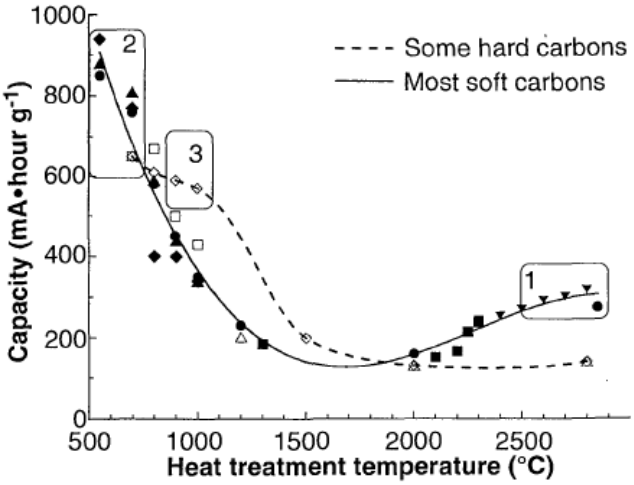

Figure 27: Reversible capacity of hard carbons and soft carbons vs. heat treatment temperature (2nd charge/discharge cycle)[44]

Hard carbon delivers higher specific capacities than graphite. The reason behind that is, that in hard carbons compared to graphite the lithium-ions can be adsorbed on each side of single layer and, hence, a stoichiometry of Li_2C_6 is feasible (Figure 28)[45].

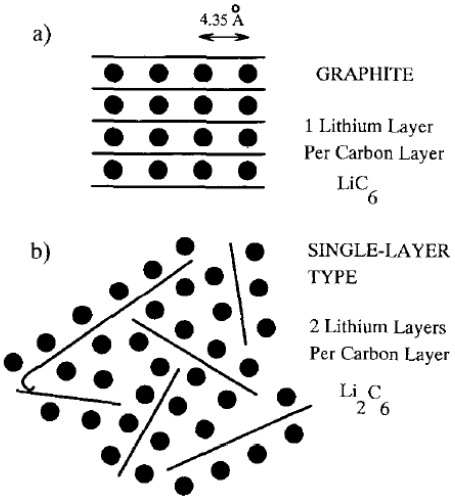

Figure 28: Intercalation of lithium into a.) graphite and b.) single layer hard carbon[45]

3.2.2.2 Intermetallic Anode Materials

In the early 1960s scientists started to investigate chemical elements, which form alloys with lithium, as anode materials in lithium-ion batteries. A. N. Dey published in 1971 that a number of metals can be alloyed with lithium at room temperature, like for example Sn, Pb, Al, Au, Pt, Zn, Cd, Ag and Mg[46]. In 1976 R. A. Sharma and R. N. Seefurth reported the formation of lithium-silicon alloys at elevated temperatures (400-500°C)[47].

The metallic host materials are used in the delithiated state. In analogy to carbonaceous materials the formation of the intermetallic Li_xM phase and the formation of the solid electrolyte interphase take place during the first charge (Eq. 25)[48].

$$M + Li^+ + e^- \rightleftharpoons Li_xM$$

M …metallic host material

Li_xM …intermetallic phase

Eq. 25

Lithium alloys are able to provide nearly the same or even slightly higher packing densities than lithium metal (Table 1). These high packing densities of lithium-alloys results in high specific and volumetric capacities. The $Li_{22}Si_5$ phase, for example, provides a theoretical specific capacity of 4199 $mAh \cdot g^{-1}$[36].

Table 1: Packing densities of different lithium-alloys compared to lithium-metal[34],[49]

Metal or Alloy (Li_xM)	Packing Density of Lithium [mol·l^{-1}]
Li	76.36
$Li_{22}Si_5$	88.56
$Li_{22}Sn_5$	75.74
$Li_{22}Pb_5$	72.17

Unfortunately, lithium alloy-based electrodes exhibit dramatic volume expansion (100 - 300 %) and contraction during lithium insertion and extraction (Figure 29)[15]. In this connection, attention should be paid not only to the inserted lithium-ions (Li_x^+), but also to the corresponding negative charge (M^{x-}), which is formed through the charge transfer and is significant lager than the neutral species (M^0)[34]. In the case of silicon the insertion of lithium-ions into the metal comes along with the formation of zintl phases. These zintl phases are due to their high ionic character very brittle. Thus, the volume expansion of the host material quickly leads to a decomposition of dimensional stability of the material itself. Within an electrode these processes cause a disintegration of the active material particles and, hence, a loss of contact to the ionic and electric conducting environment [34]. All these processes lead to a poor cycling performance of an electrode. Hence, electrodes made out of intermetallic anode materials don´t prove themselves in practice.

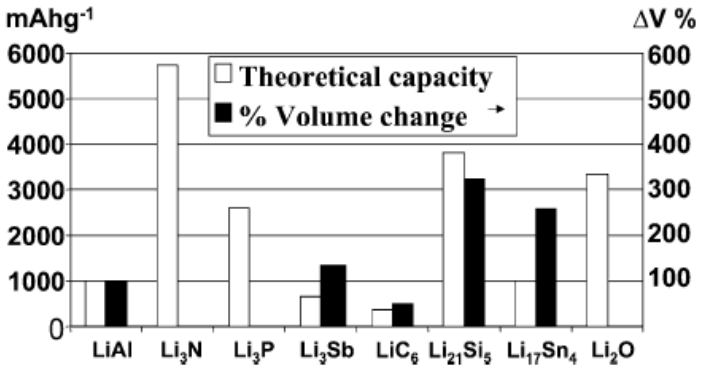

Figure 29: Theoretical capacities and volume expansion of different anode materials[40]

To overcome this above mentioned problem of volume expansion several efforts have were made:

- Small particle sizes of the active material (nano-scale) lead to less absolute volume changes and, hence, they are less sensitive to volume changes[48].
- Embedding of the host material into a stable matrix buffers the volume expansion/contraction. A typical representative of these electrode types are so called silicon/carbon composite materials[50].

3.2.2.3 Transition Metal Oxides

Various transition metal oxides have been studied as negative electrode materials for lithium-ion batteries due to their good stability and safety concerns. Main disadvantages of transition metal oxides are their low specific capacities and their poor cycling performance. Based on the reaction mechanism during the first discharge transition metal oxides can be classified into two groups[51]:

- Transition metal oxides with insertion reaction
- Transition metal oxides with conversion reaction

3.2.2.3.1 Transition metal oxides with insertion reaction.

The insertion reaction of lithium into the lattice of the electrode material occurs without basic structural change of the host material. A typical insertion reaction is shown in Eq. 26[51].

$$MO_x + yLi^+ + ye^- \leftrightarrow Li_xMO_x$$

M …a transition metal

Eq. 26

Some known representatives of this group are $Li_4Ti_5O_{12}$, TiO_2, MoO_x, WO_2 and Fe_2O_3. Ti-based oxide materials as anodes in lithium-ion batteries show a few advantages, like an excellent stability, low costs and they are also environmentally benign. Especially the spinel type $Li_4Ti_5O_{12}$ is a promising candidate as anode material, despite the high working potential and the relatively low specific capacity of 175 $mAh \cdot g^{-1}$. The advantages of $Li_4Ti_5O_{12}$ are the good cycle performance due to its stable crystal structure, the improved safety without lithium plating on the surface of the electrode for examples at temperatures below 0°C and the high rate capability without electrolyte decomposition during cycling[51].

Compared to $Li_4Ti_5O_{12}$, TiO_2 shows a higher specific capacity of 335 $mAh \cdot g^{-1}$ (for $LiTiO_2$). Another interesting representative of this group is MoO_2. MoO_2 shows a distorted rutile structure, a theoretical specific capacity of 209 $mAh \cdot g^{-1}$ (for $LiMoO_2$) and a working potential comparable to $Li_4Ti_5O_{12}$[51].

3.2.2.3.2 Transition metal oxides with conversion reaction.

In this case a conversion reaction and a complete decomposition of LiO_2 and inactive transition metal occurs. A typical insertion reaction is shown in Eq. 27[51].

$$M_xO_y + 2yLi^+ + 2ye^- \leftrightarrow xM + yLi_2O$$

M …a transition metal

Eq. 27

This group includes transition metal oxides of the type MO_x (M = Fe, Co, Ni, Cu,…). As shown in Eq. 27 at the first insertion of lithium these oxides were converted to a metallic state with the formation of Li_2O. During the subsequent extraction of lithium they reversibly return to their initial state. Advantages of these materials are the high reversible lithium storage capacities of 400 - 1000 $mAh \cdot g^{-1}$ and the good cycling performance with average working potentials of 1.8 - 2.0 V (vs. Li/Li^+).

3.2.3 Cathode Materials for Lithium-Ion Batteries

Within the scope of cathodes we can differ between several insertion compounds. Basically cathode materials can be classified into three groups:

- Transition metal oxides and chalcogenides
- Organic Molecules
- Polymers

Whereby, transition metal oxides and chalcogenides constitute the most attractive compound classes for positive host materials. In general, these compounds can be classified into one-, two- and three-dimensional host materials. According to their structural build-up the lithiation and delithiation process occurs in different dimensions[33].

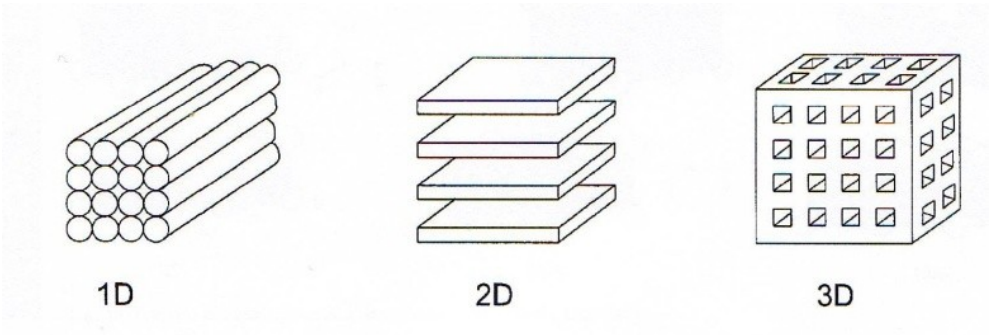

Figure 30: Schematic build-up of one-, two- and three-dimensional transition metals and chalcogenides[33]

3.2.3.1 Layered Transition Metal Oxide Electrodes

The best known representative of this group is $LiCoO_2$. It is formed at high temperatures of about 800 - 900°C and has a layered structure like α-$NaFeO_2$ (Figure 31). The structure is based on a close-packed network of oxygen atoms with Li^+ and Co^{3+} ions arranged on alternating (111) planes of the cubic rock-salt structure[33],[52]. $LiCoO_2$ is a so called two-dimensional host material – the lithiation and delithiation process occurs from two sides. During the first charge process $LiCoO_2$ fulfils the function of the lithium source within the lithium-ion battery. Half a mole of lithium is extracted from or inserted between the CoO_2 planes. Thus, the electrode stoichiometry in the discharged and charged state varies between $LiCoO_2$ and $Li_{0.5}CoO_2$. Usually $LiCoO_2$ based lithium batteries operate between 4.2 V and 3.0 V. An enlargement of the potential of 4.2 V vs. Li/Li^+ enables the extraction of more than 0.5 Li per Co atom. Thus, an increase of the specific capacity would be the result.

But increasing the potential and, hence, extract more than 0.5 mole of lithium, negatively affects the cycling performance of the $LiCoO_2$, because of the structural change from a monocline to a hexagonal buildup[53],[54]. If 4.2 V vs. Li/Li^+ are not exceeded specific capacities of around 140 $mAh \cdot g^{-1}$ can be reached reversibly[33].

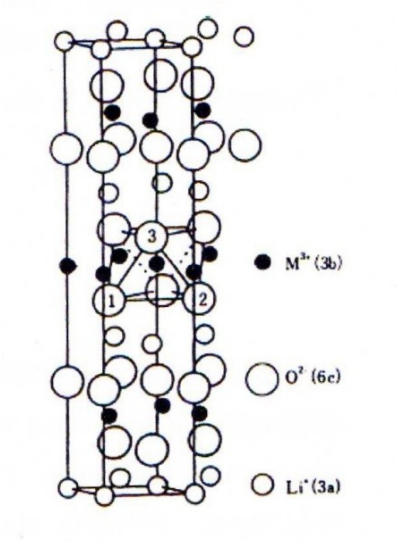

Figure 31: α-$NaFeO_2$-structure (M = Co, Ni or Mn)[39]

Lithiumcobaltoxide is the current used cathode material, but due to the fact that the world reserves of the transition metal cobalt are limited it is very expensive and, furthermore, cobalt is harmful for human, animal and plant (R 42/43-53)[55]. These are the reasons why there are several efforts to substitute parts of the cobalt by nickel or manganese without changing the α-$NaFeO_2$ structure. This replacement leads to a stoichiometry of $LiNi_xMn_yCo_{1-x-y}O_2$ ($0 \leq x \leq 0.5$)[56],[57].

3.2.3.2 Spinel Oxide Compounds

The best known cathode material of this type is $LiMn_2O_4$. $LiMn_2O_4$ has a cubic spinel structure as shown in Figure 32. The Mn_2O_4 framework provides a three-dimensional interstitial space for the lithium-ion insertion and extraction (3D lithium-diffusion).

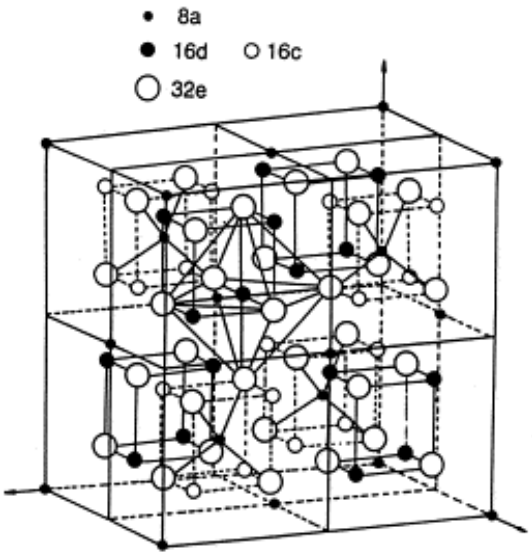

Figure 32: Cubic lattice structure of $LiMn_2O_4$ [39]

λ-MnO_2 constitutes the delithiated phase of $LiMn_2O_4$. There can be removed either one lithium from $LiMn_2O_4$ at 4.1 V vs. Li/Li^+ (Figure 33, region I & region II) or inserted at 3 V vs. Li/Li^+ leading to $Li_2Mn_2O_4$ (Eq. 28; Figure 33, region III). The insertion of lithium at 3 V vs. Li/Li^+ is accompanied with a phase transition from the cubic spinel structure to an ordered, tetragonal structure (NaCl-type) and is irreversible[39],[58],[59].

$$LiMn_2O_4 + Li \rightarrow Li_2Mn_2O_4$$

Eq. 28

$LiMn_2O_4$ provides a working voltage of 4 V vs. Li/Li^+ and a theoretical specific capacity of around 148 $mAh \cdot g^{-1}$, whereby the practical specific capacity is about 120 to 130 $mAh \cdot g^{-1}$ [58],[59],[60]. It offers compared to $LiCoO_2$ several advantages, like the low price and non-toxic materials.

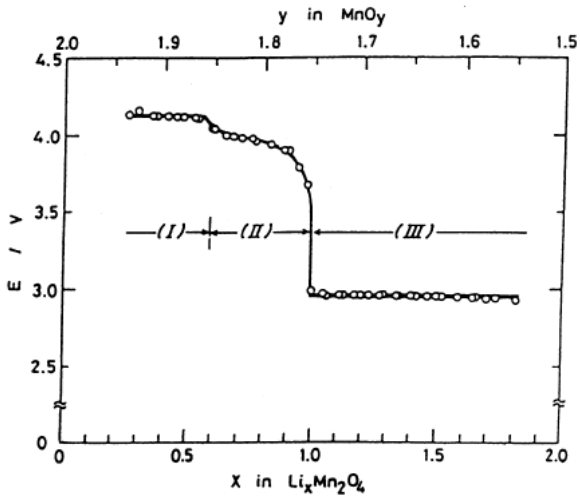

Figure 33: Open circuit voltage curve of the $Li_xMn_2O_4$ (0 < x < 2) compound[39]

However, during cycling the capacity of the $LiMn_2O_4$ spinel fades slightly. Three possible reasons for that appearance are[52],[61],[62]:

- A disproportionation reaction of the Mn^{3+}-ions and the subsequent dissolution of Mn^{2+}-ions in the electrolyte solution (Eq. 29).

$$2Mn^{3+}_{Solid} \rightarrow Mn^{4+}_{Solid} + Mn^{2+}_{Solid}$$

Eq. 29

- The Jahn-Teller effect: The manganese-ions within $LiMn_2O_4$ existing in two different oxidation states, viz. of 50 % Mn^{3+} and 50 % Mn^{4+} (Eq. 28). In the range of around 3 V vs. Li/Li^+, when the amount of Mn^{3+} increases, the Jahn-Teller distortion can occur (Figure 33). The initiation of the Jahn-Teller effect is the phase transition from the cubic to the tetragonal structure. This structural change can lead to a large volume change and subsequent to a damage of the $LiMn_2O_4$ cathode.
- The high oxidation ability of Mn^{4+} leads to a decomposition of the electrolyte solvents.

To overcome at least part of these problems several investigations had been made, like for example doping $LiMn_2O_4$ with hetero-atoms, like Li, B, Mg, Al (cations) and F, I, S (anions). The addition of for example manganese or an excess of lithium should lead to an enhanced average oxidation state and a prohibition of the Jahn-Teller distortion[52].

3.2.3.3 Olivine Structured Phosphate based Materials

In the last few years olivine structured phosphate based materials Li_xMPO_4 (M = Mn, Fe, Co, Ni) enter the spotlight of interest as cathode materials for lithium-ion batteries. They rank among the one-dimensional host materials – the lithium motion occurs through one-dimensional channels[63]. Table 2 illustrates a few properties of these compounds.

Table 2: Different properties of Li_xMPO_4 (M = Mn, Fe, Co, Ni)[63],[64]

Compound	Voltage vs. Li/Li^+	Theoretical Specific Capacity [$mAh \cdot g^{-1}$]	Lithium-Diffusivity [$cm^2 \cdot s^{-1}$]
$LiMnPO_4$	4,1	171	10^{-7}
$LiFePO_4$	3.4-3.5	171	10^{-8}
$LiCoPO_4$	4.8	167	10^{-9}
$LiNiPO_4$	5.1	167	10^{-5}

$LiFePO_4$, for example, is insensitive to overcharge, because of the highly stable three-dimensional framework, which arise out of the covalent, strong P-O bonds within the $(PO_4)^{3-}$-polyanion[65]. This fact leads to an improvement of the battery safety. Beyond that, $LiFePO_4$ shows several advantages like a low toxicity, low costs of the raw materials, a high thermal stability and a high capacity.

A disadvantage of olivine structured phosphate based cathode materials is the very low electric conductivity and, furthermore, due to the one-dimensional lithium diffusion through the channels, which can be blocked by defects and impurities, the slow kinetics [63].

3.2.4 Binding Agent

The function of a binding agent (or binder) is to glue the particles of the active material together and to ensure a contact of them with the current collector foils aluminum (at the cathode) and copper (at the anode). A binder should especially exhibit, beside of the binding purpose, the following properties[66]:

- Chemical and electrochemical stability
- Insolubility in the electrolyte

As desirable an ideal binding agent exhibits these properties.

Over the last years especial two binder systems were intensively investigated – on the one hand the organic polyvinylidene fluoride (PVdF) based binder system and on the other hand the aqueous styrene-butadiene copolymer (SBR) based binder system with sodium salt of carboxymethylcellulose (Na-CMC) as viscosity regulating agent, whereby for now the former are the most frequently applied binder systems for the negative electrode[67],[68]. However, SBR based binder systems show a lot of advantages as binder for the negative electrode, especial for intermetallic anode materials, like a higher binding ability with small amount and more flexible electrodes, but it is a not suitable binding system for the positive electrode, because of its poor oxidation-resistance during the charging process of the cell[66]. In 2005 W.-R. Liu et al. illustrated that the aqueous SBR/Na-CMC based binder system applied to Si-C composite anodes shows in contrast to the organic PVdF binder system an improved cycling stability (Figure 34)[67]. At first this beneficial effect in combination especial with silicon anodes and silicon/graphite composite electrodes was attributed to the more flexible SBR binder, which should compensate the high volume changes of the material (3.2.2.2, page 29). However, in 2007 J. Li et al. reported that Na-CMC based binder systems shows improved properties in contrast to the combination of SBR and Na-CMC[69].

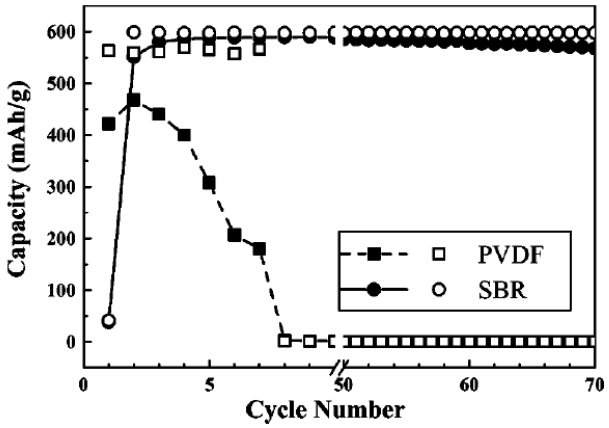

Figure 34: Cycling performances of a Si/C composite anode with on the one hand polyvinylidene fluoride (PVdF) as binder and on the other hand with styrene-butadiene copolymer (SBR)/sodium carboxymethylcellulose (Na-CMC) as binder system[67]

Hence, during the last years the sodium carboxymethylcellulose more and more comes into the limelight as binder system, especially for silicon anodes and silicon/graphite composite electrodes [70],[71]. The Na-CMC can be processed by aqueous electrode-paste preparation and the recovery of the active electrode material at the end of the battery life can be easily made by pyrolysis of the natural binder. In addition to it the price of Na-CMC is much lower than that of PVdF[72].

3.2.5 Electrolytes for Lithium-Ion Batteries

The electrolyte acts as the medium for the lithium-ion transfer between the two electrodes. Generally electrolytes for lithium-ion batteries can be classified into:

- Liquid electrolytes
- Solid polymer electrolytes
- Gel-type electrolytes

The requirements, which should be fulfilled by an electrolyte for lithium-ion batteries, are:

- A wide electrochemical stability window
- A good ionic conductor and electronic insulator
- An inert behavior against other cell components, like for example the separator or the casing
- A robustness against various abuse conditions, like electrical abuse and thermal abuse

3.2.5.1 Liquid Electrolytes

Currently, liquid electrolytes are the common electrolyte systems in the application field of lithium-ion batteries. In the easiest case liquid electrolytes consist of a non-aqueous, aprotic solvent and a therein dissolved inorganic lithium-salt, but in fact, a liquid electrolyte consists of a mixture of non-aqueous, aprotic solvents, one or more therein dissolved inorganic salts and usually a various number of electrolyte additives. Non-aqueous electrolytes exhibit several advantages:

- A wide liquid range
- A wide electrochemical stability window
- A good compatibility with the electrode materials

The disadvantages of non-aqueous electrolytes are:

- A low (ion-) conductivity
- High costs
- A high flammability
- A high environmental gravity

Possible, commonly used solvents are shown in Figure 35. Furthermore different characteristics of possible solvents are listed in Table 3.

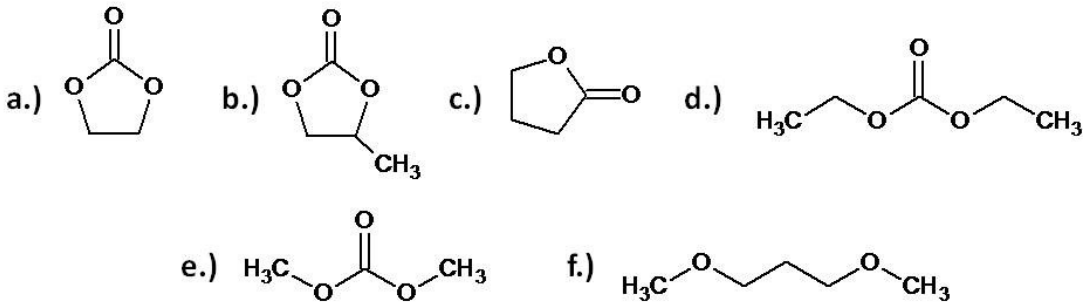

Figure 35: Molecular structure of possible electrolyte solvents within a lithium-ion battery: a.) Ethylenecarbonate (EC), b.) Propylenecarbonate, c.) γ-Butyrolactone, d.) Diethylcarbonate (DEC), e.) Dimethylcarbonate (DMC), f.) Dimethoxyethane (DME)

Table 3: Physical properties at 25°C of different solvents. T_m…freezing point, T_b…boiling point, ε…dielectric constant, η/cP…viscosity at constant pressure, ρ…density[15],[39]

Solvent	Acronym	T_m [°C]	T_b [°C]	ε	η/cP	ρ [kg·l^{-1}]
acetonitril	AN	-48.835	81.60	35,95	0.341	0.77675
n-butylamine	n-BU	-49.1	77.4	4.88 (20°C)	0.681	0.7385
γ-butyrolactone	**GBL**	**-43.53**	**204**	**39.1**	**1.7315**	**1.1242**
diethyl carbonate	**DEC**	**-43.0**	**126.8**	**2.8059**	**0.7529**	**0.96928**
dimethoxy ethane	**DME**	**-58**	**84.50**	**7.075**	**0.407**	**0.86122**
dimethyl carbonate	**DMC**	**4.6**	**90**	**3.1075**	**0.55902**	**1.06316**
dimethyl sulfoxide	DMSO	18.54	189	46.5	1.992	1.0955
1,3-dioxolane	DIOX	-97.22	76.5		0.6 (20°C)	1.0647 (20°C)
ethylene carbonate	**EC**	**36.5**	**238**	**90.36 (40°C)**	**1.9 (40°C)**	**1.3214 (40°C)**
ethylmethyl carbonate	**EMC**			**2.4**	**0.65**	**1.0070**
methansulfonyl chloride	MSC	-50	160			
methyl acetate	MA	-98.05	56.868	6.68	0.364	0.9279
methyl formate	MF	-99.0	31.75	8.5 (20°C)	0.328	0.9664
3-methyl-2-oxazolidinone	3Me2OX	15.9	74-75 (<1 Torr)	77.5	2.450	1.1702
2-methyltetrahydrofuran	2MeTHF	-137.25	79.9	6.75		0.8540 (20°C)
propylene carbonate	**PC**	**-54.53**	**242**	**64.95**	**2.512**	**1.1996**
sulfolane	TMS, SL	28.45	287.3	43.30 (30°C)	10.287 (30°C)	1.2619 (30°C)
sulfur dioxid		-75.46	-10.01	15.6 (0°C)	0.4285 (0°C)	1.46 (0°C)
sulfuryl chloride		-54.1	69.4	11.5	0.674	1.657
tetrahydrofuran	THF	-108.5	65.965	7.43	0.459	0.8819
thionyl chloride		-104.5	77	8.675	0.603	1.629

A during the last decade intensively investigated group of possible solvents for the electrolyte within a lithium-ion battery are room-temperature molten salts, so called room-temperature ionic liquids (RTIL).

Advantages of these “green” compounds are the high thermal stability and the good electrochemical stability[73]. A RTIL is at room-temperature a liquid compound, which only consists of ions and their combinations. Typical examples for RTILs are several quaternary ammonium salts, but these compounds cannot be used directly in lithium-ion batteries [74]. The reason for that is the occurrence of solvated intercalation into the graphite anode, because no suitable solid electrolyte interphase (chapter 3.2.6, page 44) is formed at the surface of the common anode material graphite. However, by using the ionic liquid N-methyl-N-propyl pyrrolidinium bis(fluorosulfonyl)imide ($PYR_{13}FSI$) as solvent a suitable solid electrolyte interphase, which suppresses solvated co-intercalation and, hence, allows the reversible lithium insertion/deinsertion in graphite anodes, is formed. Major drawbacks of $PYR_{13}FSI$ are the high costs and the low electrochemical stability window[75].

3.2.5.1.1 Conductive Lithium Salts

The composition of an electrolyte strongly influences the cycle life, the cell performance and the aging properties of a cell. There are a number of factors, which influences the electrolyte performance. One of the most popular ones is the electrolyte conductivity.

The conductivity of an organic electrolyte is only about 1/100 – 1/1000 of the conductivity of an aqueous electrolyte. Therefore, the addition of a suitable salt to the electrolyte is indispensable.

The main requirements, which an ideal lithium salt for the liquid electrolyte of a lithium-ion battery should meet, are[15],[76]:

- A good solubility in the particular solvents
- An intrinsic thermal stability
- A high conductivity of its solutions
- A high chemical stability with the solvent
- A high electrochemical stability
- The anion should be inert toward other cell components
- A low molecular weight
- Low costs

In Table 4 the properties of different common lithium salts for electrolytes in lithium-ion batteries are listed.

Table 4: Properties of different conductive salts for lithium-ion batteries[77] (LiTf…lithium triflat; LiTFSI…lithium trifluorosulfonimide)

Properties	Good → Bad					
Ion mobility	$LiBF_4$	$LiClO_4$	$LiPF_6$	$LiAsF_6$	LiTf	LiTFSI
Ion pair dissociation	LiTFSI*	$LiAsF_6$	$LiPF_6$	$LiClO_4$	$LiBF_4$	LiTf
Solubility	LiTFSI	$LiPF_6$	$LiAsF_6$	$LiBF_4$	LiTf	
Thermal stability	LiTFSI	LiTf	$LiAsF_6$	$LiBF_4$	$LiPF_6$	
Chemical inertia	LiTf**	LiTFSI	$LiAsF_6$	$LiBF_4$	$LiPF_6$	
SEI-formation	$LiPF_6$	$LiAsF_6$	LiTFSI	$LiBF_4$		
Al-corrosion	$LiAsF_6$	$LiPF_6$	$LiBF_4$	$LiClO_4$	LiTf	LiTFSI

To dissolve one of these conductive salts into an aprotic solvent, the solvent must show a high dielectric constant. Unfortunately, a high dielectric constant and a low viscosity are two qualities of solvents, which mostly exclude themselves mutually. This fact offers the problem, that a high viscosity of the solvent induces low lithium-cation mobility within the electrolyte. Due to this fact, solvents with a high dielectric constant, like EC or PC, are mixed with low-viscosity solvents, like DEC or DMC. Figure 36 illustrates the differences in electrolyte conductivity at different temperatures by the use of different conductive salts[78].

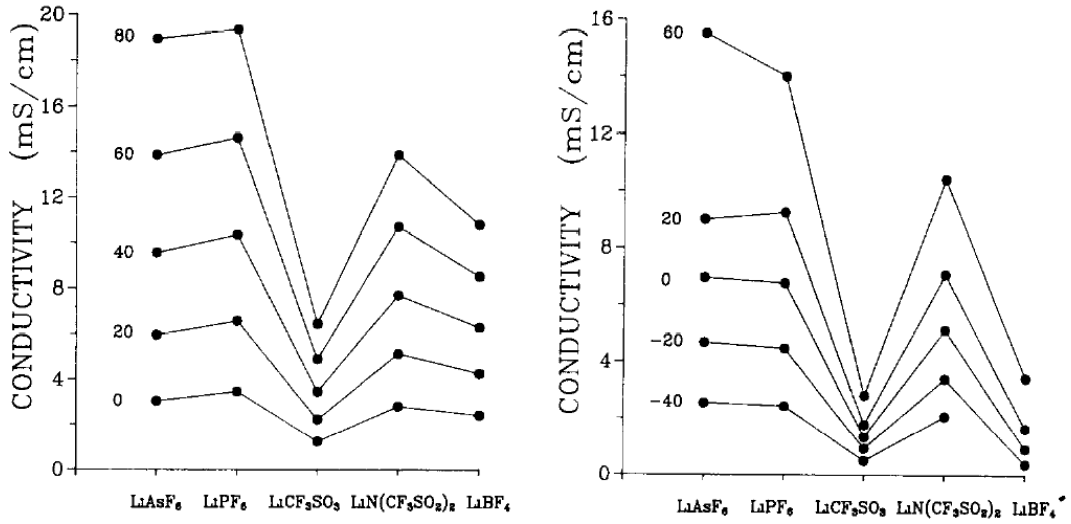

Figure 36: Conductivity of the electrolyte EC/PC (50/50) (left graph) with the addition of 1 M conductive salt (right graph). The temperatures [°C] are indicated on the graph[78]

Attention should be paid, that the addition of conductive lithium salt to the electrolyte only makes sense up to a certain concentration of the conductive lithium salt. The conductivity of the solution passes a maximum with the increase of the conductive salt concentration. Figure 37 illustrates the dependence of the conductivity to the conductive salt concentration[79].

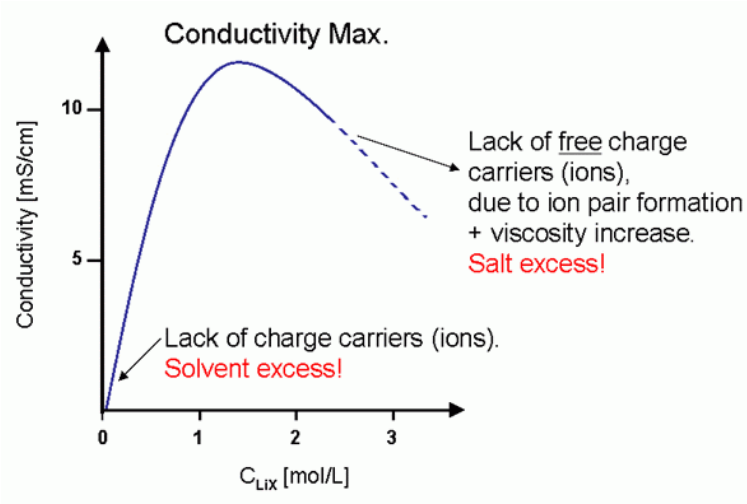

Figure 37: Dependence of the conductive salt concentration on the conductivity[80]

3.2.5.1.2 Electrolyte Additives

Added to an electrolyte system an additive should specifically influence the properties of the electrolyte. In the majority of cases commercial electrolytes contain a mixture of additives. The maximum amount of an additive in an electrolyte is 5 w% or 5 v%. Electrolyte additives can be classified into:

- Electrolyte additives for the anode passivation (SEI)
- Electrolyte additive for the overcharge protection
- Electrolyte additive for the improvement of the ability of wetting (electrolyte/separator; electrolyte/electrode)
- Electrolyte additive to minimize the flammability of the electrolyte
- Electrolyte additive to absorb undesirable components
- Electrolyte additive for the improvement of the electrolyte conductivity

In 2002, for example, D. Aurbach et al. reported that the presence of vinylene carbonate (VC) in an EC/DMC/$LiPF_6$ electrolyte system reduces the irreversible capacity of lithiated graphite electrodes and improves their cycling performance especially at elevated temperatures[81]. Nowadays VC is one of the most common electrolyte additives for lithium-ion batteries.

3.2.5.2 Solid Polymer Electrolytes, Gel-type Polymer Electrolytes and Ionic Liquids

Solid polymer electrolytes show several advantages, which minimize the security risks of a lithium-ion cell, like their inflammability and consequently their high temperature resistance and the absence of leakage problems. The main disadvantage of solid electrolytes is the minor ionic conductivity[82].

A gel-type polymer electrolyte consists of an organic electrolyte, which is integrated into a polymer matrix. Gel-type polymer electrolytes are a good opportunity to combine mechanical stability of a solid electrolyte with the chemical properties of a liquid electrolyte. An example of such a polymer is polyvinylidene fluoride (PVdF)[83],[84].

3.2.6 Electrode/Electrolyte Interphase – the Solid Electrolyte Interphase

Lithium cells and lithium-ion cells operate far beyond the thermodynamically stability limits of today known electrolytes. Consequently, at the negative electrode occurs a reductive decomposition of the electrolyte during the first cycle (charge). The result of this reductive electrolyte decomposition is the formation of a protective film on the surface of the negative electrode, which is called the solid electrolyte interphase (SEI). This not soluble film protects the electrode-surface from further corrosion and allows the transfer of lithium-ions, but prevents the electron transfer and is also impermeable for other electrolyte components[33],[85]. The phenomenon of the SEI formation is unique for lithium and its compounds. The battery performance, the irreversible charge loss, the rate capability, the cycleability, the exfoliation especially in terms of graphite and the safety of the cell are mainly influenced by the quality of the solid electrolyte interphase.

In general, the SEI layer formed in organic solvent based electrolytes comprises (Figure 38)[33]:

- A thick, porous, electrolyte permeable film of organic (polymeric and oligomeric) decomposition products
- A thin, compact, electrolyte impermeable film of inorganic decomposition products

Thus, it can be recorded that the composition of the SEI is critically influenced by the chemical structure of the electrolyte solvents. In organic solvent-based electrolytes the SEI-formation is irreversible.

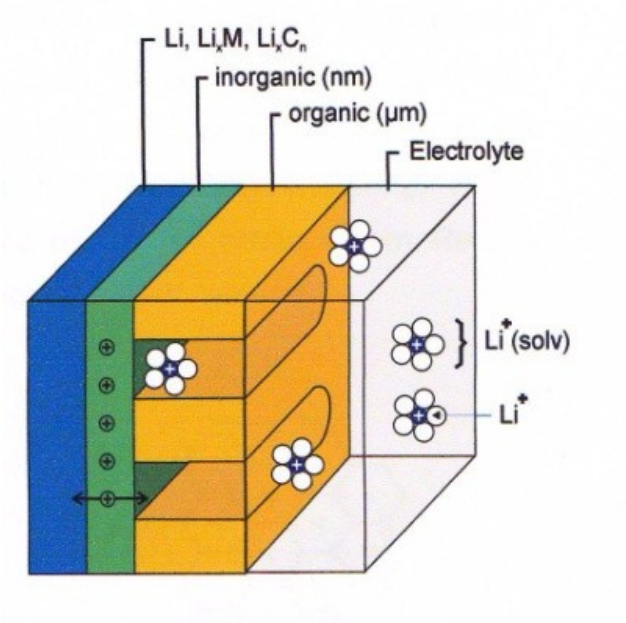

Figure 38: Schematic drawing of the solid electrolyte interphase[33]

3.2.7 Separators

A separator is a porous membrane, which is placed between the anode and the cathode, whereby the pores are filled with the liquid electrolyte. The main function of a separator is to permit the ionic flow but to prevent the electron flow within a cell and, hence, to prevent an electrical short circuit. Beyond that, a separator should have a good wettability with the liquid electrolyte, a high chemical stability against the electrolyte, a high mechanical and dimensional stability and a sufficient physical strength to ensure an easy handling [86]. The common separators related to the use of liquid electrolytes are microporous polyolefins, like polypropylene (PP), polyethylene (PE) and a combination of them (PP/PE/PP). Lithium-ion batteries with gel-type polymer electrolytes especially use microporous separators made of PVdF or PVdF coated microporous polyolefin separators. In lithium-ion batteries with a solid polymer electrolyte the solid electrolyte acts as separator as well as electrolyte[87].

4 Experimental Setups and Methods of Investigation

Electrode Preparation ProcessFigure 39 illustrates two flow diagrams of the electrode preparation process in the Experimental Part 1 (left flow diagram) and the Experimental Part 2 (right flow diagram). The chapters 4.1.1 (page 47) and 4.1.2 (page 48) dwell upon the within the flow diagrams blue emphasized working steps.

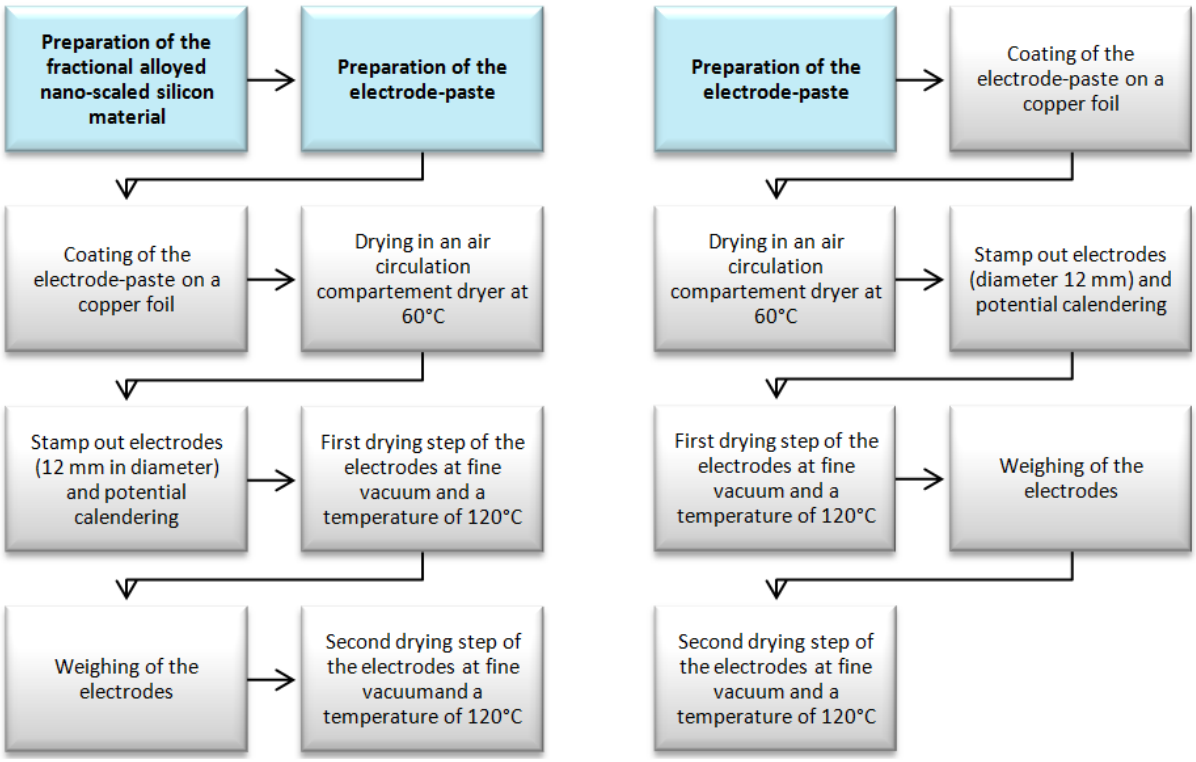

Figure 39: Flow diagrams of the electrode preparation process in Experimental Part 1 (left) and in Experimental Part 2 (right)

4.1.1 Preparation of the Fractional Alloyed Nano-Scaled Silicon Material

The preparation of the fractional alloyed nano-scaled silicon powder is made by two different ways:

- Preliminary fractional alloying from the gaseous phase
- Preliminary fractional alloying by solid state diffusion

4.1.1.1 Preliminary Fractional Alloying from the Gaseous Phase

The preliminary alloying from the gaseous phase is made at vacuum by a glass tube furnish of the type B-585 of the firm Büchi and a special glass device (V = 200 cm^3; Figure 40). The nano-scaled silicon powder was preliminary fractional alloyed from the gaseous phase with the elements sodium (Na; Riedel-de Haën) and potassium (K; Sigma-Aldrich).

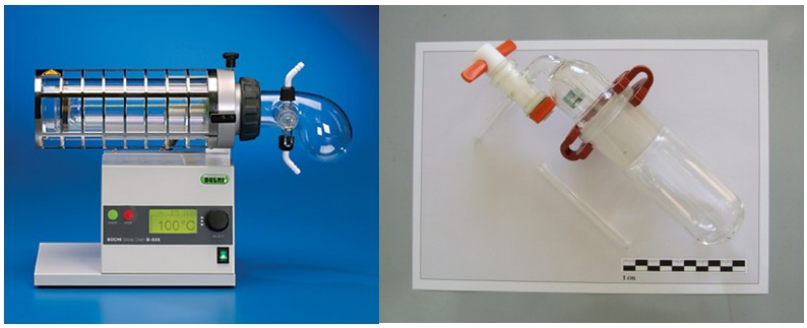

Figure 40: The glass tube furnish B-585 of the firm Büchi (left)[88] and the special device for the preliminary fractional alloying process from the gaseous phase (right)

4.1.1.2 Preliminary Fractional Alloying by Solid State Diffusion

The preliminary alloying by solid state diffusion is made at argon atmosphere by a glass tube furnish of the type AHT (Figure 41, left picture). The nano-scaled silicon powder was preliminary fractional alloyed by solid state diffusion with a sodium/potassium (22 % Na/78 % K; Sigma-Aldrich) alloy and the elements calcium (Ca; Sigma-Aldrich) and magnesium (Mg; Merck). In case of the preliminary alloying with calcium and magnesium the nano-scaled silicon powder and the alloying metal are pressed in pellets with a special pressing tool (Figure 41, right picture). In case of the sodium/potassium alloy the nano-scaled silicon powder was pressed in a pellet and the liquid Na/K alloy was dropped in an argon filled glove box (< 1 ppm H_20, < 1 ppm O_2) onto the pellet. After the alloying process the pellet has to be grinded with a agate mortar and a agate prestle.

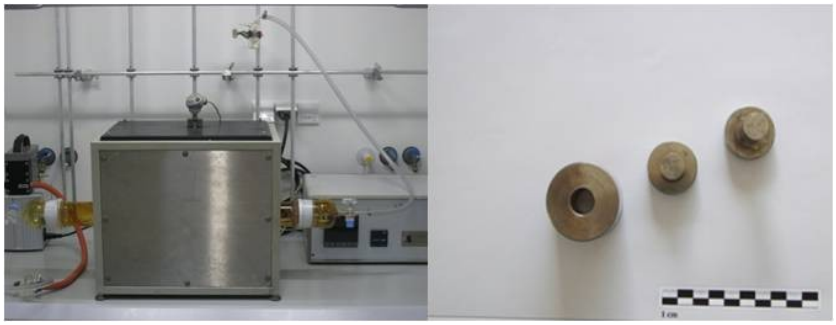

Figure 41: The glass tube furnish for preliminary alloying by solid state diffusion (left) and the special device to press pellets (right)

4.1.2 Preparation of the Electrode-Paste

The electrode-paste, or electrode-slurry, is made by mixing the active material powder, the binder powder, the solvent and additives (i.e. conductive additive) on a magnetic stirrer into a paste.

4.1.2.1 Standard Silicon Electrode-Paste Preparation

The standard silicon electrode-slurry composition is shown in Table 5.

Table 5: Standard silicon electrode-slurry composition

Composition [%]	Function	Compound
8	binder	Na-CMC (Wolff Celluloses GmbH & Co. KG)
80	active material powder	nano-scaled silicon powder
12	conductive additive	carbon black (Super P; Timcal)
	solvent	deionised water
2 drops	stabilizing agent	tenside (potassium polyarylphenyl ether phosphate; Rhodia)

The standard silicon electrode-paste is made by the following dispersing-sequence:

1. Dissolving the binder in the solvent
2. Adding the active material powder
3. Adding the conductive additive
4. Stirring of the electrode-paste for around 24 h (~700 $r \cdot min^{-1}$)

The coating of the electrode-slurry is made on a coater of the firm Erichsen (model 509 ejector) by the use of hand fountain blade. The used current collector is a copper foil and the wet film thickness is 105 µm.

4.1.2.2 Standard Silicon/Graphite Composite Electrode-Paste Preparation

The standard silicon electrode-slurry composition in is shown in Table 6.

Table 6: Standard silicon/graphite composite electrode-slurry composition

Composition [%]	Function	Compound
8	binder	Na-CMC (Wolff Celluloses GmbH & Co. KG)
20	active material powder I	nano-scaled silicon powder
62	active material powder II	graphite
10	conductive additive	carbon black (Super P; Timcal)
	solvent	deionised water
2 drops	stabilizing agent	tenside (potassium polyarylphenyl ether phosphate; Rhodia)

The standard silicon electrode-paste is made by the following dispersing-sequence:

1. Dissolving the binder in the solvent
2. Adding the active material powder I
3. Ultrasonic treatment (30 s, 30 % power)
4. Adding the conductive additive
5. Adding the active material powder II
6. Stirring of the electrode-paste for around 24 h (~700 $r \cdot min^{-1}$)

The coating of the electrode-slurry is also made on a coater of the firm Erichsen (model 509 ejector) by the use of hand fountain blade. The used current collector is a copper foil and the wet film thickness varies between 60 µm and 100 µm.

4.2 Electrochemical Measurements

4.2.1 Cyclovoltammetry

The cyclovoltammetry is also called “triangle voltage method”. This name is based on the triangular voltage flow, which arise out of applying at first an increasing potential and then a decreasing potential (or vice versa) at a working electrode (Figure 42).

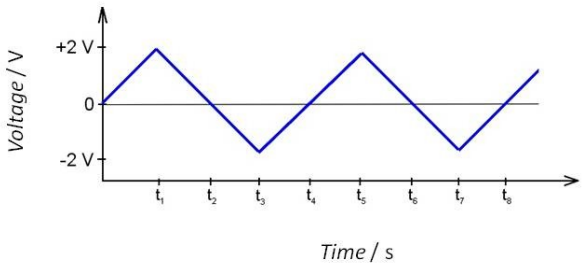

Figure 42: Voltage flow in case of cyclovoltammetry[89]

The current I, which is necessary to retain the applied voltage U, is recorded and applied against a given voltage (voltage advance velocity [$V \cdot s^{-1}$]). If an electrochemical reaction occurs a current flow is observable.

For the common potentiostatic measurements a three electrode assembly with a reference electrode (RE), a working electrode (WE) and a counter electrode (CE) is used. Between the WE and the CE a required voltage is applied, whereby the RE act as zero point potential. If an electrochemical reaction at the WE occurs the voltage between the WE and the CE varies by the reason of different kinds of overvoltages. This voltage difference is recorded by a potentiostatic device, which align the voltage with the required voltage by being live between the WE and the CE. Figure 43 illustrates a typical cyclovoltammogramm of a graphite (KS 6) anode vs. Li/Li^+.

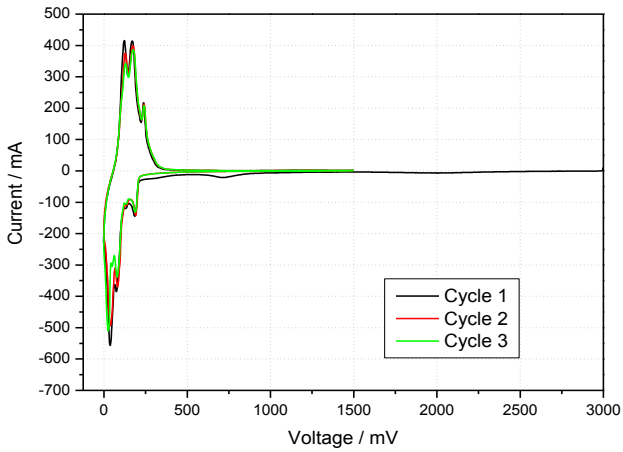

Figure 43: Typical cyclovoltammogramm of a graphite (KS 6) anode vs. Li/Li^+; EC/DEC (3:7, v:v), 1 M $LiPF_6$[90]

At the performed cycolvoltammetric measurements metallic lithium constitutes the reference electrode as well as the counter electrode. This is indicated in the following by the term "vs. Li/Li^+" (chapter 0, page 52). The voltage limits in the first cycle are 3 V – 0 V – 1.5 V and in the following cycles 1.5 V – 0 V – 1.5 V. The voltage advance velocity is 30 $\mu V \cdot s^{-1}$. The within this work used potentiostat is manufactured by the company Bio Logic (model VMP 3).

4.2.2 Constant Current Cycling

The constant current cycling measurements were performed on the cycling device Maccor-Test series 4000. The constant current cycling measurements were taken with different test programs (Table 7, Table 8).

Table 7: Test program 1

Rest			4 h
Cycle 1	Constant Current Charging	Lithiation of the anode	0.1 C → 0.1 V
	Constant Voltage Charging	Lithiation of the anode	0.05 C
	Constant Current Discharging	Delithiation of the anode	0.1 C → 1 V
Cycle 2 - 100	Constant Current Charging	Lithiation of the anode	0.5 C → 0.1 V
	Constant Voltage Charging	Lithiation of the anode	1 h
	Constant Current Discharging	Delithiation of the anode	0.5 C → 1 V

Table 8: Test program 2

Rest			4 h
Cycle 1	Constant Current Charging	Lithiation of the anode	0.1 C → 0.05 V
	Constant Voltage Charging	Lithiation of the anode	4 h
	Constant Current Discharging	Delithiation of the anode	0.1 C → 1.5 V
Cycle 2	Constant Current Charging	Lithiation of the anode	0.2 C → 0.05 V
	Constant Voltage Charging	Lithiation of the anode	2 h
	Constant Current Discharging	Delithiation of the anode	0.2 C → 1.5 V
Cycle 3	Constant Current Charging	Lithiation of the anode	0.3 C → 0.05 V
	Constant Voltage Charging	Lithiation of the anode	3 h
	Constant Current Discharging	Delithiation of the anode	0.3 C → 1.5 V
Cycle 3-50	Constant Current Charging	Lithiation of the anode	0.5 C → 0.05 V
	Constant Voltage Charging	Lithiation of the anode	1 h
	Constant Current Discharging	Delithiation of the anode	0.5 C → 1.5 V

Table 9: Test program 3

Rest			4 h
	Constant Current Charging	Lithiation of the anode	0.02 C → 0.00 V / 1,00 C
	Constant Voltage Charging	Lithiation of the anode	2 h / 1,00 C
	Constant Current Discharging	Delithiation of the anode	0.1 C → 1.5 V
Rest			2 h

4.2.3 The Swagelok® test cell

The electrochemical measurements were carried out in Swagelok® test cells (Figure 44). In general, the Swagelok® test cell consists of three current collector punches – the current collector punch for the counter electrode, the current collector punch for the reference electrode and the current collector punch for the working electrode. The main corpus constitutes of a T-shaped, stainless steel device. The Swagelok® cells are assembled in an argon filled glove box (< 1 ppm H_20, < 1 ppm O_2). The used components are:

- **Separator**: 6 x Freudenberg-fleece FS 2190 (polypropylene; thickness: 23 µm) with a diameter of 12 mm; for the constant current cycling measurements additional a Celgard® separator was used
- **Electrolyte**: 120 µl Ethylenecarbonate/Diethylenecarbonate (3:7; v:v); 1 M Lithiumhexafluoro-phosphate; 2 v% Vinylenecarbonate
- **Reference electrode**: metallic lithium
- **Counter electrode**: metallic lithium
- **Working electrode**: prepared electrode

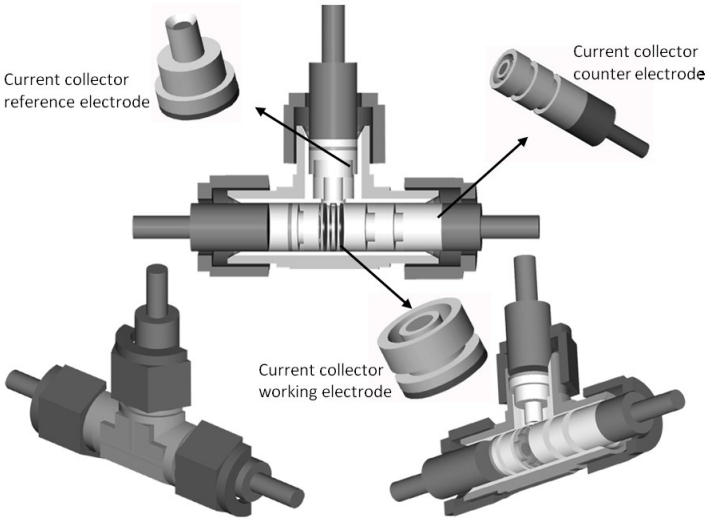

Figure 44: Schematic build-up of a Swagelok® cell

4.3 Scanning Electron Microscopy

A scanning electron microscope (SEM) ranks among the electron microscopes. In general, a SEM consists of (Figure 45):

- A beam generative system
- A XY-diversionary system
- A lens system
- A detector
- An electronic signal processing
- A sample chamber
- A vacuum pump system

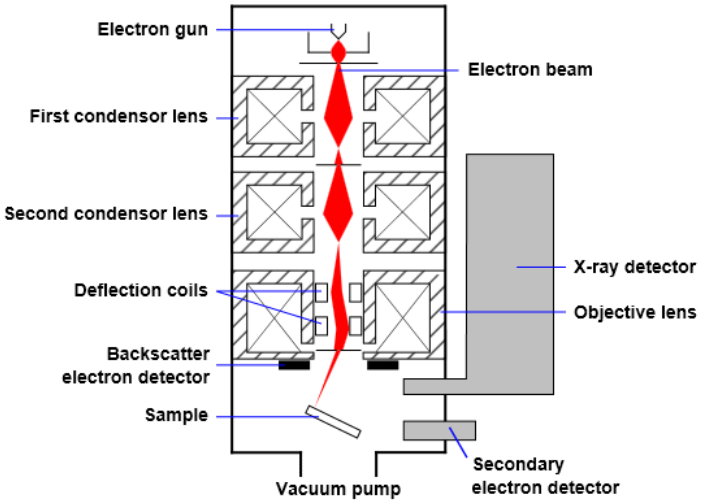

Figure 45: Schematic setup of a scanning electron microscope[91]

The high energy primary electron beam is led point by point across the sample. The electrons of the primary beam interact with the atoms of the sample and in every point the signal intensity is measured and converted into greyshades. By the use of a suitable calculator a picture of the sample can be generated. The most important types of signals which can be detected by a scanning electron microscope and the corresponding detector types are:

- Secondary electrons ↔ secondary electron detector
- Back-scattered electrons ↔ back-scattered electron detector
- X-rays ↔ energy-dispersive detector

Thus, the produced signals mainly contain information about the topography and the composition of the sample.

Figure 46 illustrates a picture of the in the course of this work used scanning electron microscope manufactured by the company Tescan (model Vega 3 SBU). The energy dispersive detector is manufactured by the company Oxford Instruments (model INCA x-act 51ADD0007).

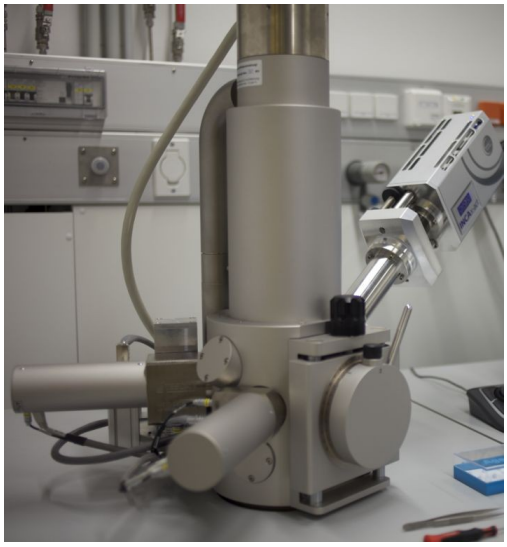

Figure 46: The SEM Vega 3 SBU

4.4 X-Ray Diffraction

With the aid of X-ray diffraction (XRD) it is possible to make a point of the atomic structure of a material. This analytical technique is based on the elastic scattering of X-rays from the electron clouds of the different atoms within a sample. Figure 47 illustrates a possible setup of a X-ray diffractometer.

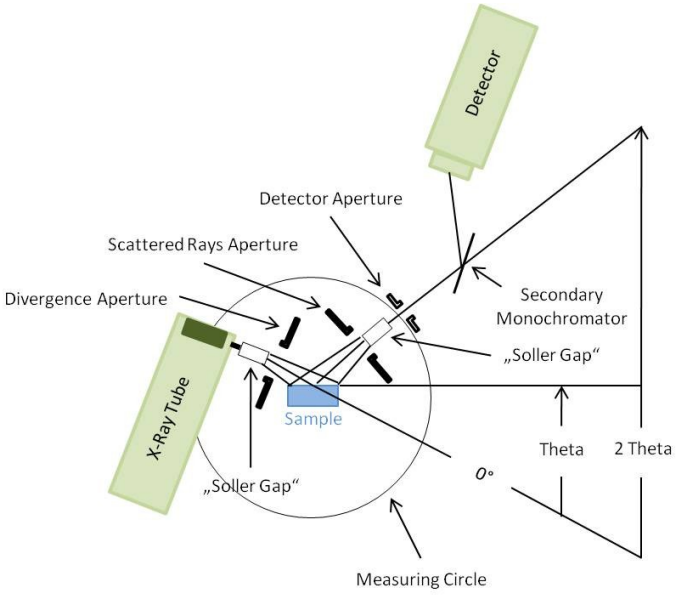

Figure 47: Schematic setup of a XRD (example)

In general, it is necessary to distinguish between several X-ray diffraction techniques, whereby the most common are[92]:

- **The single-crystal X-ray diffraction.**

  Single crystal diffraction is used to investigate the complete structure of a crystalline sample.

- **The powder diffraction.**

  The powder diffraction is the most commonly used technique. It is possible to characterize and identify unknown polycrystalline and (mixed) solid samples, whereby terms like the crystallographic structure, the grain size and the preferred orientation can be determined.

- **The high-resolution X-ray diffraction.**

  With the aid of high-resolution X-ray diffraction it is possible to investigate the thickness, the crystallographic structure and the strain in thin epitaxial films.

In the course of this work a X-ray diffractometer manufactured by the company Bruker (model D8 Advance) was used (Figure 48, left). Figure 48 (right) also illustrates the special designed sealed cell for the ex-situ XRD measurements of uncycled/cycled electrodes.

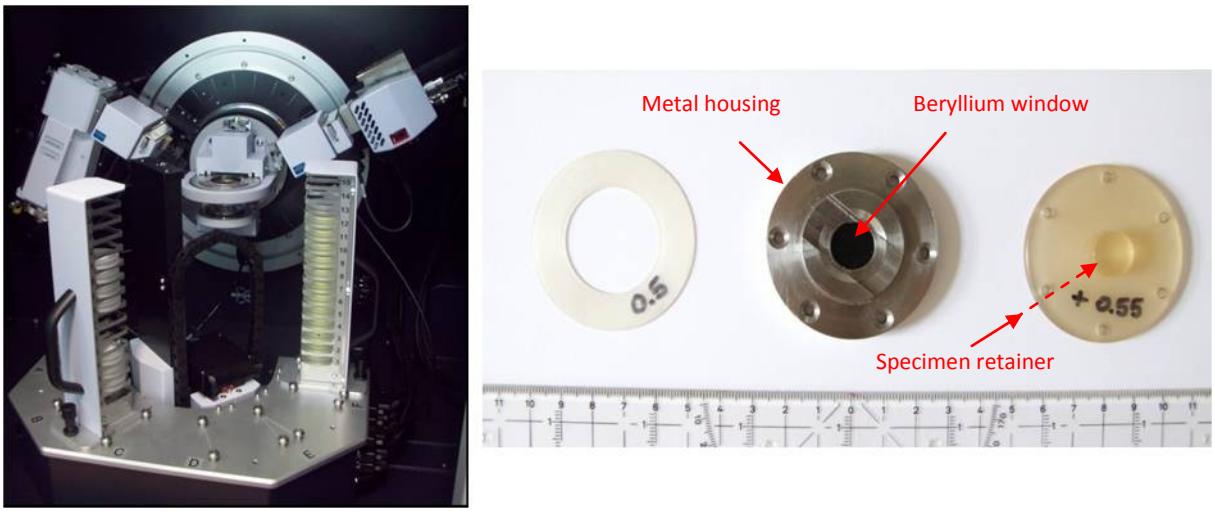

Figure 48: X-ray diffractometer D8 Advance (left) and the special designed sealed cell for the ex-situ XRD measurements of uncycled/cycled electrodes (right)

4.5 Gas Chromatography – Mass Spectrometry

The coupling of a gas chromatograph (GC) with a mass spectrometer (MS) enables the quantitative and qualitative identification of individual substances within a test sample. Figure 49 illustrates a schematic setup of a GC-MS. As its name implies a GC-MS consists of two major units – a gas chromatograph and a mass spectrometer. The gas chromatograph is responsible for the fractionation of the particular substances within the sample and the mass spectrometer is responsible for the qualitative and quantitative analysis of the particular components.

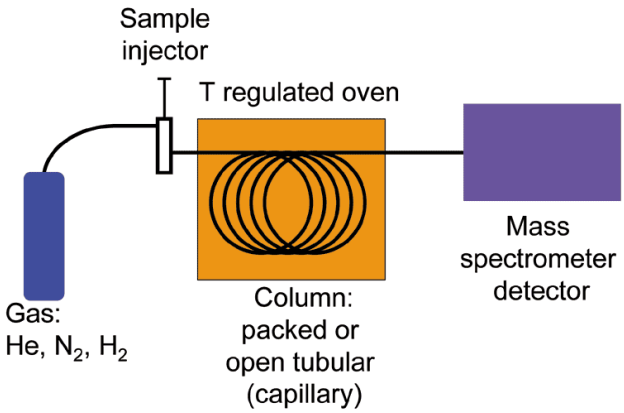

Figure 49: Schematic setup of a gas chromatograph – mass spectrometer coupling[93]

Figure 50 illustrates a picture of the in the course of this work used GC-MS "Agilent G1701EA GC/MSD ChemStation".

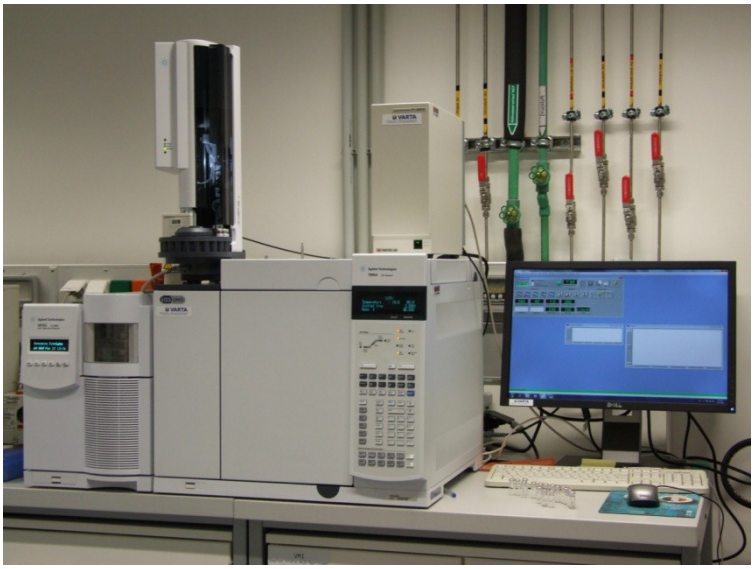

Figure 50: The Agilent G1701EA GC/MSD ChemStation

Within this work we used the GC-MS to investigate possible residuals of the plasticizer triethylcitrate (TEC) within the electrode after several drying steps (chapter 6, page 92). The preparation of the samples is shown in the flow diagram in Figure 51.

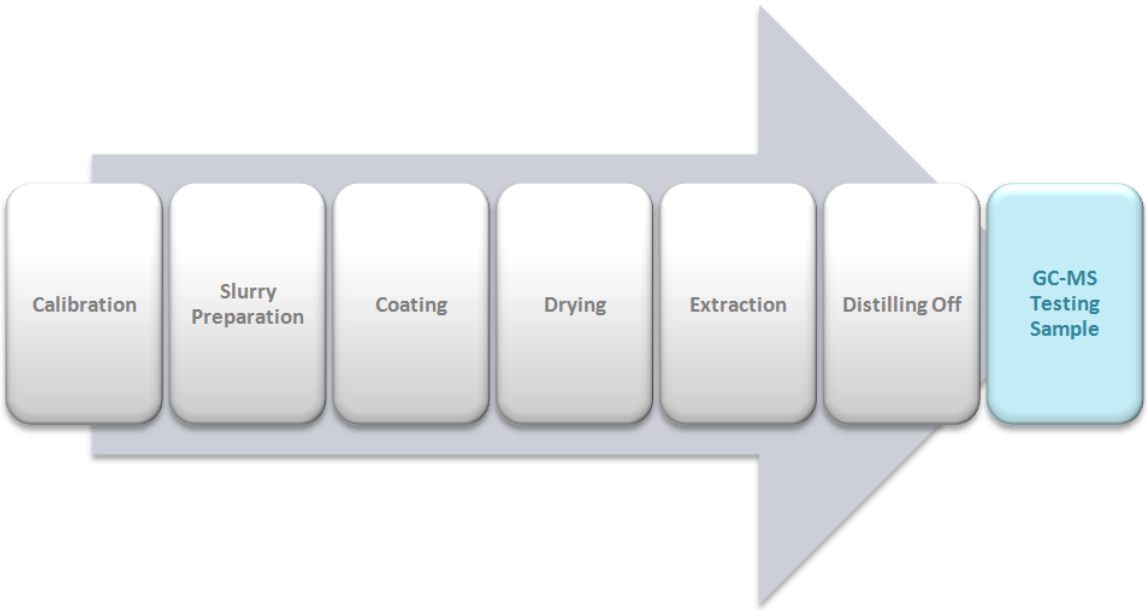

Figure 51: Flow diagram of the GC-MS testing sample preparation process

- **Calibration** →Manufacturing of four calibration standards:
  - 8 ppm TEC in acetone (puriss.)
  - 40 ppm TEC in acetone (puriss.)
  - 200 ppm TEC in acetone (puriss.)
  - 1000 ppm TEC ion acetone (puriss.)
- **Slurry Preparation**: In this connection a standard silicon/graphite composite electrode-paste according to chapter 4.1.2.2 (page 49) was prepared. 10 w% (calculated from the used overall solid mass of the electrode-paste) of triethylcitrate were added after point 1 of the dispersing sequence (dissolving the Na-CMC binder in distilled water; page 49).
- **Coating**: Coating of the electrode paste on a copper foil (wet film thickness: 150 µm) → electrode.
- **Drying**: Surface drying of the electrode within an air circulation compartment dryer (ULTS) at a temperature of around 60°C (~30 min). Subsequently drying of the electrode within a glass tube furnish (GRO) at fine vacuum and a temperature of around 120°C (~5 h and 18 h).
- **Extraction**: "Soxhlett" extraction of the whole electrode with distilled acetone (puriss).
- **Distilling Off**: Removing the solvent and transferring the residual into a rotary evaporator.

5 Experimental Part 1: Fractional Preliminary Alloying of Nano-Scaled Silicon as Active Material for the Negative Electrode in Lithium-Ion Batteries

5.1 Background and Motivation

As already mentioned in chapter 3.2.2.2 (page 29) silicon can alloy with lithium. On consideration of the Li-Si binary phase diagram it can be determined that each silicon atom can accommodate 4.4 lithium-ions (Figure 53)[47]. This leads to the formation of a $Li_{22}Si_5$ phase, which corresponds to a theoretical specific capacity of 4199 mAh·g^{-1} (Table 10).

In 1981 R.A. Huggins et al. first reported the use of lithium-metal alloys (Li_ySi) as negative electrode material. By use of coulometric titration technique at elevated temperature (420°C; molten LiCl-KCl electrolyte) the four intermediate phases $Li_{12}Si_7$ ($Li_{1.71}Si$), Li_7Si_3 ($Li_{2.83}Si$), $Li_{13}Si_4$ ($Li_{3.25}Si$) and $Li_{22}Si_5$ ($Li_{4.40}Si$) could be identified (Figure 52)[94].

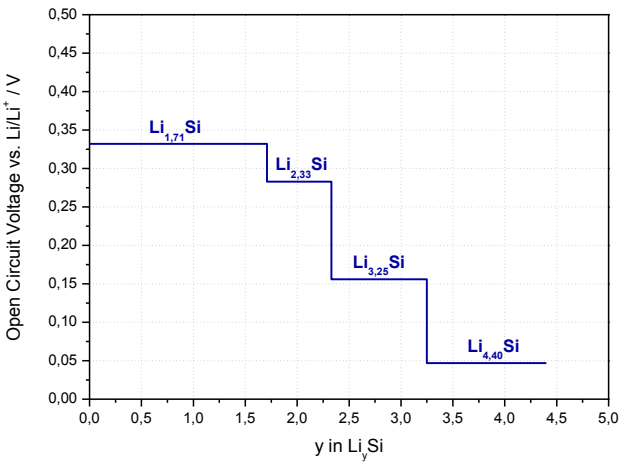

Figure 52: Coulometric titration curve of Li-Si[94]

Table 10 point up chemical and physical properties of the four intermediate phases of the Li-Si system at 415°C. These data show that it is possible to enhance the cycling performance of a silicon electrode through a controlling of the state of charge by coulomb counting or by controlling the cut-off voltage and consequently a controlling of the volume expansion.

Table 10: Chemical and physical properties of the four intermediate phases of the Li-Si system at 400°C[36]

Stoichiometry		Molar mass of the alloy [g·mol^{-1}]	Specific capacity excl. lithium [mAh·g^{-1}]	Potential vs. Li/Li$^+$ [V]	Crystal structure	Density [g·cm^{-3}]	Volume expansion [%]
Si					cubic		
$Li_{1,71}Si$	$Li_{12}Si_7$	40.0	1636	0.332	orthorhombic	1.15	190
$Li_{2,33}Si$	Li_7Si_3	44.3	2227	0.283	rhomohedral	1.43	158
$Li_{3,25}Si$	$Li_{13}Si_4$	50.6	3101	0.156	orthorhombic	1.38	206
$Li_{4,40}Si$	$Li_{22}Si_5$	58.6	4199	0.047	cubic	1.18	314

Contrary to the lithiation of silicon at elevated temperatures (~ 400°C) another behavior is observed at room temperature. In 2000 H. Li et al. suggests that the lithiation of silicon at room temperature destroys the crystal structure of silicon and subsequent a metastable amorphous Li-Si alloy is formed. During further delithiation a recrystallisation occurs. Furthermore, it can be observed that the nano-sized silicon particles merge together after the lithium-insertion/extraction[95]. P. Limthongkul et al. identified the Gibbs free energy of the four known crystalline phases (at equilibrium) and of the metastable amorphous phase (Figure 53). The crystalline phases at equilibrium show lower Gibbs free energies than the amorphous Li-Si phase. Thus, it seems that by season of a kinetic inhibition at room temperature it is not possible to decrease the free enthalpy to reach the thermodynamic equilibrium[96].

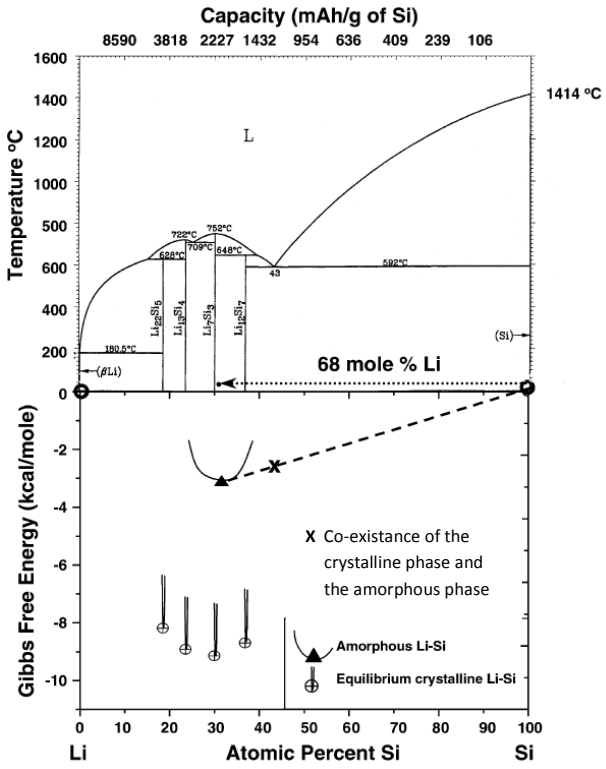

Figure 53: Li-Si binary phase diagram (top) and the corresponding Gibbs free energy diagram (bottom) of the known crystalline and amorphous Li-Si phases (at elevated temperature) [96]

M. N. Obrovac and L. Christensen confirmed by X-ray diffraction in their work the abovementioned amorphization of crystalline silicon at room temperature during lithiation. They observed that the highly lithiated amorphous silicon suddenly crystallizes into a $Li_{15}Si_4$ ($Li_{3,75}Si$) phase at about 50 mV vs. Li/Li^+. J. Li and J. R. Dahn also investigated by in situ X-ray diffraction the reaction of lithium with crystalline silicon at room temperature. They confirmed that crystalline silicon becomes amorphous during lithiation and that this amorphous phase suddenly crystallizes at about 60 mV vs. Li/Li^+ into a $Li_{15}Si_4$ phase (Eq. 30). This fully lithiated state at room temperature ($Li_{15}Si_4$) corresponds to a specific capacity of only about 3579 $mAh \cdot g^{-1}$. During delithiation the $Li_{15}Si_4$ phase coexists with an amorphous Li_ySi phase (Eq. 31). Electrochemical investigations show that cycling over 60 mV improves the performance of the silicon electrode[97],[98],[99].

$$Si\ (crystalline) + \ xLi^+ + xe^- \rightarrow Li_xSi\ (amorphous) + (3{,}75 - x)Li^+ + (3{,}75 - x)e^- \rightarrow Li_{15}Si_4\ (crystalline)$$

Eq. 30

$$Si_{15}\,Li_4\ (crystalline) \rightarrow Si\ (amorphous) + vLi^+ + ve^- + Li_{15}Si_4\ (residual)$$

Eq. 31

Deduced from the calculations of Y. Kubota the Gibbs free energy of the $Li_{15}Si_4$ phase can be generated (Eq. 32)[100].

$$\Delta G_r = \Delta E_r = E_r\left[Li_{\frac{15}{4}}Si\right] - \frac{15}{4}E_r[Li] - E_r[Si] = -1.136\ eV \equiv -4.351 \cdot 10^{-23} kcal$$

G_r …Gibbs free energy
E_r …internal energy

Eq. 32

Multiplied this result by the Avogadro´s constant and divided by 15/4 a Gibbs free energy for the $Li_{15}Si_4$ phase of ***-6.987 kcal·mol^{-1}*** appears (Figure 54).

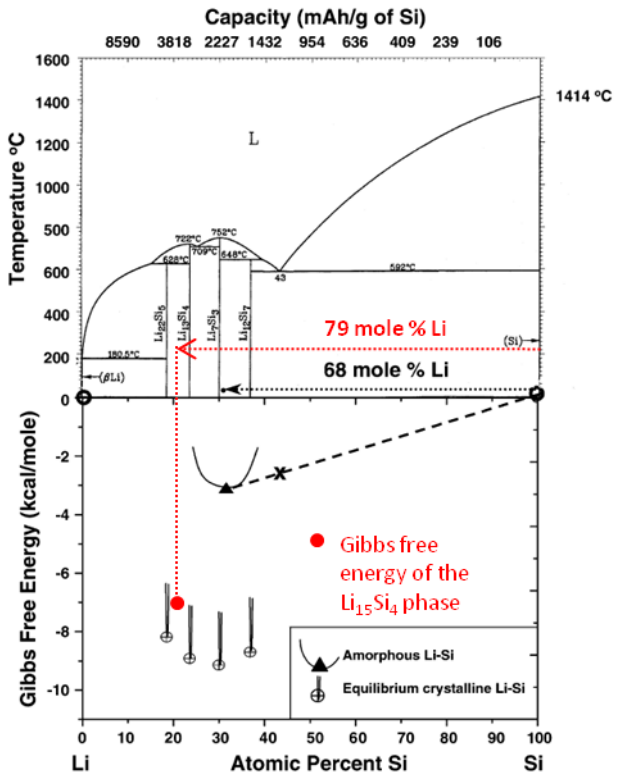

Figure 54: Li-Si binary phase diagram (top) and the corresponding Gibbs free energy diagram (bottom) of the known crystalline and amorphous Li-Si phases at elevated temperature and room temperature[96]

Hence, after consideration of all abovementioned investigations and results, the highly lithiated phase at elevated temperature is the $Li_{22}Si_5$ phase with a corresponding theoretical specific capacity of 4199 $mAh \cdot g^{-1}$ and at room temperature the $Li_{15}Si_4$ phase with a corresponding theoretical specific capacity of 3579 $mAh \cdot g^{-1}$, although the $Li_{22}Si_5$ phase is the thermodynamically more stable phase. Based on these results it is possible to generate a theoretical specific capacity of a silicon/graphite composite material by using Eq. 33.

$$\frac{(cap_{Si} \cdot x_{Si} + cap_C \cdot x_C)}{(x_{Si} + x_C)}$$

cap_{Si} …theoretical specific capacity of silicon
cap_C …theoretical specific capacity of graphite
x_{Si} …percentage amount of silicon in the electrode-paste (chapter 4.1.2.2, page 49)
x_C …percentage amount of graphite in the electrode-paste (chapter 4.1.2.2, page 49)

Eq. 33

Considering the percentage composition of a standard silicon/graphite composite electrode as already specified in chapter 4.1.2.2 (page 49), the two different highly lithiated states of silicon D and their corresponding theoretical specific capacities and the theoretical specific capacity of 372 mAh·g^{-1} of graphite, we can generate two possible theoretical specific capacities for the silicon/graphite composite (Eq. 34, Eq. 35).

$$\frac{\left(4199\,\frac{mAh}{g}\cdot 0.2 + 372\,\frac{mAh}{g}\cdot 0.62\right)}{0.82} = 1305\,\frac{mAh}{g}$$

Eq. 34

$$\frac{\left(3579\,\frac{mAh}{g}\cdot 0.2 + 372\,\frac{mAh}{g}\cdot 0.62\right)}{0.82} = 1154\,\frac{mAh}{g}$$

Eq. 35

Figure 55 shows the two generated theoretical specific capacities of the silicon/graphite composite material and the constant current cycling of one of those electrodes at room temperature, whereby an average specific capacity of around 1250 mAh·g^{-1}, which is higher than the estimated capacity of 1154 mAh·g^{-1} at room temperature, is observable.

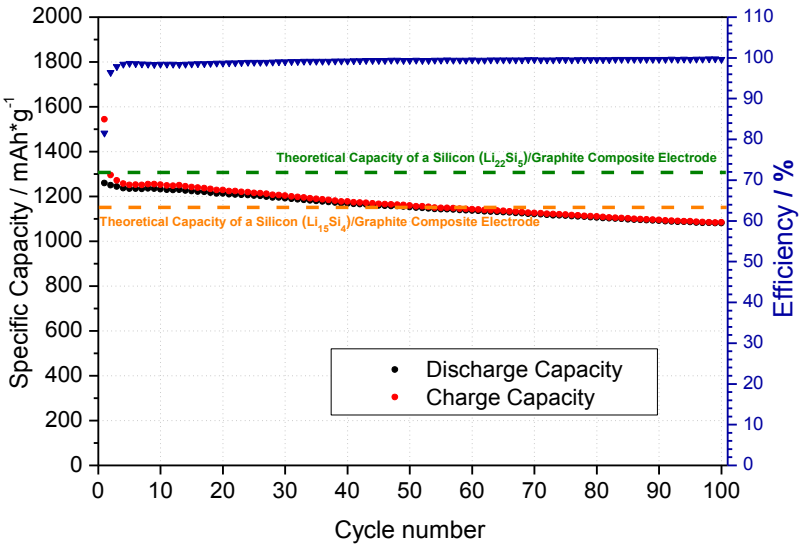

Figure 55: Constant current cycling of a standard silicon/graphite composite electrode and the generated theoretical capacities of a silicon/graphite composite electrode based on the theoretical specific capacity of the $Li_{22}Si_5$ phase (4200 mAh·g^{-1}; green line) and of a silicon/graphite composite electrode based on the theoretical specific capacity of the $Li_{15}Si_4$ phase (3579 mAh·g^{-1}; orange line)

To drill down on this phenomenon of higher capacity than derived by the results from literature possible at room temperature, high resolution transmission electron microscopy (HRTEM) measurements in combination with energy-dispersive X-ray spectroscopy (EDX) measurements were done (Figure 56). These showed impurities of sodium and potassium.

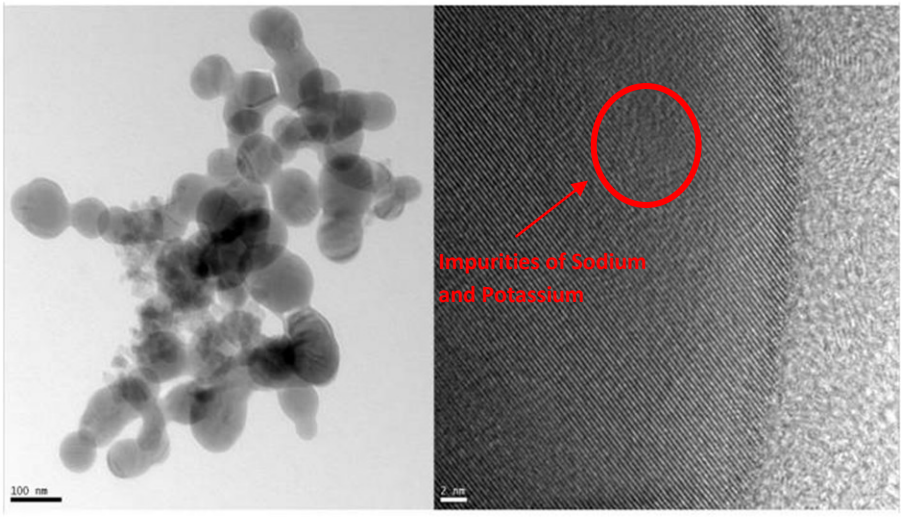

Figure 56: HRTEM measurements of nano-scaled silicon powder (Nanostructured & Amorphous Materials Inc.; 98+%)

By the use of constant current cycling the direct comparison of the nano-scaled silicon powder with impurities of sodium and potassium (silicon produced by the firm Nanostructured and Amorphous Materials, Inc.) and highly pure nano-scaled silicon powder (silicon produced by the firm Evonik formerly known as Degussa) illustrates an enormous increase in capacity of the electrodes made out of the impure powder (Figure 57). In further consequence the pure silicon will be denoted as “silicon D” and the impure silicon as “silicon L”.

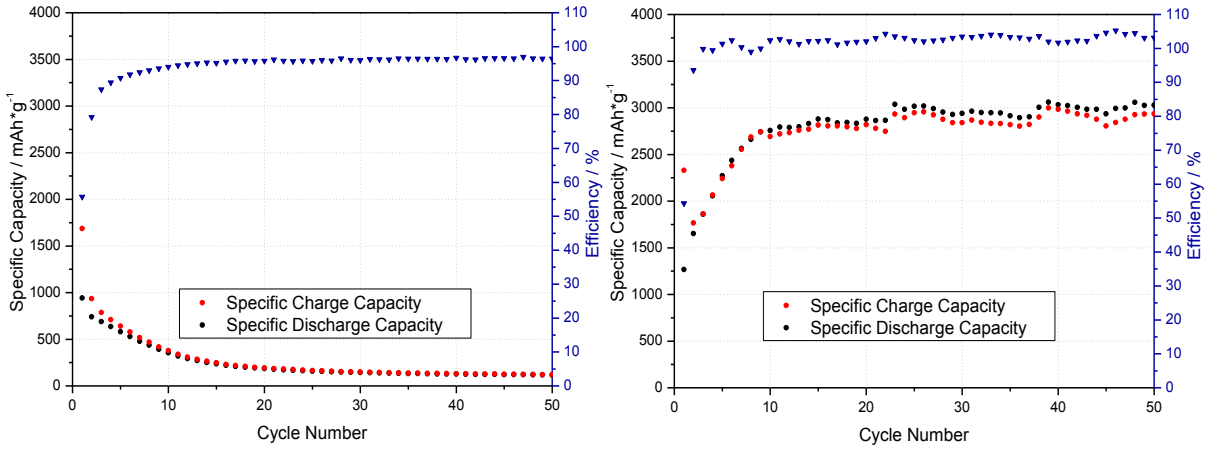

Figure 57: Constant current cycling of silicon D (left) and silicon L (right)

5.2 Experimental Results

5.2.1 Fractional Preliminary Alloying of Nano-Scaled Silicon with Sodium

The fractional preliminary alloying of silicon D with sodium is made from the gaseous phase at vacuum and at 300°C, whereby the vapor pressure of sodium is $1 \cdot 10^{-2}$ mbar at a temperature of 281.85°C[101]. 10 w% (calculated from the used overall solid mass of the nano-scaled silicon D powder) of the sodium metal were used. The evaporating time was around 24 h. Subsequent a standard silicon electrode-slurry according to chapter 4.1.2.1 (page 48) was prepared.

5.2.1.1 Electrochemical Results

Figure 58 shows the cyclovoltammogramm of the unmodified silicon D electrode vs. Li/Li^+ in comparison to the with sodium modified silicon D electrode vs. Li/Li^+.

Figure 59 should illustrate in particular the differences in performance of the two different electrodes from cycle to cycle.

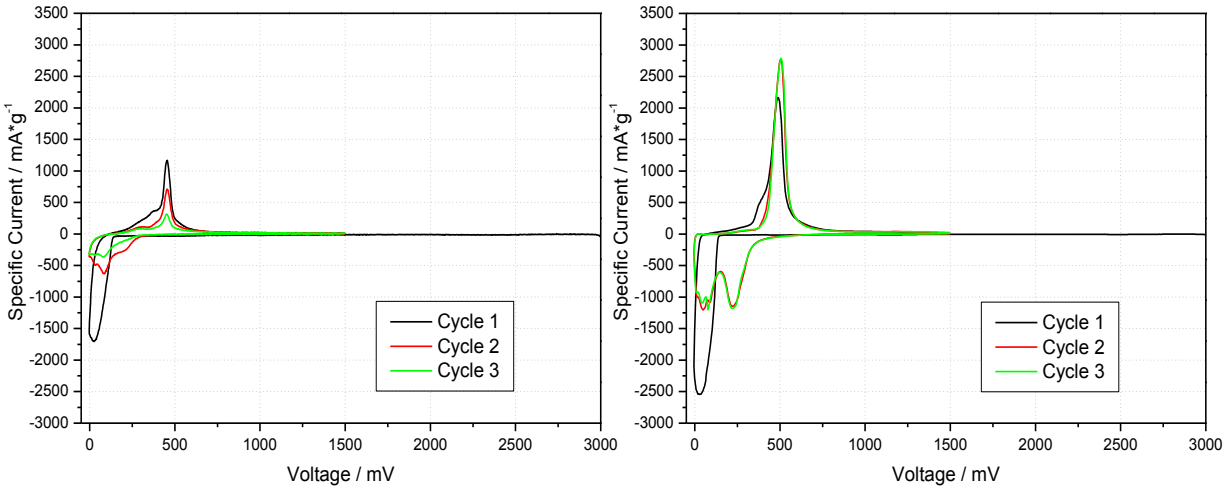

Figure 58: Cyclovoltammogramm of a pure silicon D electrode [m (active layer) = 0,369 mg] vs. Li/Li^+ (left) and a silicon electrode [m (active layer) = 0,339 mg] made out of the with sodium modified silicon D vs. Li/Li^+ (right); EC/DEC (3:7, v:v), 1 M $LiPF_6$, 2 v% VC

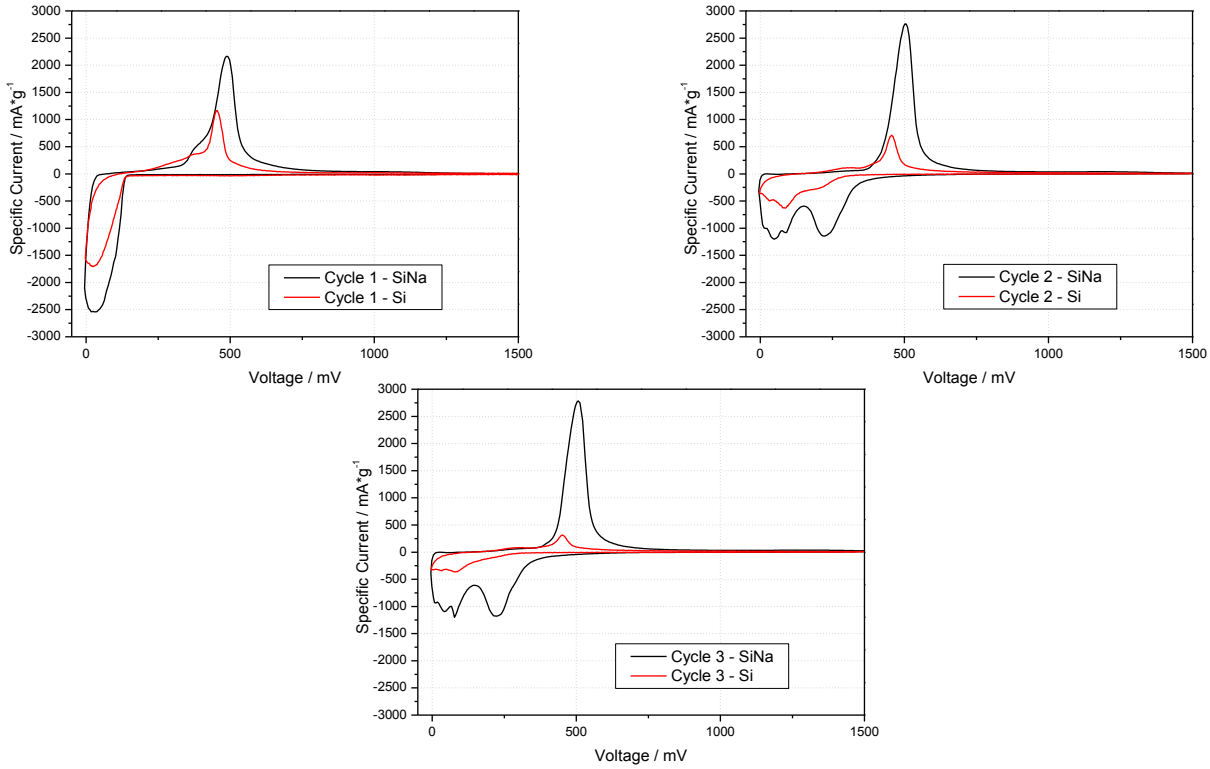

Figure 59: Particular cycles generated from the cyclovoltammogramms in Figure 58

Table 11 and Table 12 show the specific charge capacities, the specific discharge capacities and the efficiencies generated from the cyclovoltammogramms.

Table 11: Specific charge capacity, specific discharge capacity and efficiency generated from the cyclovoltammogramm of the pure silicon D electrode in Figure 58 (left)

Cycle	Specific Charge Capacity [mAh·g^{-1}]	Specific Discharge Capacity [mAh·g^{-1}]	Efficiency [%]
1	1116	658	59
2	536	417	78
3	328	261	80

Table 12: Specific charge capacity, specific discharge capacity and efficiency generated from the cyclovoltammogramm of the silicon D modified with Na electrode in Figure 58 (right)

Cycle	Specific Charge Capacity [mAh·g^{-1}]	Specific Discharge Capacity [mAh·g^{-1}]	Efficiency [%]
1	2974	2663	90
2	2825	2739	97
3	2805	2713	97

Comparing the two cyclovoltammogramms in Figure 58 we can see a higher current flow and consequent higher, sharper current peaks at the cyclovoltammogramm of the with sodium modified silicon D electrode. This is indicative for better reaction kinetics of the modified sample electrode. If we cast a glance to the particular cycles in Figure 59 we can observe, that the electrode performance of the unmodified electrode gets worse from cycle to cycle, whereby the modified electrode gets better. This is also confirmed by the generated charge and discharge capacities. In addition to that the first cycle of the unmodified silicon D electrode shows a very low efficiency in comparison to with the sodium modified silicon electrode (Table 11 and Table 12).

Figure 60 shows the constant current cycling measurements of a silicon D electrode vs. Li/Li^+ and of a silicon D modified with sodium electrode vs. Li/Li^+. The used test program is the test program 1 (chapter 4.2.2; page 51). These measurements confirm the results gained from the cyclovoltammetry. We can observe an enormous improvement in the cycling performance of the electrode by preliminary fractional alloying of the nano-scaled silicon D with sodium. The average discharge capacity is 2000 $mAh \cdot g^{-1}$.

In summary it can be said, that the preliminary fractional alloying of the high purity, nano-scaled silicon powder D with sodium has a positive effect on the performance of the active material. Thus, it can be assumed, that the presence of the sodium decreases the activation energy for the formation of highly lithiated silicon alloys, so that they already formed at room temperature.

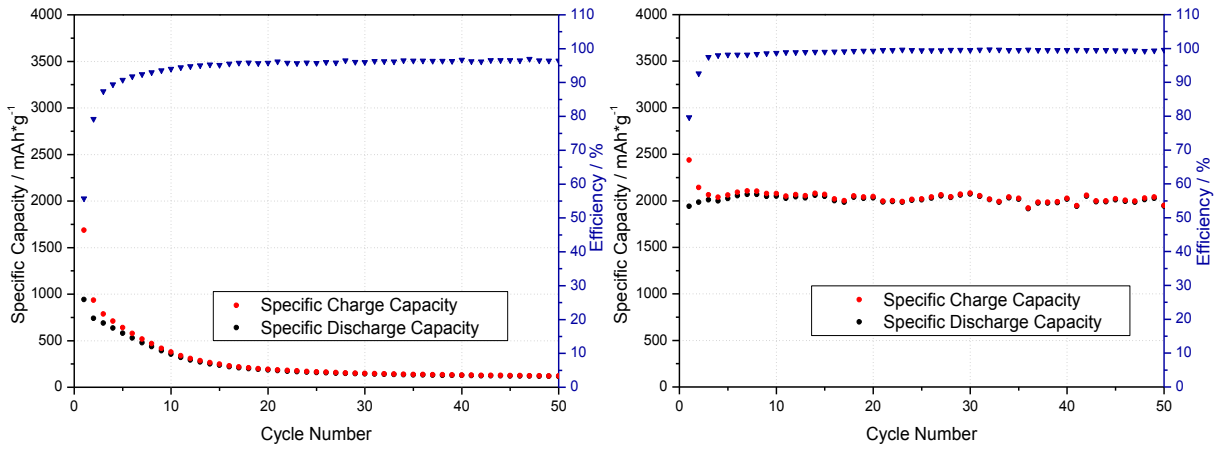

Figure 60: Constant current cycling of a pure silicon D electrode [m (active layer) = 0,233 mg] vs. Li/Li^+ (left) and a silicon D modified with Na electrode [m (active layer) = 0,228 mg] vs. Li/Li^+ (right); EC/DEC (3:7, v:v), 1 M $LiPF_6$, 2 v% VC; test program 1

The variation in evaporating time (48 h and 72 h) of the pure nano-scaled silicon powder doesn`t show an improvement in the cycling performance of the electrode (Figure 61 and Table 13).

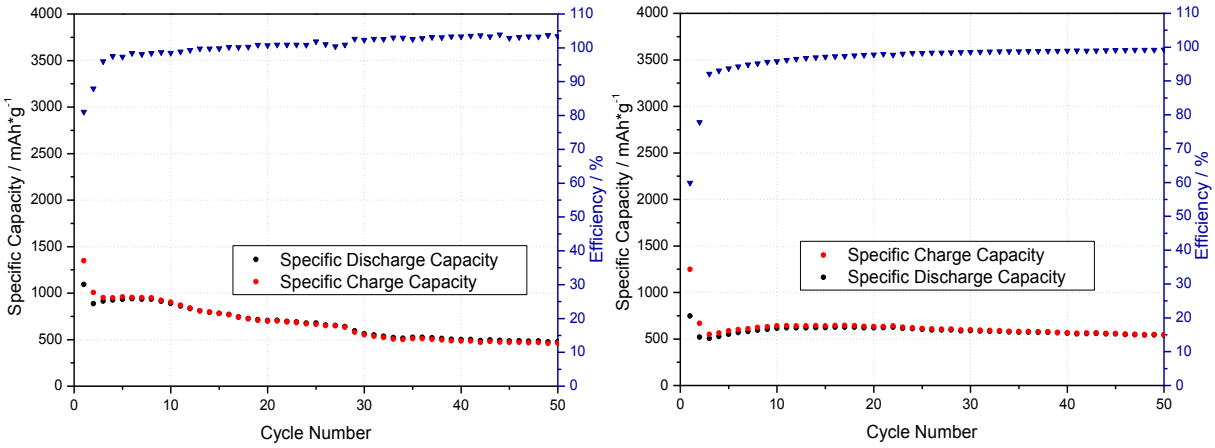

Figure 61: Constant current cycling of a silicon D modified with Na (evaporating time 48 h) electrode [m (active layer) = 0,794 mg] vs. Li/Li^+ (left) and a silicon D modified with Na (evaporating time 72 h) electrode [m (active layer) = 0,714 mg] vs. Li/Li^+ (right); EC/DEC (3:7, v:v), 1 M $LiPF_6$, 2 v% VC; test program 1

Table 13: Average specific discharge capacities of electrodes made out of the with sodium preliminary fractional alloyed nano-scaled silicon powder D with the use of different evaporating times (24 h, 48 h, 72 h)

Evaporating Time [h]	Average Specific Discharge Capacity [$mAh \cdot g^{-1}$]
24	2000
48	600
72	500

5.2.1.2 Analytical Results

By transmission electron microscopy (TEM) measurements in combination with energy-dispersive X-ray spectroscopy (EDX) measurements of the preliminary alloyed nano-scaled silicon powder in comparison with the pure material we could prove the presence of sodium in the for 24 h processed powder (Figure 62, Figure 64 and Table 14) The measurements were performed at the "Felmi – The Austrian Centre for Electron Microscopy and Nanoanalysis".

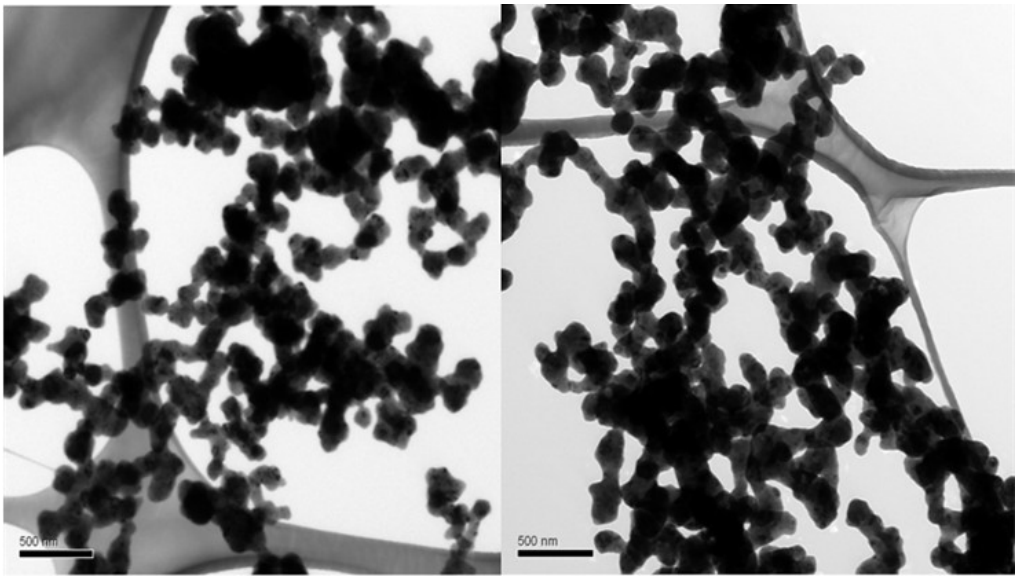

Figure 62: Transmission electron microscopy measurements of the pure nano-scaled silicon powder D (left) and the with sodium preliminary fractional alloyed silicon powder D (24 h) (right)

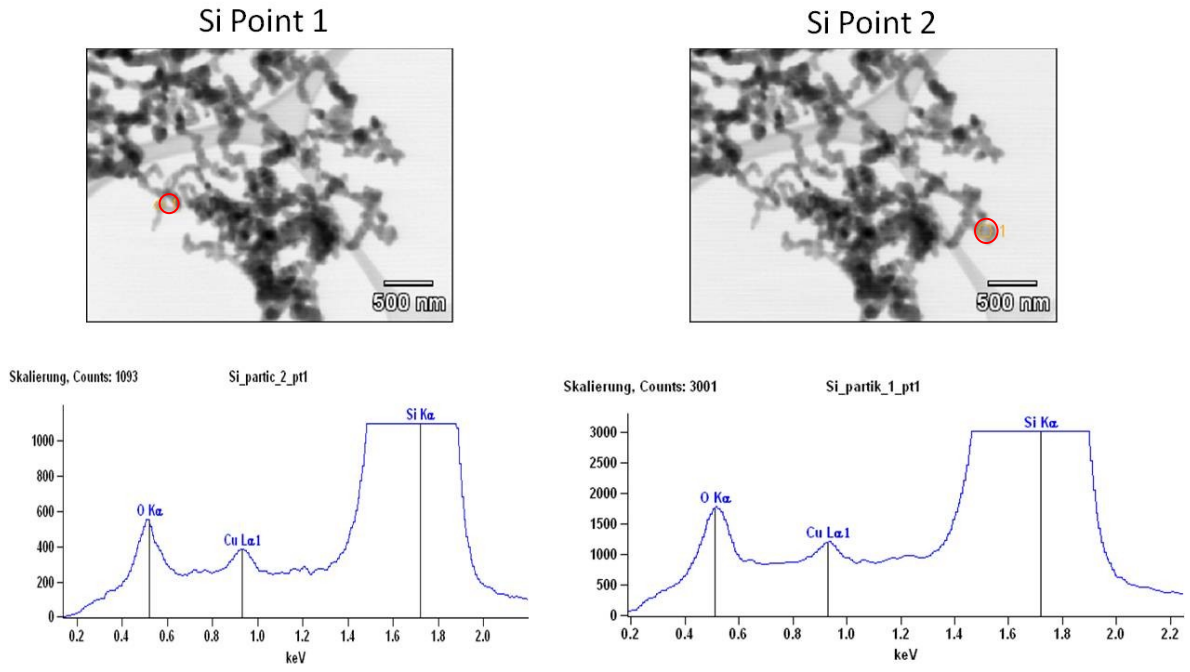

Figure 63: Energy-dispersive X-ray spectroscopy of the pure nano-scaled silicon powder D

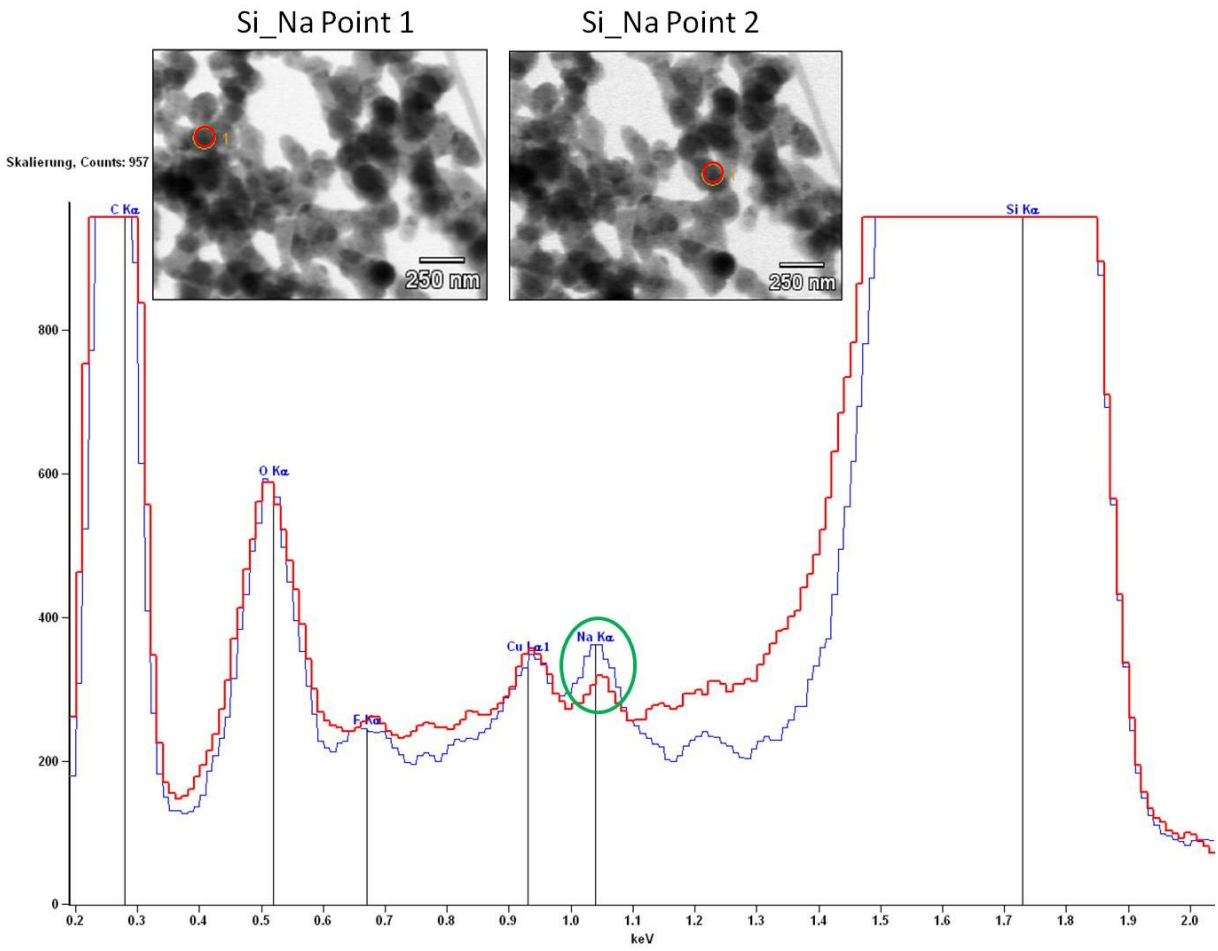

Figure 64: Energy-dispersive X-ray spectroscopy of the with sodium preliminary fractional alloyed silicon powder D (evaporating time 24 h)

Table 14: Mass percent (m%) of sodium within the pure nano-scaled silicon powder D and the with sodium preliminary fractional alloyed silicon powder D (evaporating time 24 h) generated from the energy-dispersive X-ray measurements shown in Figure 63 and Figure 64

Measuring point	*Na-K* [m%]	*Si-K* [m%]
Si Point 1	0.000	100.0
Si Point 2	0.000	100.0
Si_Na Point 1	0.030	99.97
Si_Na Point 2	0.630	99.37

Beyond that, scanning electron microscopy (SEM) measurements in combination with energy-dispersive X-ray spectroscopy (EDX) measurements were done (Figure 65).

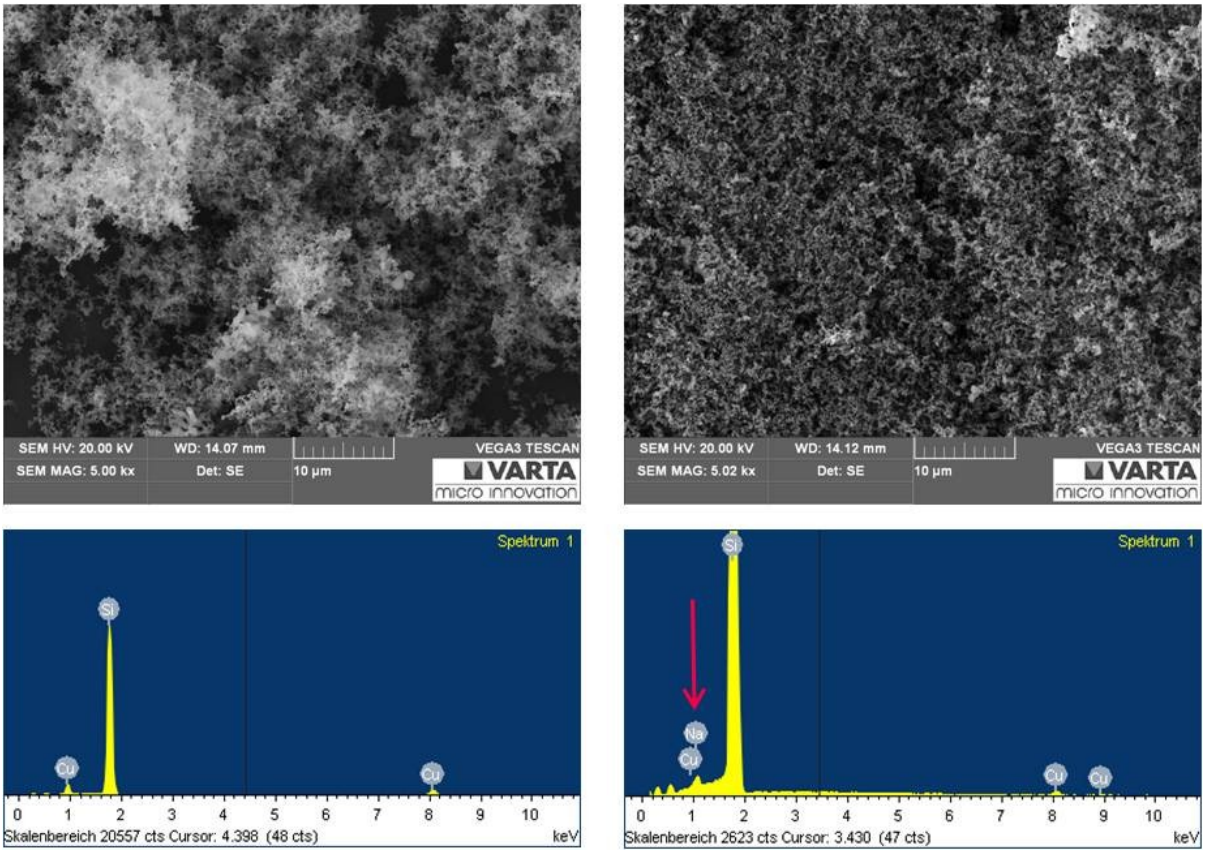

Figure 65: Scanning electron microscopy images (top) and an energy-dispersive X-ray spectroscopy spectra (bottom) of an electrode made out of the pure nano-scaled silicon powder D (left) and an electrode made out of the with sodium preliminary fractional alloyed silicon powder D (evaporating time 24 h) (right)

The two scanning electron microscopy images in Figure 65 illustrates a more compact appearance of the with sodium modified sample electrode. By the way of illustration, Figure 65 also shows an energy-dispersive X-ray spectroscopy spectrum of the silicon electrode made out of the pure silicon D and the silicon electrode made out of the with sodium preliminary fractional alloyed silicon D. Altogether by fives spectra of the unmodified and the modified electrode were generated. The quantitative analysis in m% is shown in Table 15 and Table 16. The energy-dispersive X-ray spectroscopy (EDX) measurements confirm the presence of sodium within the modified electrode.

Table 15: Mass percent (m%) of sodium within the electrode made out of the pure nano-scaled silicon powder D generated from the energy-dispersive X-ray measurements shown in Figure 65

Measuring point	*Na-K* [m%]	*Si-K* [m%]	*Cu-K* [m%]
Point 1	0.000	78.73	21.27
Point 2	0.000	77.78	22.22
Point 3	0.000	69.42	30.58
Point 4	0.000	67.90	32.10
Point 5	0.000	53.98	46.02

Table 16: Mass percent (m%) of sodium within the electrode made out of the with sodium preliminary fractional alloyed silicon powder D (evaporating time 24 h) generated from the energy-dispersive X-ray measurements shown in Figure 65

Measuring point	*Na-K* [m%]	*Si-K* [m%]	*Cu-K* [m%]
Point 1	0.560	97.44	2.000
Point 2	0.990	96.91	2.110
Point 3	0.820	96.80	2.370
Point 4	0.710	97.10	2.190
Point 5	0.520	97.32	2.160

To prove the assumption, that the presence of sodium within the high purity, nano-scaled silicon powder D implicates a decrease of the free enthalpy of the lithium/silicon alloy so that the formation of a higher lithiated phase is consequently favored, X-ray diffraction measurements with a specially designed cell (chapter 4.4, page 54) were performed.

Non cycled electrodes as well as previously cycled electrodes were measured:

- silicon D non cycled
- silicon L cycled
- silicon D cycled
- silicon D preliminary fractional alloyed with sodium cycled

The used test program was the test program 3 (chapter 4.2.2, page 51).

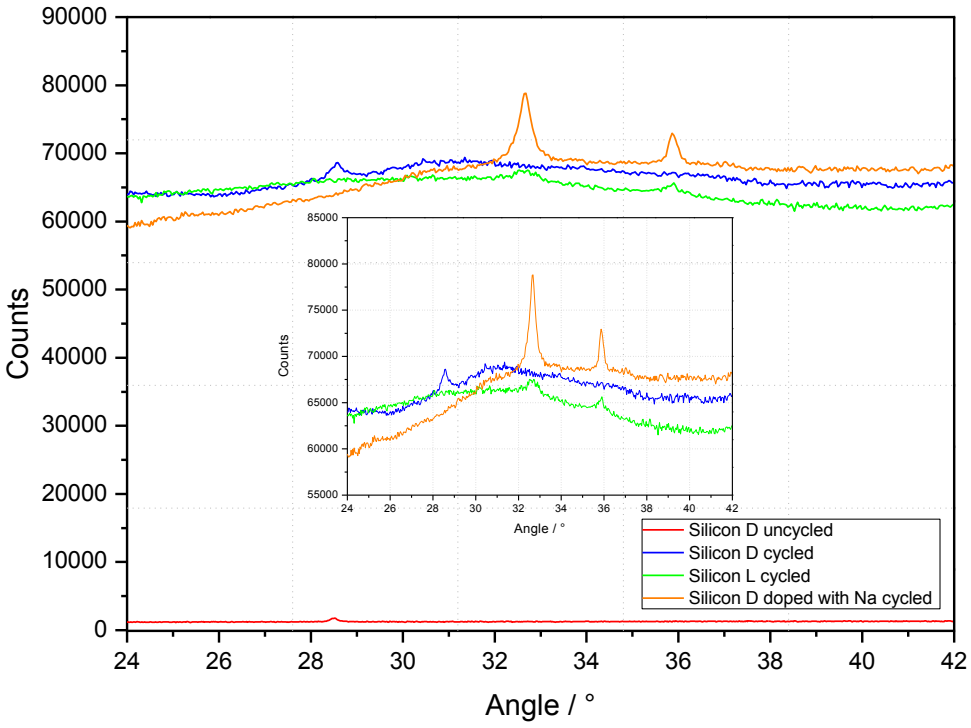

Figure 66: X-ray diffraction measurements of the different silicon samples

The with sodium fractional preliminary alloyed and cycled silicon D electrode and the cycled electrode made out of the impure silicon L show the same peaks at 32,5° and 36°. However, the cycled electrode made out of the pure silicon D doesn´t show these peaks. This awareness and the fact that the base material silicon powder L and the with sodium fractional preliminary alloyed silicon powder D show a consimilar cycling behavior also admit the interpretation that the fractional preliminary alloying of high purity silicon powder has an beneficial effect on the performance of the material. Unfortunately, the observed peaks cannot be assigned to the common lithium/silicon phases or to another “unknown” lithium/silicon phase.

5.2.2 Fractional Preliminary Alloying of Nano-Scaled Silicon with Potassium

The fractional preliminary alloying of silicon D with potassium is made by gaseous phase at vacuum and a temperature of 300°C, whereby the vapor pressure of potassium is 133 mbar at a temperature of 171°C[102]. We used 5 w% (calculated from the used overall solid mass of the nano-scaled silicon D powder) of potassium. The pure silicon D powder was preliminary alloyed for 24 h. Subsequent a standard silicon electrode-slurry according to chapter 4.1.2.1 (page 48) was prepared.

5.2.2.1 Electrochemical Results

Figure 67 shows the cyclovoltammogramm of the unmodified silicon D electrode vs. Li/Li^+ in comparison to with the potassium modified silicon D electrode vs. Li/Li^+. Figure 68 should illustrate in particular the differences in performance of the two different electrodes from cycle to cycle.

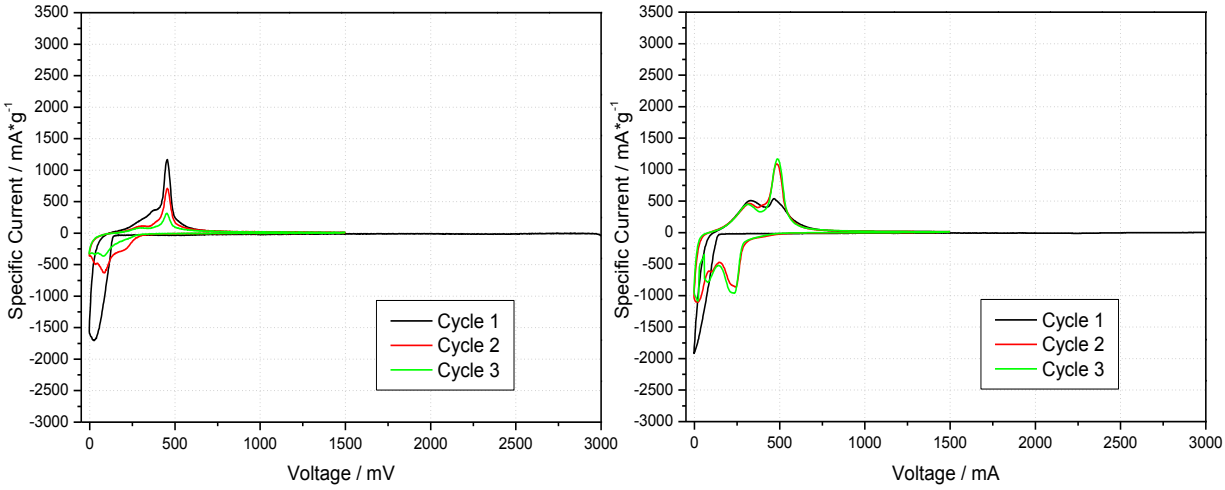

Figure 67: Cyclovoltammogramm of a pure silicon D electrode [m (active layer) = 0,369 mg] vs. Li/Li^+ (left) and a silicon electrode [m (active layer) = 0,554 mg] made out of the with potassium modified silicon D vs. Li/Li^+ (right); EC/DEC (3:7, v:v), 1 M $LiPF_6$, 2 v% VC

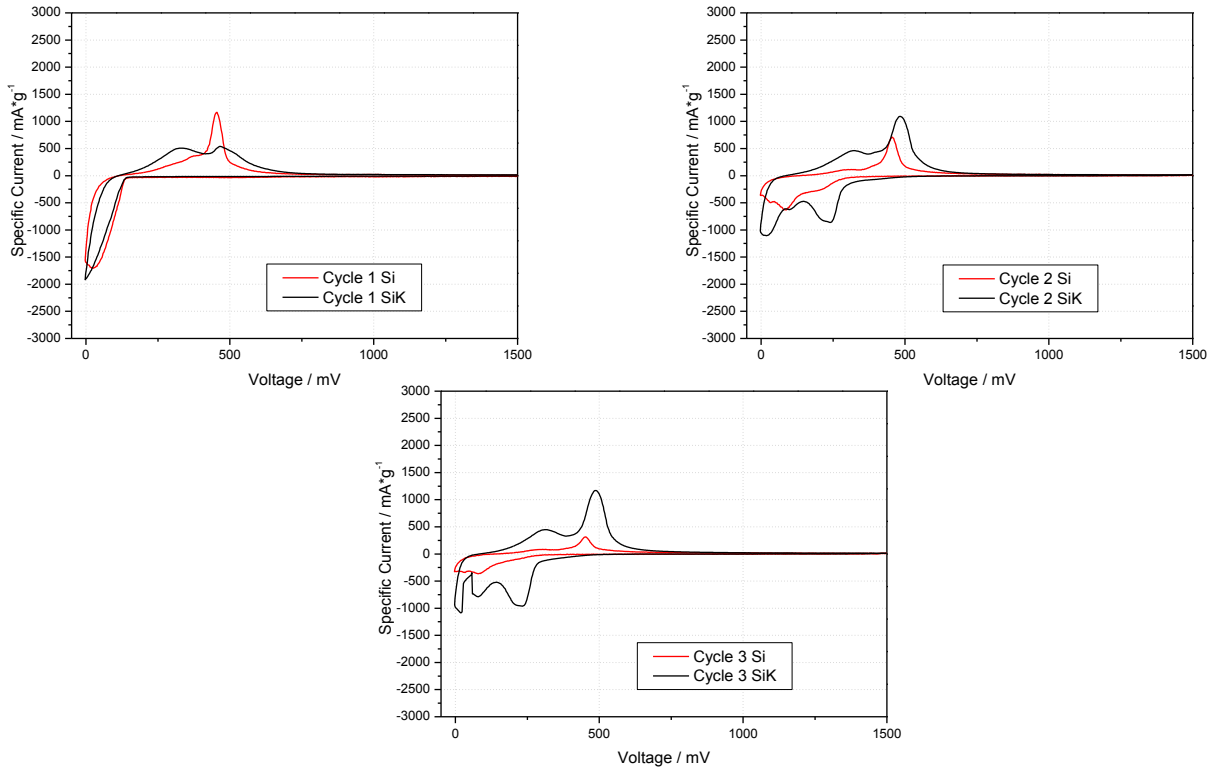

Figure 68: Particular cycles generated from the cyclovoltammogramms in Figure 67

Table 17 and Table 18 show the specific charge capacities, the specific discharge capacities and the efficiencies generated from the cyclovoltammogramms.

Table 17: Specific charge capacity, specific discharge capacity and efficiency generated from the cyclovoltammogramm of the pure silicon D electrode in Figure 67 (left)

Cycle	Specific Charge Capacity [mAh·g^{-1}]	Specific Discharge Capacity [mAh·g^{-1}]	Efficiency [%]
1	1116	658	59
2	536	417	78
3	328	261	80

Table 18: Specific charge capacity, specific discharge capacity and efficiency generated from the cyclovoltammogramm of the silicon D modified with K electrode in Figure 67 (right)

Cycle	Specific Charge Capacity [mAh·g^{-1}]	Specific Discharge Capacity [mAh·g^{-1}]	Efficiency [%]
1	2145	1723	80
2	2243	1999	89
3	2119	1973	93

If we compare the two cyclovoltammogramms in Figure 67 the current flow and the appearance of the current peaks (edge) is nearly the same. Hence, we make an educated guess that the reaction kinetics of the preliminary fractional alloyed sample electrode isn´t better than those of the unmodified sample electrode. The consideration of the particular cycles shows a similar occurrence like the with sodium preliminary alloyed sample electrode – the electrode performance of the unmodified electrode gets worse from cycle to cycle, whereby the modified electrode gets better. This assessment is confirmed by the generated charge and discharge capacities. Beyond that, the pure silicon D electrode shows worse efficiencies than the with potassium preliminary fractional alloyed sample electrode (Table 17 and Table 18). If we compare the with sodium preliminary fractional alloyed silicon electrode (chapter 5.2.1, page 64) and the with potassium preliminary fractional alloyed silicon electrode the former shows a better electrochemical performance.

Figure 69 shows the constant current cycling measurements of a silicon D electrode vs. Li/Li^+ and of a silicon D modified with potassium electrode vs. Li/Li^+. The used test program is the test program 1 (chapter 4.2.2; page 51). An improvement in the cycling performance of the preliminary fractional alloyed silicon D electrode in comparison to the pure silicon D electrode is observeable. Conspicuously is also the improvement in the efficiency. The average discharge capacity is around 1200 $mAh \cdot g^{-1}$.

The preliminary fractional alloying of the high purity, nano-scaled silicon powder D with potassium has a positive effect on the performance of the active material. Also in this case we can proceed on the assumption, that the presence of the potassium implicates a decrease of the free enthalpy of the lithium/silicon alloy and the formation of a higher lithiated phase is consequently favored.

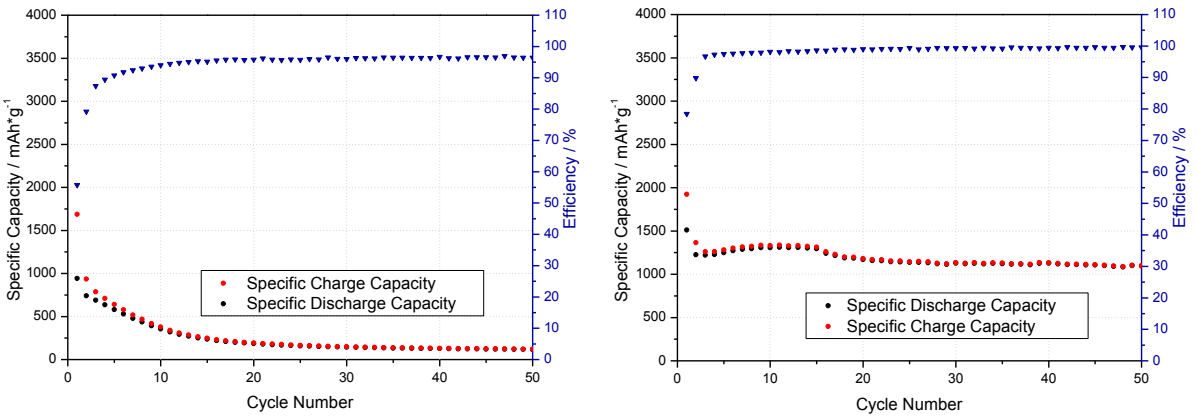

Figure 69: Constant current cycling of a pure silicon D electrode [m (active layer) = 0,233 mg] vs. Li/Li^+ (left) and a silicon D modified with K electrode [m (active layer) = 0,448 mg] vs. Li/Li^+ (right); EC/DEC (3:7, v:v), 1 M $LiPF_6$, 2 v% VC; test program 1

5.2.2.2 Analytical Results

Beyond that, scanning electron microscopy (SEM) measurements in combination with energy-dispersive X-ray spectroscopy (EDX) measurements were done (Figure 70).

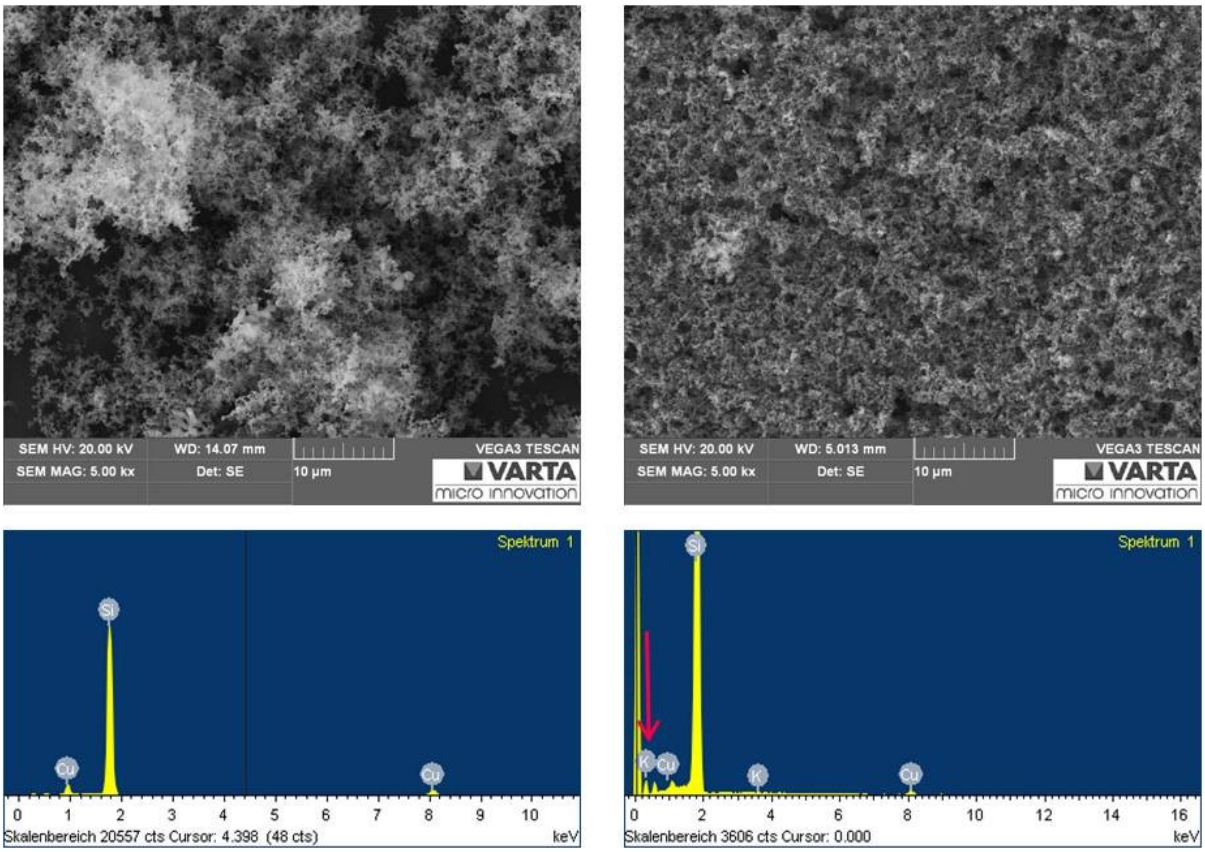

Figure 70: : Scanning electron microscopy images (top) and an energy-dispersive X-ray spectroscopy spectra (bottom) of an electrode made out of the pure nano-scaled silicon powder D (left) and an electrode made out of the with potassium preliminary fractional alloyed silicon powder D (evaporating time 24 h) (right)

Comparing the two scanning electron images in Figure 70 the silicon electrode made out of the with potassium preliminary fractional alloyed silicon D shows a more compact appearance. By the way of illustration, Figure 70 also show two energy-dispersive X-ray spectroscopy spectra of a silicon electrode made out of the pure silicon D and a silicon electrode made out of the with potassium modified silicon D. Altogether five spectra of the modified electrode were generated. The quantitative analysis in m% is shown in Table 20. In the case of the energy-dispersive X-ray measurements of a with K modified sample electrode the verification of potassium is proved difficult (Table 20, measuring point 1).

Table 19: Mass percent (m%) of potassium within the electrode made out of the pure nano-scaled silicon powder D generated from the energy-dispersive X-ray measurements shown in Figure 70

Measuring point	*K-K* [m%]	*Si-K* [m%]	*Cu-K* [m%]
Point 1	0.000	78.73	21.27
Point 2	0.000	77.78	22.22
Point 3	0.000	69.42	30.58
Point 4	0.000	67.90	32.10
Point 5	0.000	53.98	46.02

Table 20: Mass percent (m%) of potassium within the electrode made out of the with potassium preliminary fractional alloyed silicon powder D (evaporating time 24 h) generated from the energy-dispersive X-ray measurements shown in Figure 70

Measuring point	*K-K* [m%]	*Si-K* [m%]	*Cu-K* [m%]
Point 1	-0.050	96,85	3,200
Point 2	0,160	96,21	3,630
Point 3	0,010	95,26	4,730
Point 4	0,060	95,59	4,340
Point 5	0,110	96,55	3,340

5.2.3 Fractional Preliminary Alloying of Nano-Scaled Silicon with Sodium/Potassium Alloy

The fractional preliminary alloying of silicon D with sodium/potassium alloy is made by solid state diffusion at argon gas flow and a temperature of 900°C. We used 5 w% (calculated from the used overall solid mass of the nano-scaled silicon D powder) of the sodium/potassium alloy. The pure silicon was preliminary alloyed for 24 h. Subsequent a standard silicon electrode-slurry according to chapter 4.1.2.1 (page 48) was prepared.

5.2.3.1 Electrochemical Results

Figure 71 shows the cyclovoltammogramm of the unmodified silicon D electrode vs. Li/Li^+ in comparison to the with sodium/potassium alloy modified silicon D electrode vs. Li/Li^+. Figure 72 should illustrate in particular the differences in performance of the two different electrodes from cycle to cycle.

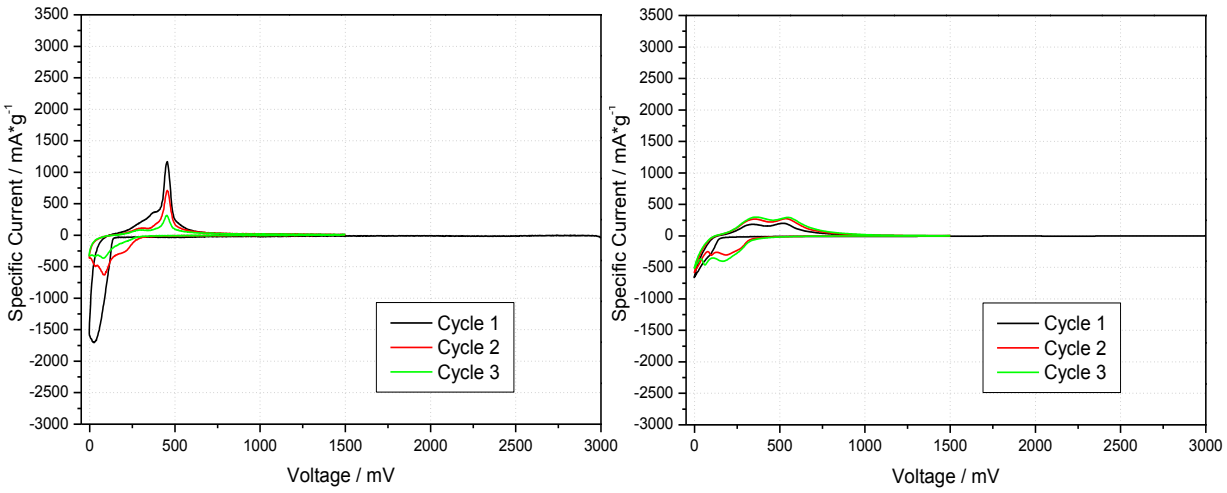

Figure 71: Cyclovoltammogramm of a pure silicon D electrode [m (active layer) = 0,369 mg] vs. Li/Li^+ (left) and a silicon electrode [m (active layer) = 1,873 mg] made out of the with sodium/potassium alloy modified silicon D vs. Li/Li^+ (right); EC/DEC (3:7, v:v), 1 M $LiPF_6$, 2 v% VC

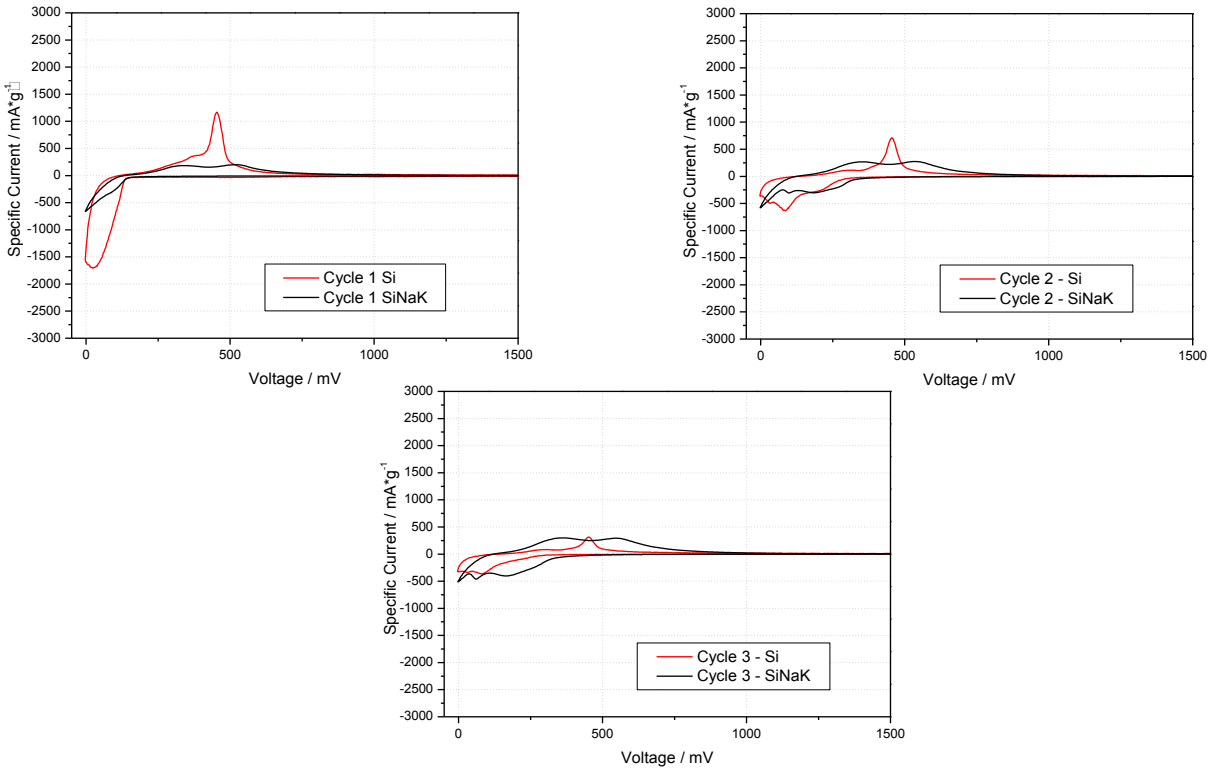

Figure 72: Particular cycles generated from the cyclovoltammogramms in Figure 71

Table 21 and Table 22 show the specific charge capacities, the specific discharge capacities and the efficiencies generated from the cyclovoltammogramms.

Table 21: Specific charge capacity, specific discharge capacity and efficiency generated from the cyclovoltammogramm of the pure silicon D electrode in Figure 71 (left)

Cycle	Specific Charge Capacity [mAh·g^{-1}]	Specific Discharge Capacity [mAh·g^{-1}]	Efficiency [%]
1	1116	658	59
2	536	417	78
3	328	261	80

Table 22: Specific charge capacity, specific discharge capacity and efficiency generated from the cyclovoltammogramm of the silicon D modified with Na/K alloy electrode in Figure 71 (right)

Cycle	Specific Charge Capacity [mAh·g^{-1}]	Specific Discharge Capacity [mAh·g^{-1}]	Efficiency [%]
1	929	748	81
2	1142	1088	95
3	1304	1252	96

The cyclovoltammogramms of the with sodium/potassium alloy preliminary fractional alloyed nano-scaled silicon D electrodes show worse reaction kinetics in comparison to the unmodified silicon D electrode. Figure 72 illustrates the particular cycles from the cyclovoltammogramm in Figure 71. We can observe that the electrode performance of the unmodified electrode gets worse from cycle to cycle, whereby the behavior of the modified electrode roughly remains constant. The generated specific charge and discharge capacities in Table 22 distinctly illustrate this statement. The with sodium/potassium alloy preliminary fractional alloyed silicon D electrode shows crucial better efficiencies than the electrode made out of the unmodified silicon D (Table 21 and Table 22).

Figure 73 shows the constant current cycling measurements of a silicon D electrode vs. Li/Li^+ and of a silicon D modified with sodium/potassium alloy electrode vs. Li/Li^+. The used test program is the test program 1 (chapter 4.2.2; page 51). We can observe an improvement in the cycling performance of the electrode by preliminary alloying of the nano-scaled silicon D with sodium/potassium alloy. The average discharge capacity is around 1000 $mAh \cdot g^{-1}$.

The preliminary fractional alloying of the high purity nano-scaled silicon D with the sodium/potassium alloy also implicates an improvement of the performance of the active material.

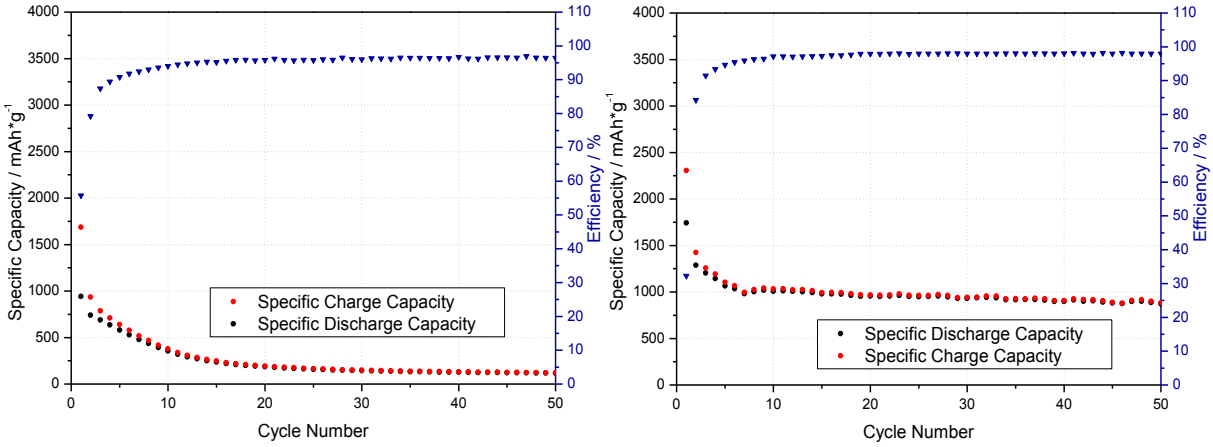

Figure 73: Constant current cycling of a pure silicon D electrode electrode [m (active layer) = 0,233 mg] vs. Li/Li^+ (left) and a silicon D modified with Na/K alloy electrode [m (active layer) = 1,663 mg] vs. Li/Li^+ (right); EC/DEC (3:7, v:v), 1 M $LiPF_6$, 2 v% VC; test program 1

5.2.3.2 Analytical Results

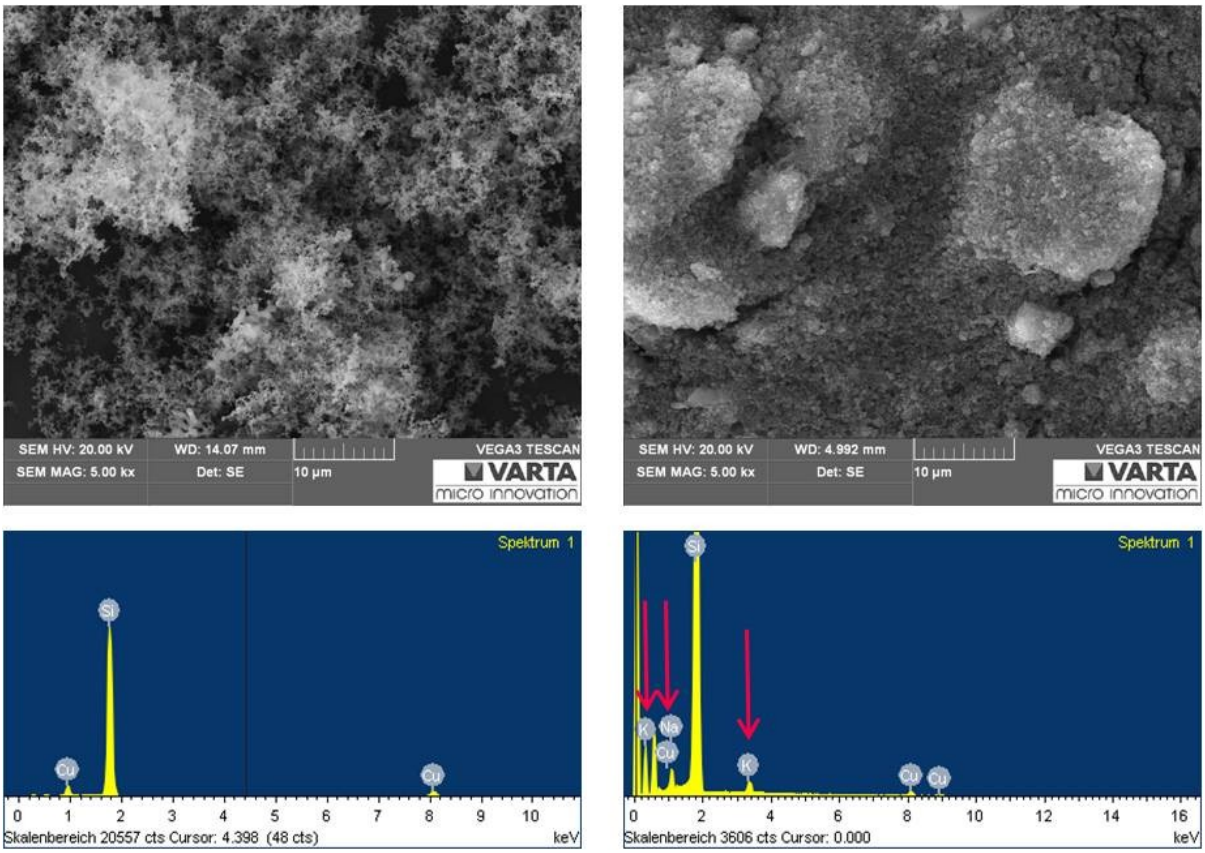

Figure 74: Scanning electron microscopy images (top) and an energy-dispersive X-ray spectroscopy spectra (bottom) of an electrode made out of the pure nano-scaled silicon powder D (left) and an electrode made out of the with sodium/potassium alloy preliminary fractional alloyed silicon powder D (evaporating time 24 h) (right)

Comparing the two scanning electron images in Figure 70 the silicon electrode made out of the with sodium/potassium alloy preliminary fractional alloyed silicon D shows a more compact appearance. Even the comparison with the SEM images of the with sodium and potassium modified silicon D electrodes shows that the with the sodium/potassium alloy modified silicon D electrode exhibits a more compact appearance, but the surface character seems to be not that plain. Altogether two spectra of the modified electrode were generated. The quantitative analysis in m% is shown in Table 24. In comparison to the previous discussed preliminary fractional alloyed samples in this case attention should be paid to the high amount of sodium and potassium within the sample electrode. This can be a reason for the latish worse cycling performance of the electrode.

Table 23: Mass percent (m%) of sodium and potassium within the electrode made out of the pure nano-scaled silicon powder D generated from the energy-dispersive X-ray measurements shown in Figure 74

Measuring point	*K-K* [m%]	*Na-K* [m%]	*Si-K* [m%]	*Cu-K* [m%]
Point 1	0.000	0.000	78.73	21.27
Point 2	0.000	0.000	77.78	22.22
Point 3	0.000	0.000	69.42	30.58
Point 4	0.000	0.000	67.90	32.10
Point 5	0.000	0.000	53.98	46.02

Table 24: Mass percent (m%) of sodium and potassium within the electrode made out of the with sodium/potassium alloy preliminary fractional alloyed silicon powder D (evaporating time 24 h) generated from the energy-dispersive X-ray measurements shown in Figure 74

Measuring point	*Na-K* [m%]	*K-K* [m%]	*Si-K* [m%]	*Cu-K* [m%]
Point 1	1.71	2.06	93.13	3.10
Point 2	1.98	2.50	93.28	2.24

5.2.4 Fractional Preliminary Alloying of Nano-Scaled Silicon with Calcium

The fractional preliminary alloying of silicon D with calcium is made by solid state diffusion at argon gas flow and a temperature of 950°C. We used 10 w% (calculated from the used overall solid mass of the nano-scaled silicon D powder) of calcium metal. The pure material was preliminary alloyed for 24 h. Subsequent a standard silicon electrode-slurry according to chapter 4.1.2.1 (page 48) was prepared.

5.2.4.1 Electrochemical Results

Figure 75 shows the cyclovoltammogramm of the unmodified silicon D electrode vs. Li/Li^+ in comparison to a with calcium modified silicon D electrode vs. Li/Li^+. Figure 76 should illustrate in particular the differences in performance of the two different electrodes from cycle to cycle.

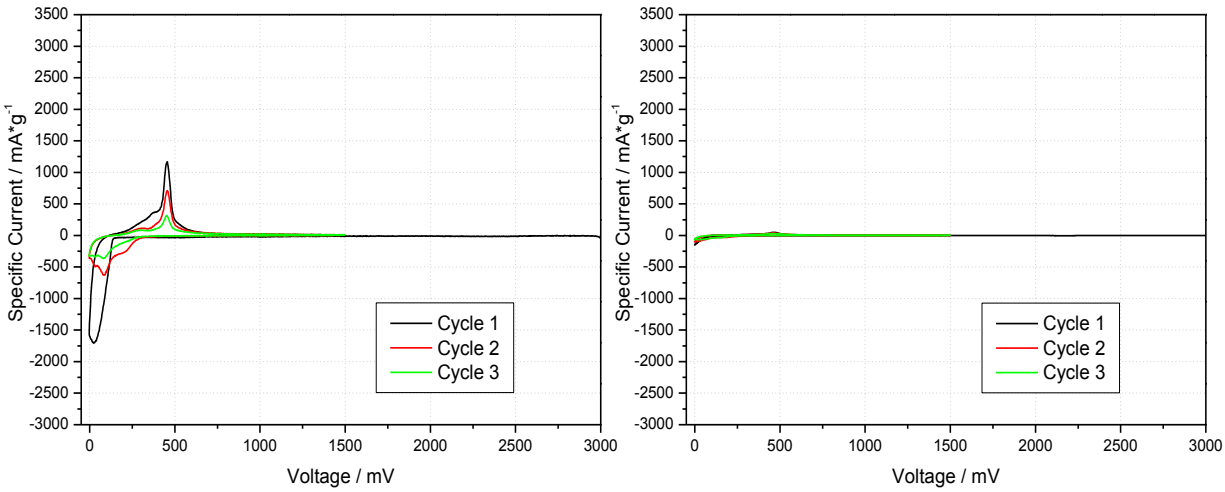

Figure 75: Cyclovoltammogramm of a pure silicon D electrode [m (active layer) = 0,369 mg] vs. Li/Li^+ (left) and a silicon electrode [m (active layer) = 3,699 mg] made out of the with calcium modified silicon D vs. Li/Li^+ (right); EC/DEC (3:7, v:v), 1 M $LiPF_6$, 2 v% VC

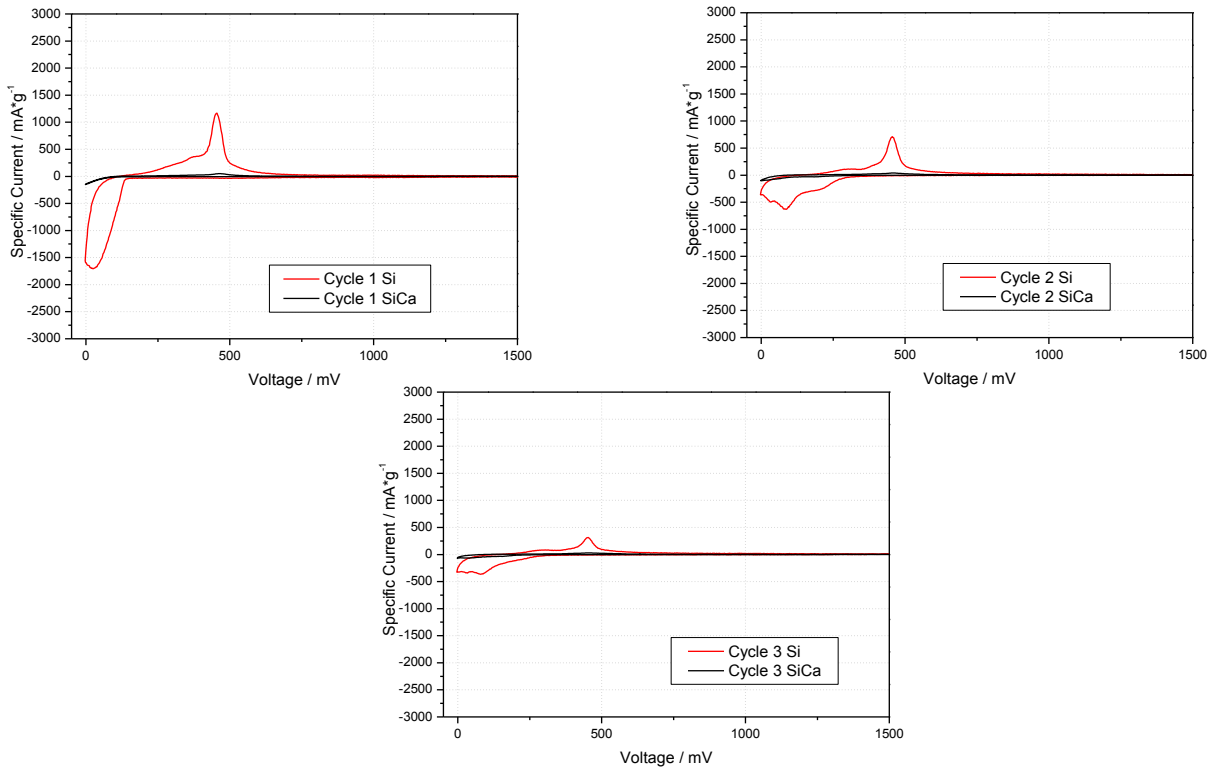

Figure 76: Particular cycles generated from the cyclovoltammogramms in Figure 75

Table 25 and Table 26 show the specific charge capacities, the specific discharge capacities and the efficiencies generated from the cyclovoltammogramms.

Table 25: Specific charge capacity, specific discharge capacity and efficiency generated from the cyclovoltammogramm of the pure silicon D electrode in Figure 75 (left)

Cycle	Specific Charge Capacity [mAh·g^{-1}]	Specific Discharge Capacity [mAh·g^{-1}]	Efficiency [%]
1	1116	658	59
2	536	417	78
3	328	261	80

Table 26: Specific charge capacity, specific discharge capacity and efficiency generated from the cyclovoltammogramm of the silicon D modified with Ca electrode in Figure 58 (right)

Cycle	Specific Charge Capacity [mAh·g^{-1}]	Specific Discharge Capacity [mAh·g^{-1}]	Efficiency [%]
1	196	105	54
2	157	112	71
3	119	96	81

Comparing the two cyclovoltammogramms in Figure 58 we can see, that the electrode made out of with calcium preliminary fractional alloyed silicon D doesn´t deliver the desired results. During the insertion of lithium as well as during the extraction of lithium we cannot observe appreciable electrochemical reactions, thus, the modified electrode doesn´t show an improvement in the electrochemical properties in comparison to the pure silicon electrode. This can be confirmed by the generated charge and discharge capacities, which are really low (Table 25 and Table 26).

Figure 77 shows the constant current cycling measurements of a silicon D electrode vs. Li/Li^+ and of a silicon D modified with calcium electrode vs. Li/Li^+. The used test program is the test program 1 (chapter 4.2.2; page 51). These measurements confirm the results gained from the cyclovoltammetry. We cannot observe an improvement in the cycling performance of the electrode by preliminary alloying of the nano-scaled silicon D with calcium. The average discharge capacity is 100 $mAh \cdot g^{-1}$.

The fractional preliminary alloying of the high purity nano-scaled silicon powder D with calcium doesn´t provide the desired results. In this case we can assume that the preliminary fractional alloying process by solid state diffusion doesn´t sufficiently occur and due to this fact no decrease in the free enthalpy proceeds.

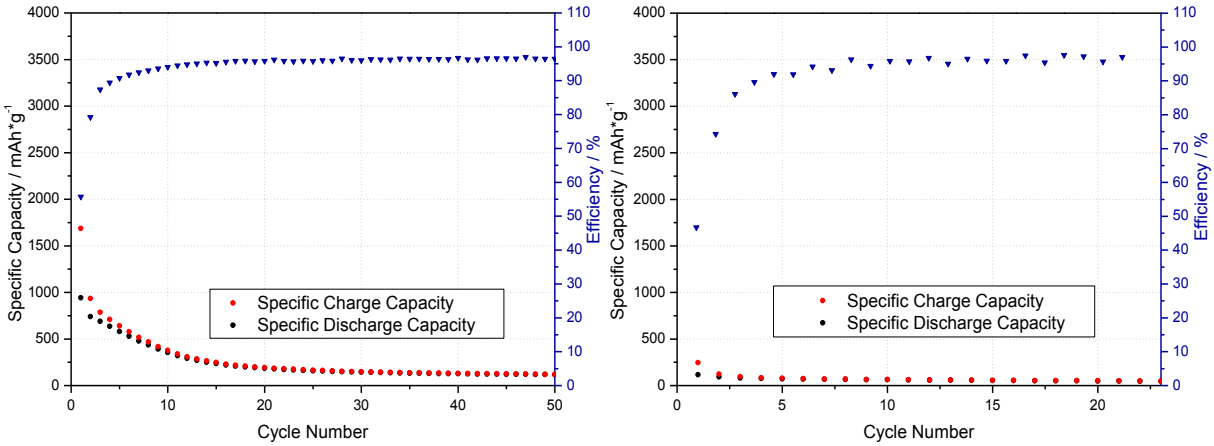

Figure 77: Constant current cycling of a pure silicon D electrode electrode [m (active layer) = 0,233 mg] vs. Li/Li^+ (left) and a silicon D modified with Ca electrode [m (active layer) = 4,044 mg]vs. Li/Li^+ (right); EC/DEC (3:7, v:v), 1 M $LiPF_6$, 2 v% VC; test program 1

5.2.4.2 Analytical Results

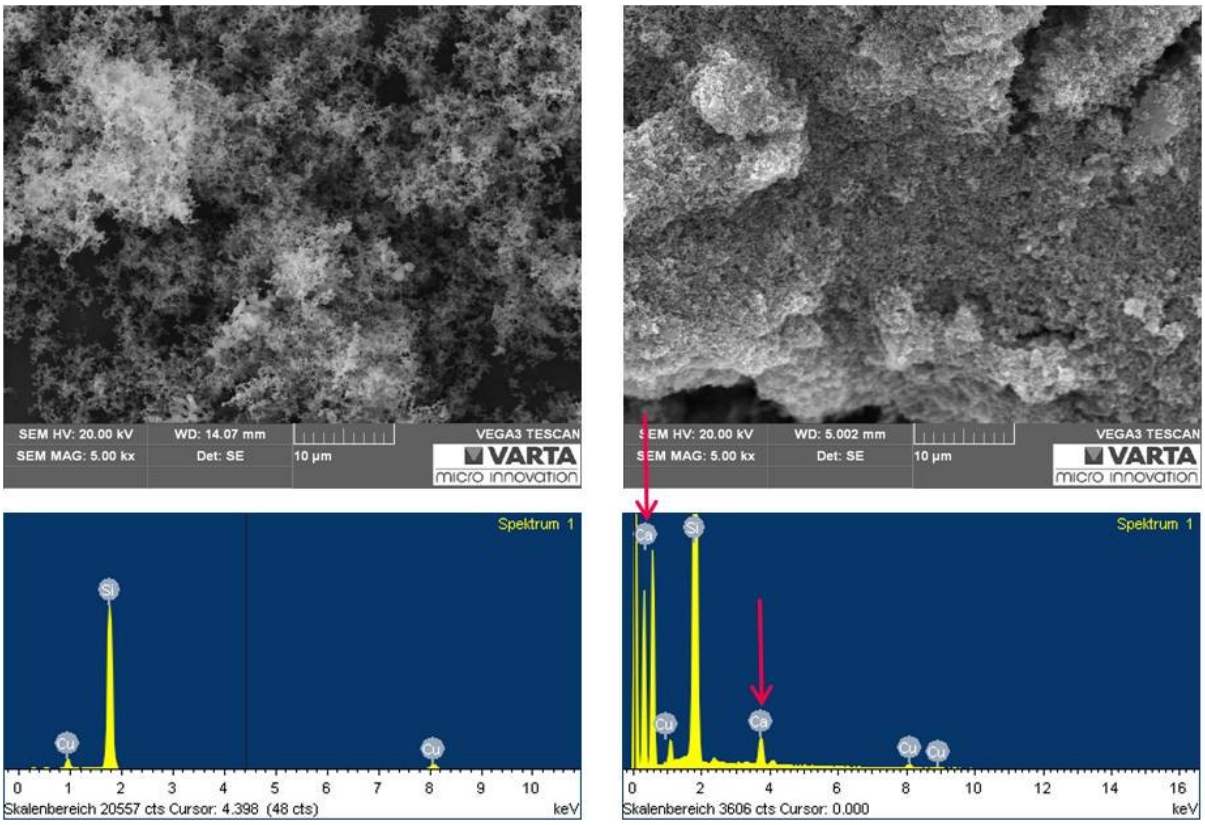

Figure 78: Scanning electron microscopy images (top) and an energy-dispersive X-ray spectroscopy spectra (bottom) of an electrode made out of the pure nano-scaled silicon powder D (left) and an electrode made out of the with calcium preliminary fractional alloyed silicon powder D (evaporating time 24 h) (right)

The comparison of the scanning electron microscopy images in Figure 78 shows in general a more compact appearance of the with calcium modified silicon D electrode. But partial there are seeming crater (Figure 78, bottom of the right SEM image) observable. The quantitative analysis in m% is shown in Table 28.

Table 27: Mass percent (m%) of calcium within the electrode made out of the pure nano-scaled silicon powder D generated from the energy-dispersive X-ray measurements shown in Figure 78

Measuring point	*Ca-K* [m%]	*Si-K* [m%]	*Cu-K* [m%]
Point 1	0.000	78.73	21.27
Point 2	0.000	77.78	22.22
Point 3	0.000	69.42	30.58
Point 4	0.000	67.90	32.10
Point 5	0.000	53.98	46.02

Table 28: Mass percent (m%) of calcium within the electrode made out of the with calcium preliminary fractional alloyed silicon powder D (evaporating time 24 h) generated from the energy-dispersive X-ray measurements shown in Figure 78

Measuring point	*Ca-K* [m%]	*Si-K* [m%]	*Cu-K* [m%]
Point 1	6.760	89.17	4.070
Point 2	7.140	89.71	3.150

5.2.5 Fractional Preliminary Alloying of Nano-Scaled Silicon with Magnesium

The fractional preliminary alloying of silicon D with magnesium is made by solid state diffusion at argon gas flow and a temperature of 600°C. We used 10 w% (calculated from the used overall mass of the nano-scaled silicon D powder) of magnesium. The pure material was preliminary alloyed for 24 h. Subsequent a standard silicon electrode-slurry according to chapter 4.1.2.1 (page 48) was prepared.

5.2.5.1 Electrochemical Results

Figure 79 shows the cyclovoltammogramm of the unmodified silicon D electrode vs. Li/Li^+ in comparison to a with magnesium modified silicon D electrode vs. Li/Li^+. Figure 80 should illustrate in particular the differences in performance of the two different electrodes from cycle to cycle.

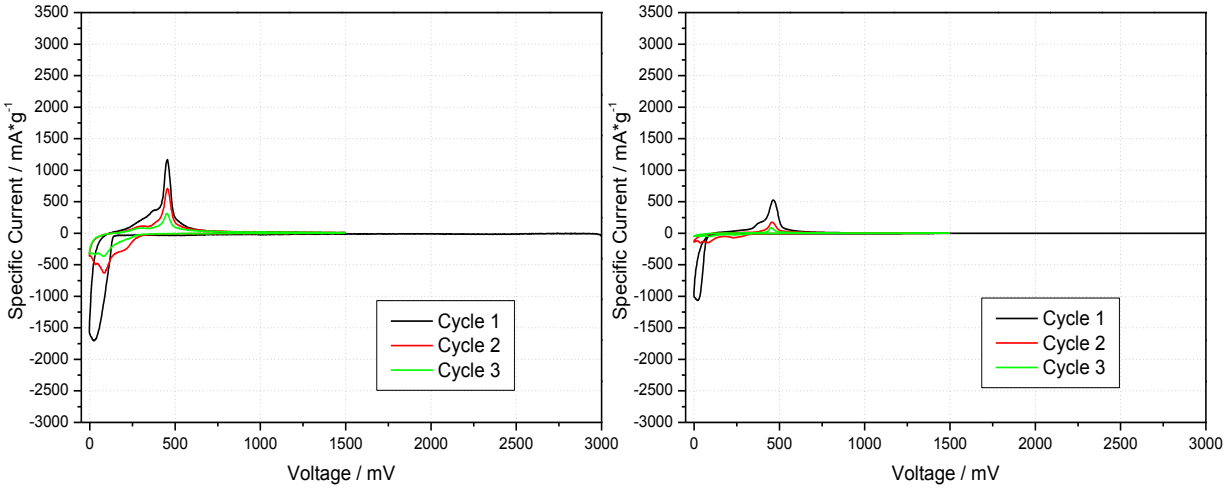

Figure 79: Cyclovoltammogramm of a pure silicon D electrode [m (active layer) = 0,369 mg] vs. Li/Li^+ (left) and a silicon electrode [m (active layer) = 0,734 mg] made out of the with magnesium modified silicon D vs. Li/Li^+ (right); EC/DEC (3:7, v:v), 1 M $LiPF_6$, 2 v% VC

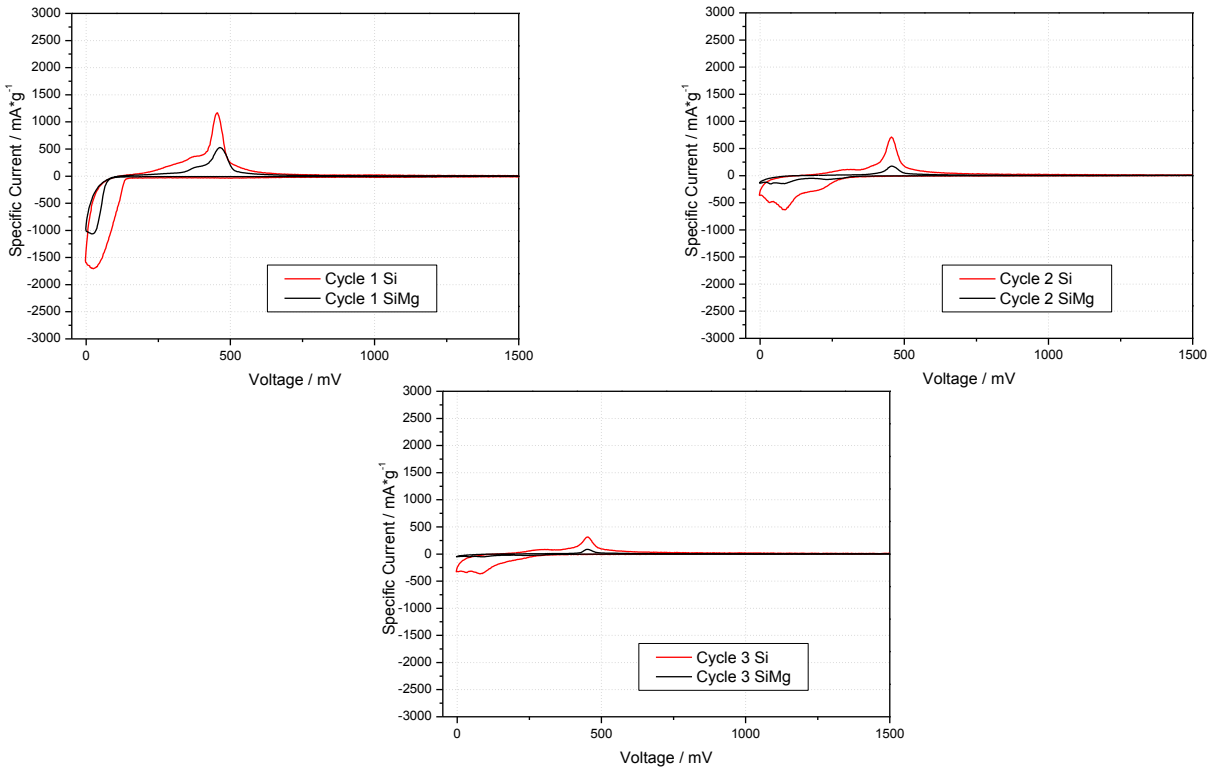

Figure 80: Particular cycles generated from the cyclovoltammogramms in Figure 79

Table 29 and Table 30 show the specific charge capacities, the specific discharge capacities and the efficiencies generated from the cyclovoltammogramms.

Table 29: Specific charge capacity, specific discharge capacity and efficiency generated from the cyclovoltammogramm of the pure silicon D electrode in Figure 79 (left)

Cycle	Specific Charge Capacity [mAh·g^{-1}]	Specific Discharge Capacity [mAh·g^{-1}]	Efficiency [%]
1	1116	658	59
2	536	417	78
3	328	261	80

Table 30: Specific charge capacity, specific discharge capacity and efficiency generated from the cyclovoltammogramm of the silicon D modified with Mg electrode in Figure 79 (right)

Cycle	Specific Charge Capacity [mAh·g^{-1}]	Specific Discharge Capacity [mAh·g^{-1}]	Efficiency [%]
1	914	609	67
2	315	203	64
3	121	99	82

Comparing the two cyclovoltammogramms in Figure 79 we cannot observe an improvement in the electrochemical properties of the modified electrode. Figure 80 illustrates that the pure silicon electrode as well as the modified silicon electrode gets worse from cycle to cycle. This statement is better pointed by the generated charge and discharge capacities shown in Table 29 and Table 30. The capacities of the modified silicon electrode are worse than those of the pure silicon electrode.

Figure 81 shows the constant current cycling measurements of a pure silicon D electrode vs. Li/Li$^+$ and of a with manganese modified silicon D electrode vs. Li/Li$^+$. The used test program is the test program 1 (chapter 4.2.2; page 51). These measurements confirm the results gained from the cyclovoltammetry. We can observe degradation in the cycling performance of the electrode by preliminary alloying of the nano-scaled silicon D with manganese. The average discharge capacity is around 50 mAh·g^{-1}.

Here too, the fractional preliminary alloying of the high purity nano-scaled silicon powder D with magnesium doesn´t provide the desired results. We can also assume that the preliminary fractional alloying process by solid state diffusion doesn´t sufficiently occur and due to this fact no decrease in the free enthalpy proceeds.

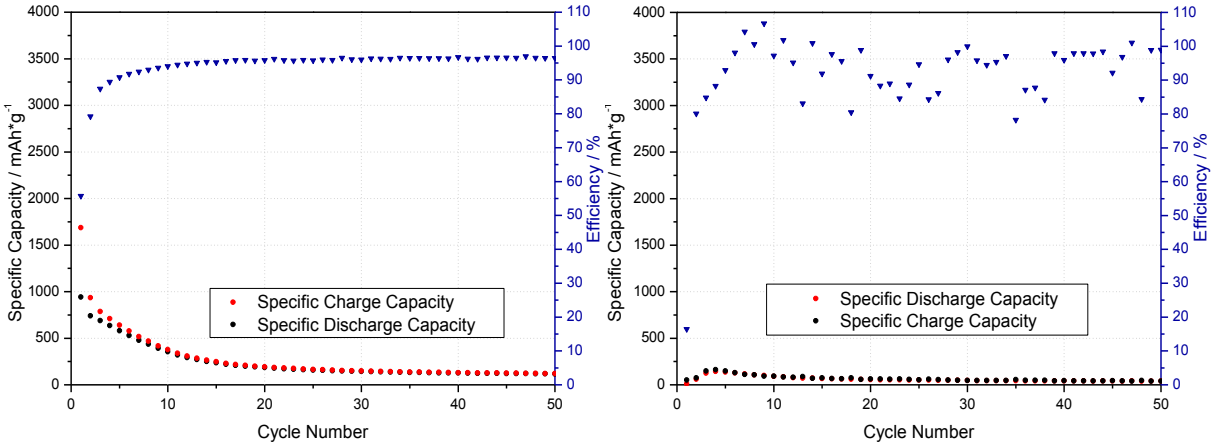

Figure 81: Constant current cycling of a pure silicon D electrode electrode [m (active layer) = 0,233 mg] vs. Li/Li$^+$ (left) and a silicon D modified with Mg electrode [m (active layer) = 0,574 mg] vs. Li/Li$^+$ (right); EC/DEC (3:7, v:v), 1 M $LiPF_6$, 2 v% VC; test program 1

5.2.5.2 Analytical Results

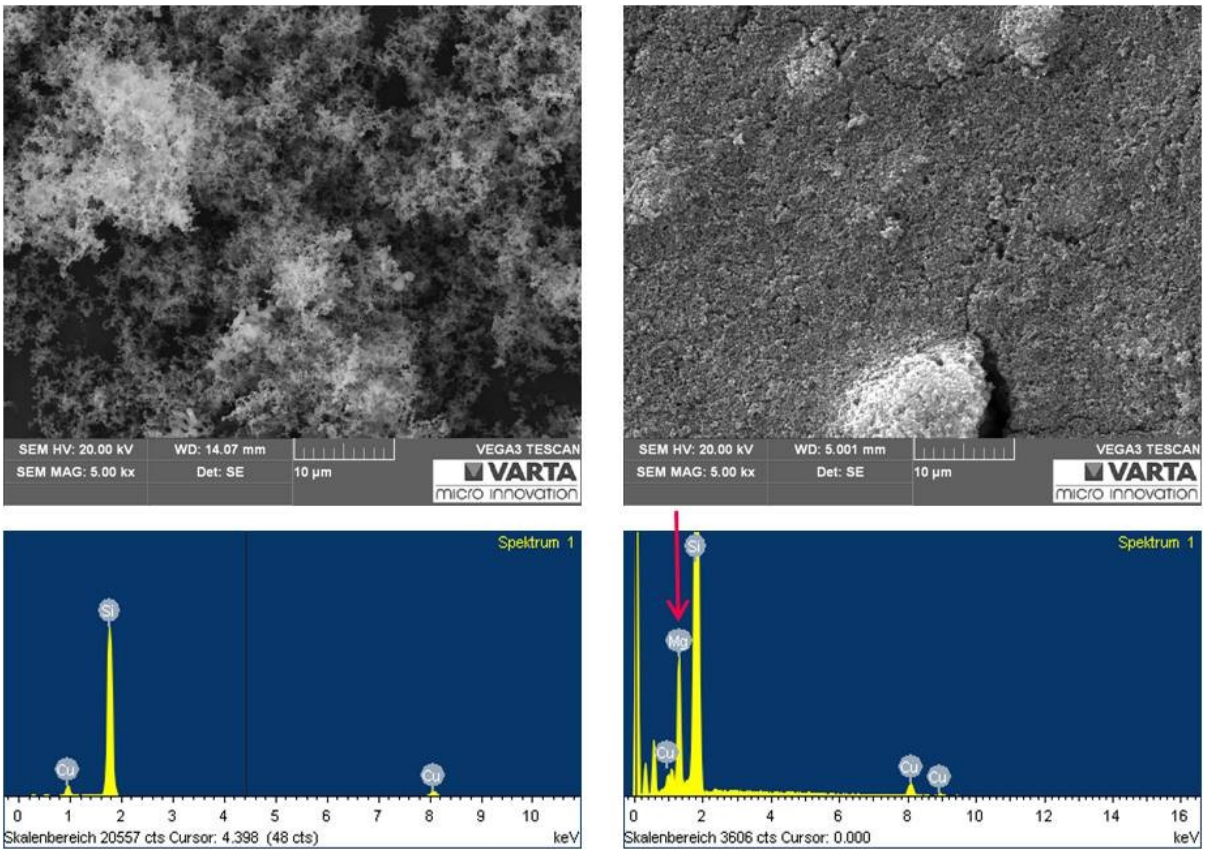

Figure 82: Scanning electron microscopy images (top) and an energy-dispersive X-ray spectroscopy spectra (bottom) of an electrode made out of the pure nano-scaled silicon powder D (left) and an electrode made out of the with magnesium preliminary fractional alloyed silicon powder D (evaporating time 24 h) (right)

The SEM image of the silicon electrode made out of the with magnesium preliminary fractional alloyed silicon D powder shows a real compact appearance with some irregularities like small fissures and ridges. The quantitative analysis in m% is shown in Table 32.

Table 31: Mass percent (m%) of magnesium within the electrode made out of the pure nano-scaled silicon powder D generated from the energy-dispersive X-ray measurements shown in Figure 82

Measuring point	*Mg-K* [m%]	*Si-K* [m%]	*Cu-K* [m%]
Point 1	0.000	78.73	21.27
Point 2	0.000	77.78	22.22
Point 3	0.000	69.42	30.58
Point 4	0.000	67.90	32.10
Point 5	0.000	53.98	46.02

Table 32: Mass percent (m%) of magnesium within the electrode made out of the with magnesium preliminary fractional alloyed silicon powder D (evaporating time 24 h) generated from the energy-dispersive X-ray measurements shown in Figure 82

Measuring point	*Mg-K* [m%]	*Si-K* [m%]	*Cu-K* [m%]
Point 1	7.160	86.32	6.520
Point 2	7.430	86.12	6.450

6 Experimental Part 2: Alternative Aqueous Preparation Technique of Silicon/Graphite Composite Anodes for High Energy Lithium-Ion Batteries

6.1 Background and Motivation

In general, an electrode for lithium-ion batteries consists of electrochemical active and inactive components (chapter 0, page 46). On consideration of the negative electrode (anode) the inactive components are the binding agent (PVdF or CMC), the conductive agent (carbon black) and the current collector (copper foil). The binder sticks the active material particles together and consequently ensures the contact of them with the current collector foils (chapter 3.2.4, page 37). The conductive agent caters for a better electronic contact between the active material particles and the current collector ensures an electronic contact to the whole mixture of active and inactive materials within the electrode-paste.

The common active materials for anodes are carbonaceous materials (chapter 3.2.2.1, page 24), whereby, as already mentioned in chapter 1 (page 1), a substitution of them by intermetallic anode materials, especially silicon, is desirable. But unfortunately, as mentioned previously in chapter 1 (page 1) and chapter 3.2.2.2 (page 29), the lithiation and delithiation of silicon and other intermetallic anode materials, like tin and antimony, comes along with enormous volume changes, which induce a disintegration of the active material particles. Subsequent a loss of contact to the ionic and electric conducting electrode environment occurs and as a result a significant capacity fading during the cycling of the electrode is observable.

The common binders for negative carbonaceous electrodes are fluoridated polymers and copolymers, like for example polyvinylidenfluoride and polyvinylidenfluoride-hexafluorpropylene. These polymer binder systems are from the economic and ecological point of view problematic due to the reason that it´s necessary to process them in unfavorable organic solvents, like N-methylpyrollidin-2-on or acetone. In this connection the use of sodium-carboxymethylcellulose and other cellulose based binder systems, which can be processed in water based electrode-pastes, constitutes a desirable advancement in the scope of environment-friendly electrode processing (chapter 3.2.4, page 37). Beyond that an improvement in the cycling performance of, for example, silicon and silicon/carbon composite electrodes is observable.

The main purpose of a sodium-carboxymethylcellulose binder in these electrodes is to stabilize the structure of the electrode. In this connection the mechanical behavior of the binder is of the first magnitude. Thus, the improvement in the cycling performance of electrodes with sodium-carboxymethylcellulose in contrast to for example polyvinylidenfluoride as binder is to seek in the more compact behavior of the cellulose based binder material. Cellulose-derivates constitute compared to polyvinylidenfluoride thermosetting properties. Although these properties are favorable for the cycling stability of silicon and silicon/carbon composite electrodes, they impede the electrode processing. An exfoliation of the brittle electrode-paste from the current collector foil during the drying process and a worse consistency against mechanical load during the manufacturing of the electrodes, like rolling and calendering, are two possible consequences of the thermosetting properties of cellulose based binder systems (Figure 83).

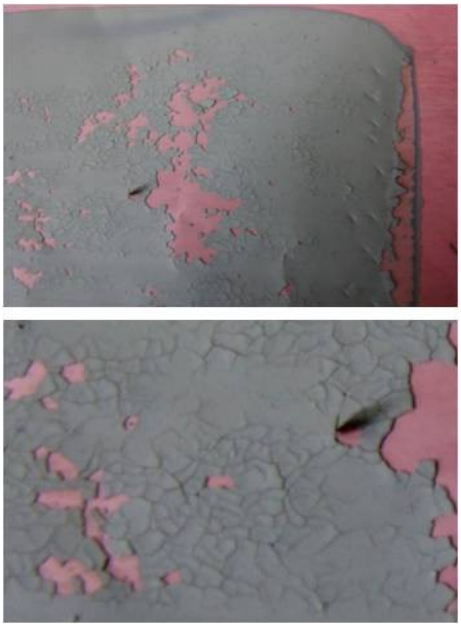

Figure 83: Picture of a silicon electrode-paste without a plasticizer coated on a copper foil

The problem of exfoliation certainly increases with the thickness of the electrode active layer on the current collector foil. That´s the reason, why the processing of water based intermetallic anodes with cellulose based binder isn´t commercially possible without additional efforts.

To overcome this problem of problematically processing of water based electrodes, especially with sodium-carboxymethylcellulose as binder, we tried to improve the not desirable behavior during the electrode preparation process by the addition of an at least partially water soluble plasticizer to the electrode paste (Figure 84).

Figure 84: Picture of a silicon electrode-paste with a plasticizer coated on a copper foil

In general a plasticizer has to accomplish the task of making a brittle material tender, resilient, flexible or ductile for his further processing. The common as plasticizer used organic materials are esters, like phthalates and adipates. More than 300 different types of plasticizers are known and around 50-100 of them are commercially used. Phthalates are the best known plasticizers[103]. The field of main application of plasticizers is the plastics industry, but a great quantity can also be found in varnishes, wall paints and glues. Furthermore plasticizers are also used from the textile industry and the cosmetics industry. Around 93 % of all plasticizers, which are produced in Europe, are used in applications including PVC (Figure 85)[104].

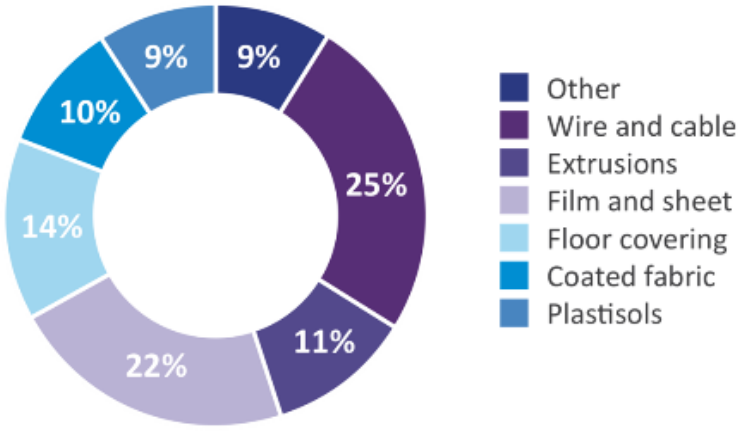

Figure 85: Percental distribution of plasticizers in the different areas of PVC applications[104]

Recently nonvolatile phthalate ester, like for example di(2-ethylhexyl)phthalate (DEHP), hit negative headlines because of their noxious effects as a component in toys made out of polyvinylchloride (PVC). Thus, low phthalates (3-6 carbon atoms), like di-n-butyl phthalate (DBP) and di(2-ethylhexyl)phthalate are more and more substituted by high phthalates (7-13 carbon atoms), like diisononyl phthalate (DINP) and diisodecyl phthalate (DIDP) (Figure 86)[104]. Further common plasticizers are esters of fatty acids, hydroxyl carboxylic acid esters and phosphoric acid esters. But also natural materials like camphor, castor oil and citrates have an emollient effect[105].

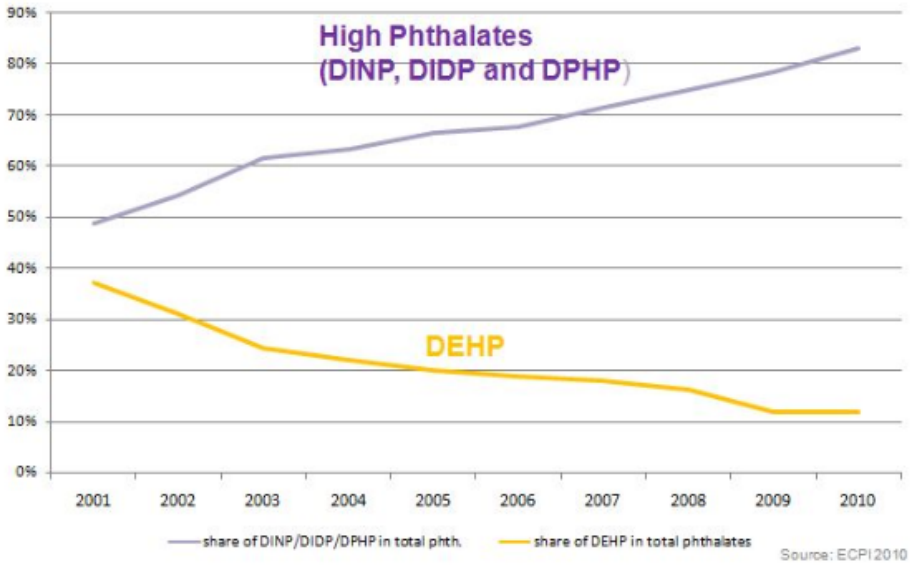

Figure 86: Percentage of phthalates sales in Europe compared to other plasticizers[104]

An atoxic alternative to the common phthalate based plasticizers are for example citric acid esters. Within this work we investigated two partially water soluble, atoxic plasticizers, glyceryltriacetate and triethylcitrate (Figure 87, Table 33). Glyceryltriacetate (E1505) and triethylcitrate (E1518) are both officially sanctioned in the European Union as food additives for aromas and much more[106].

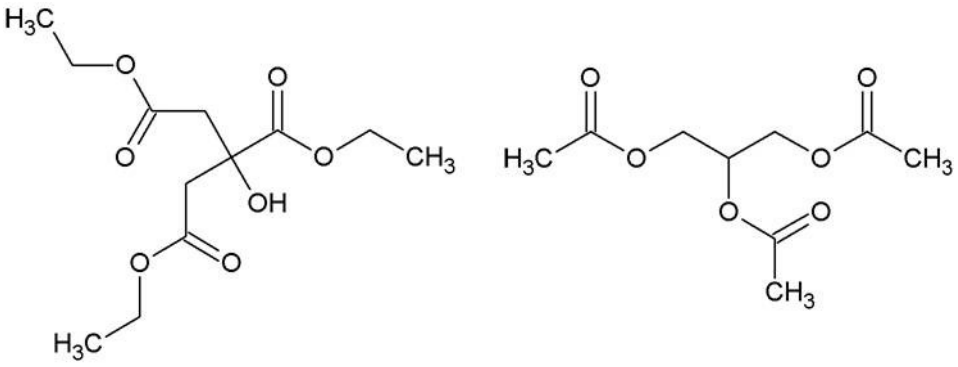

Figure 87: Structural formula of glyceryltriacetate (left) and triethylcitrate (right)

Table 33: Water solubility and boiling points of the two investigated partially water soluble plasticizers triethylcitrate and glyceryltriacetate[107]

	Triethylcitrate	Glyceryltriacetate
Solubility in distilled water [g·l^{-1}]	65	64
Boiling point [°C]	294 [127 (0.001 bar)]	258-260

As already mentioned, triethylcitrate and glyceryltriacetate are only partial soluble in water but they exhibit a good solubility in ethanol. Hence, to enlarge the possible amount of the partial water soluble plasticizers within the electrode-paste the influence of the partial substitution of distilled water with ethanol abs. within the electrodes preparation process was investigated.

Beyond that, two water soluble, atoxic plasticizers, 1,2-propanediol and glycerin, were investigated (Figure 88, Table 34). 1,2-Propanediol and glycerin are already used for example in several commercial cosmetic products.

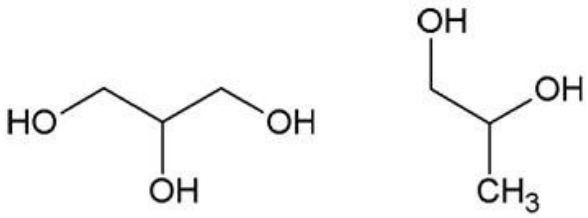

Figure 88: Structural formula of glycerin (left) and 1,2-propanediol (right)

Table 34: Boiling points of the two investigated water soluble plasticizers 1,2-propanediol and glycerin[107]

	1,2-Propanediol	Glycerin
Boiling point [°C]	186-188	290 [182 (0.027 bar)]

Every of the four above-mentioned plasticizers should be removed completely or at least partially during the first and second drying step of the electrodes at fine vacuum and a temperature of around 120°C (chapter 0, page 46). Hence, they shouldn´t influence the electrochemical performance of the electrodes.

6.2 Experimental Results

6.2.1 Partially Water Soluble Plasticizers – Glyceryltriacetate and Triethylcitrate

In this connection a standard silicon/graphite composite electrode-paste according to chapter 4.1.2.2 (page 49) was prepared. 10 w% (calculated from the used overall mass of the electrode-paste) of glyceryltriacetate or triethylcitrate were added after point 1 of the dispersing sequence (dissolving the Na-CMC binder in distilled water; page 49).

Figure 89 shows a cyclovoltammogramm of an uncalendered silicon/graphite composite electrode as contrasted with an uncalendered silicon/graphite composite electrode with the addition of 10 w% glyceryltriacetate or triethylcitrate.

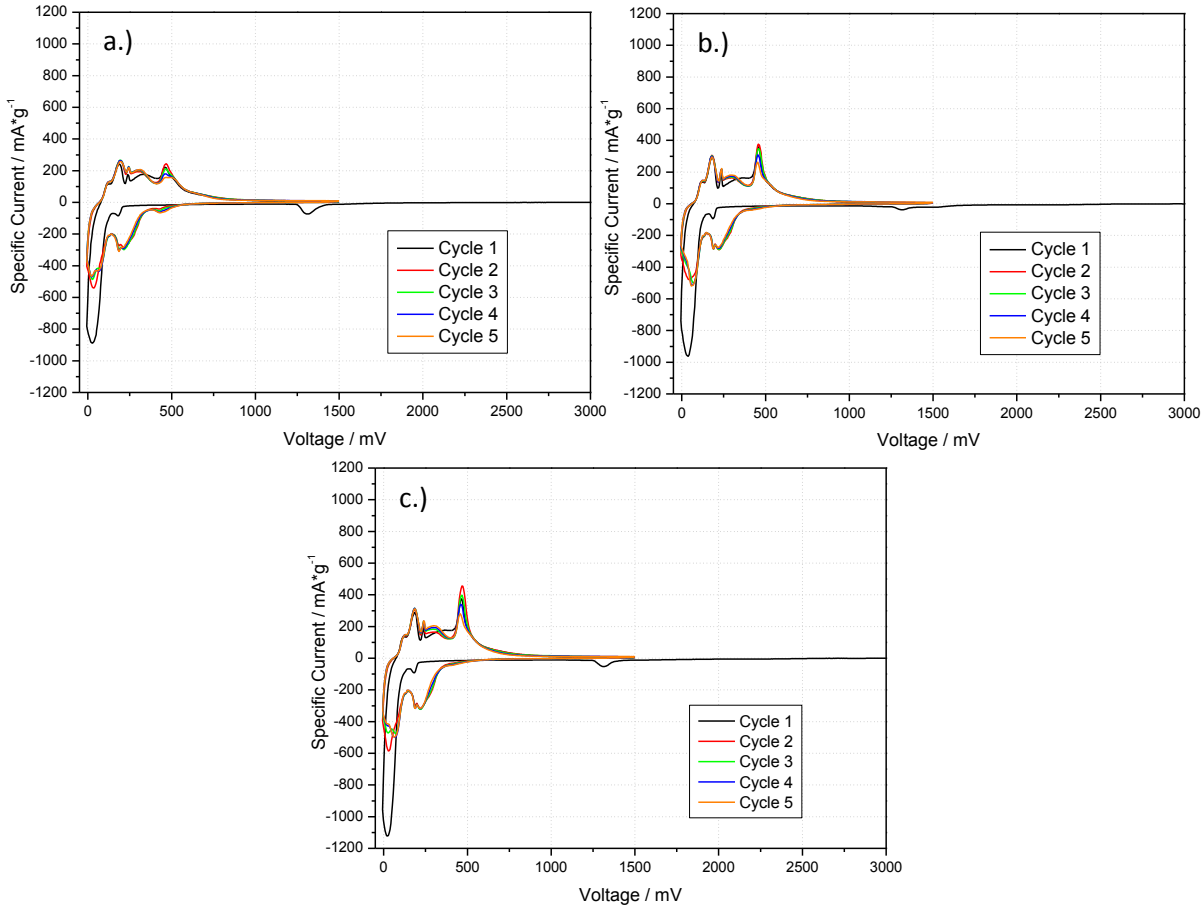

Figure 89: Cyclovoltammogramm of a.) an uncalendered silicon/graphite composite electrode [m (active layer) = 0,752 mg] vs. Li/Li^+; b.) an uncalendered silicon/graphite composite electrode [m (active layer) = 0,577 mg] with 10 w% glyceryltriacetate vs. Li/Li^+; c.) an uncalendered silicon/graphite composite electrode [m (active layer) = 0,572 mg] with 10 w% triethylcitrate vs. Li/Li^+; EC/DEC (3:7, v:v), 1 M $LiPF_6$, 2 v% VC

Table 35, Table 36 and Table 37 illustrate the specific charge and discharge capacities and the efficiencies generated from the cyclovoltammogramms in Figure 89.

Table 35: Specific charge capacity, specific discharge capacity and efficiency generated from the cyclovoltammogramm of the uncalendered silicon/graphite composite electrode in Figure 89 a.)

Cycle	Specific Charge Capacity [mAh·g^{-1}]	Specific Discharge Capacity [mAh·g^{-1}]	Efficiency [%]
1	1195	860	72
2	1064	947	89
3	1048	943	90
4	1044	936	90
5	1029	915	89

Table 36: Specific charge capacity, specific discharge capacity and efficiency generated from the cyclovoltammogramm of the uncalendered silicon/graphite composite electrode with 10w% glyceryltriacetate in Figure 89 b.)

Cycle	Specific Charge Capacity [mAh·g^{-1}]	Specific Discharge Capacity [mAh·g^{-1}]	Efficiency [%]
1	1272	909	71
2	1027	961	94
3	999	936	94
4	991	926	93
5	977	899	92

Table 37: Specific charge capacity, specific discharge capacity and efficiency generated from the cyclovoltammogramm of the uncalendered silicon/graphite composite electrode with 10w% triethylcitrate in Figure 89 c.)

Cycle	Specific Charge Capacity [mAh·g^{-1}]	Specific Discharge Capacity [mAh·g^{-1}]	Efficiency [%]
1	1431	1082	76
2	1114	1027	92
3	1091	1016	93
4	1074	993	92
5	1063	976	92

On consideration of the cyclovoltammogramms in Figure 89 there are no obvious parasitic reactions caused by the add-on of the plasticizer observable. The specific charge and discharge capacities and the efficiencies generated from the cyclovoltammogramms are nearly coincident. Thus, it can be determined that the addition of the plasticizer glyceryltriacetate or triethylcitrate during the electrode preparation process has no negative influence on the performance of the silicon/graphite composite electrode.

Figure 90 shows the constant current cycling measurements of the uncalendered silicon/graphite composite electrodes without and with the addition of 10 w% glyceryltriacetate or triethylcitrate. These measurements almost confirm the results gained from the cycolvoltammetric measurements. There is only a slight capacity fading of the uncalendered and with 10 w% of the plasticizer glyceryltriacetate or triethylcitrate manufactured composite electrode over 50 cycles observable. This slight capacity fading can be constituted by a modification of the porosity of the electrode. An increase in the porosity of the electrode would determine an increase in the active electrode surface, which leads to an obvious, continuous electrolyte decomposition and, hence, to a modification in the performance of the electrode.

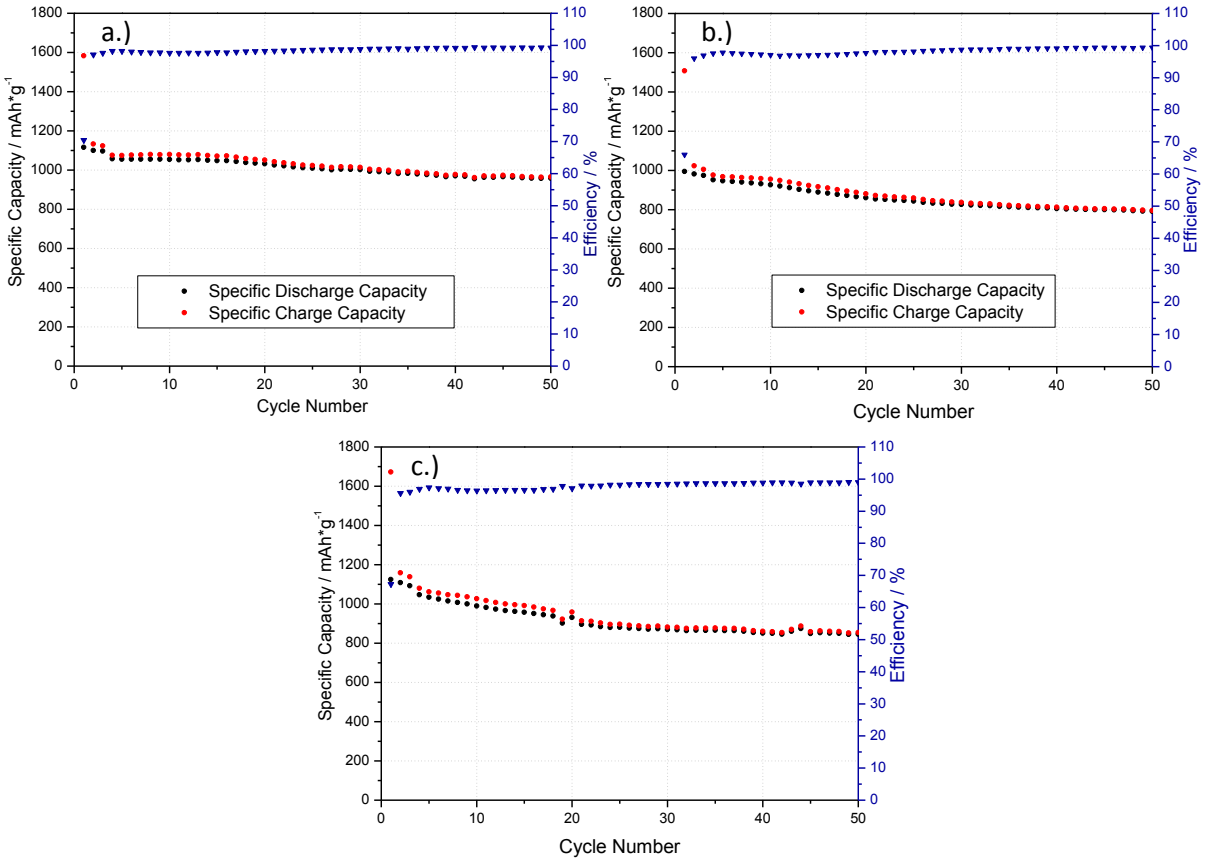

Figure 90: Constant current cycling of a.) an uncalendered silicon/graphite composite electrode [m (active layer) = 0,452 mg] vs. Li/Li$^+$; b.) an uncalendered silicon/graphite composite electrode [m (active layer) = 0,482 mg] with 10 w% glyceryltriacetate vs. Li/Li$^+$; c.) an uncalendered silicon/graphite composite electrode [m (active layer) = 0,472 mg] with 10 w% triethylcitrate vs. Li/Li$^+$; EC/DEC (3:7, v:v), 1 M $LiPF_6$, 2 v% VC; test program 2

In contrast to the uncalendered composite electrodes also calendered (calendering rate: 30 %) silicon/graphite composite electrodes without a plasticizer as well as with 10 w% glyceryltriacetate were investigated. Figure 91 shows the measured cyclovoltammogramms of the calendered silicon/graphite electrodes without and with the addition of a plasticizer.

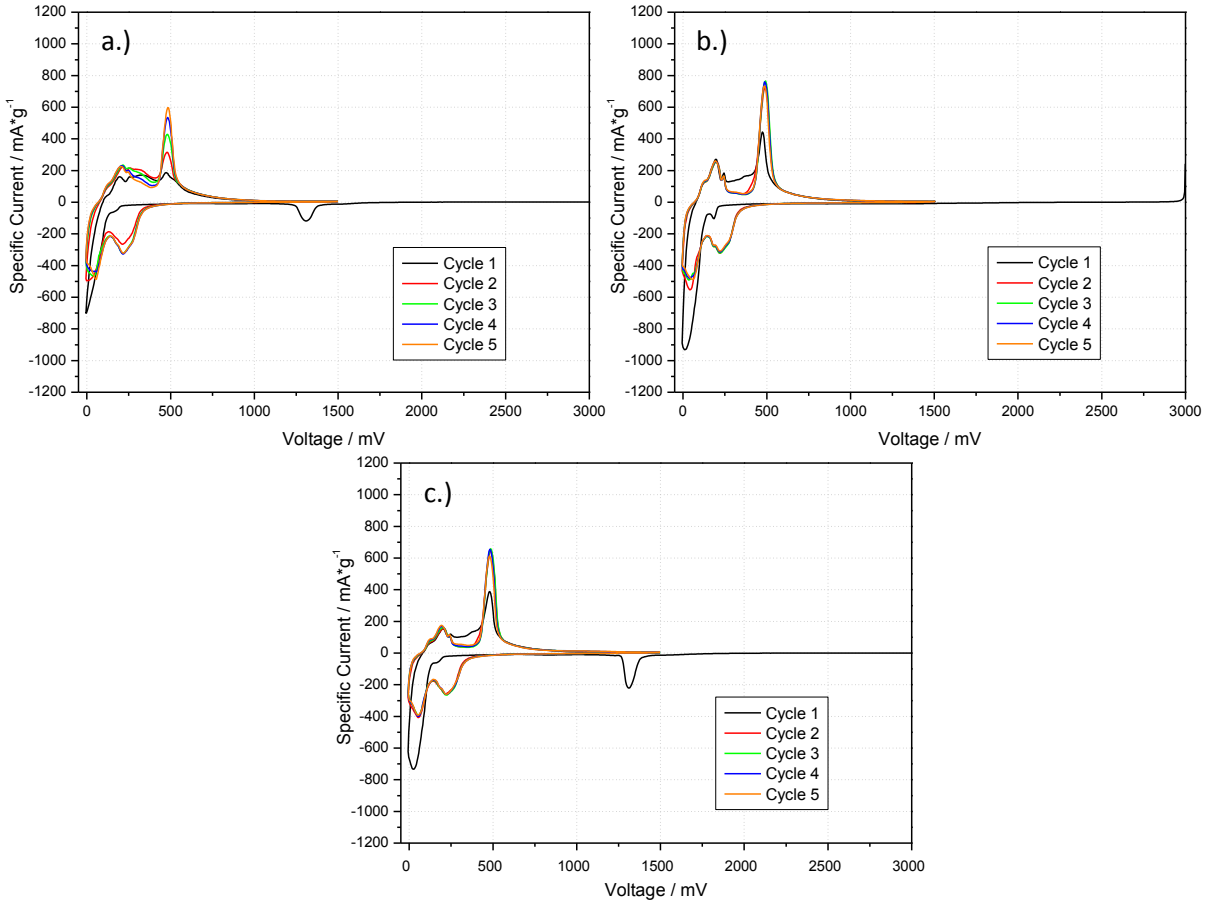

Figure 91: Cyclovoltammogramm of a.) a 30 % calendered silicon/graphite composite electrode [m (active layer) = 0,642 mg] vs. Li/Li$^+$; b.) a 30 % calendered silicon/graphite composite electrode [m (active layer) = 0,537 mg] with 10 w% glyceryltriacetate vs. Li/Li$^+$ (right); c.) a 30 % calendered silicon/graphite composite electrode [m (active layer) = 0,482 mg] with 10 w% triethylcitrate vs. Li/Li$^+$; EC/DEC (3:7, v:v), 1 M $LiPF_6$, 2 v% VC

Table 38, Table 39 and Table 40 illustrate the specific charge and discharge capacities and the efficiencies generated from the cyclovoltammogramms in Figure 91 .

Table 38: Specific charge capacity, specific discharge capacity and efficiency generated from the cyclovoltammogramm of the calendered silicon/graphite composite electrode in Figure 91 a.)

Cycle	Specific Charge Capacity [mAh·g^{-1}]	Specific Discharge Capacity [mAh·g^{-1}]	Efficiency [%]
1	1012	760	75
2	987	978	99
3	1022	1018	100
4	1031	1025	99
5	1032	1027	99

Table 39: Specific charge capacity, specific discharge capacity and efficiency generated from the cyclovoltammogramm of the calendered silicon/graphite composite electrode with 10w% glyceryltriacetate in Figure 91 b.)

Cycle	Specific Charge Capacity [mAh·g^{-1}]	Specific Discharge Capacity [mAh·g^{-1}]	Efficiency [%]
1	1164	968	83
2	1109	1062	96
3	1084	1053	97
4	1073	1042	97
5	1065	1037	97

Table 40: Specific charge capacity, specific discharge capacity and efficiency generated from the cyclovoltammogramm of the calendered silicon/graphite composite electrode with 10w% triethylcitrate in Figure 91 c.)

Cycle	Specific Charge Capacity [mAh·g^{-1}]	Specific Discharge Capacity [mAh·g^{-1}]	Efficiency [%]
1	1122	758	68
2	872	835	96
3	861	832	97
4	856	829	97
5	853	843	99

Comparing the three cyclovoltammogramms in Figure 91 no parasitic and inadvertent reactions are observable. By comparison of the cyclovoltammogramms of the uncalendered electrodes (Figure 89) with the cyclovoltammogramms of the calendered electrodes (Figure 91) in the case of the calendered electrodes sharper, higher current peaks are distinguishable. This is indicative for better reaction kinetics of the calendered electrodes. This observation can be clearly confirmed by the generated specific charge and discharge capacities and efficiencies (Table 38, Table 39 and Table 40).

Figure 92 shows the constant current cycling measurements of the calendered silicon/graphite composite electrodes without and with the addition of 10 w% glyceryltriacetate or triethylcitrate. These measurements confirm the results gained from the cycolvoltammetric measurements. As already seen at the constant current measurements of the uncalendered electrodes a slight capacity fading of the calendered and with 10 w% glyceryltriacetate or triethylcitrate manufactured composite electrode over 50 cycles is observable. Here, too, this phenomenon can be constituted by the change of the electrode porosity as a result of the addition of the plasticizer. As already mentioned in the context with the uncalendered electrodes an increase in the porosity of the electrode would determine an increase in the active electrode surface, which leads to an obvious, continuous electrolyte decomposition and, hence, to a modification in the performance of the electrode.

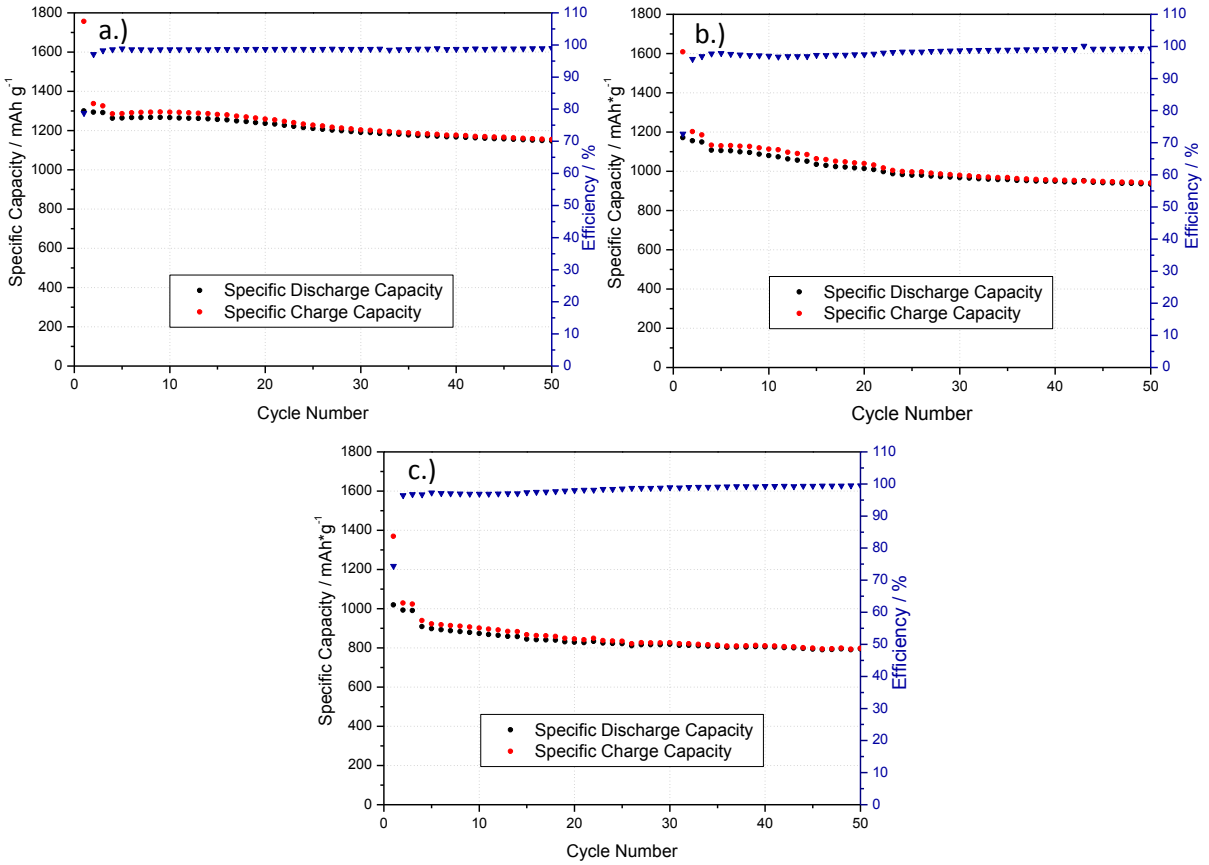

Figure 92: Constant current cycling of a.) a 30 % calendered silicon/graphite composite electrode [m (active layer) = 0,477 mg] vs. Li/Li$^+$; b.) a 30 % calendered silicon/graphite composite electrode [m (active layer) = 0,532 mg] with 10 w% glyceryltriacetate vs. Li/Li$^+$; c.) a 30 % calendered silicon/graphite composite electrode [m (active layer) = 0,697 mg] with 10 w% triethylcitrate vs. Li/Li$^+$; EC/DEC (3:7, v:v), 1 M $LiPF_6$, 2 v% VC; test program 2

To investigate the assumption that the plasticizers should be removed completely or at least partially during the first and second drying step of the electrodes at fine vacuum and a temperature of around 120°C (chapter 0, page 46) gas chromatography (GC)-mass spectrometry (MS) measurements were performed (chapter 4.5, page 56).

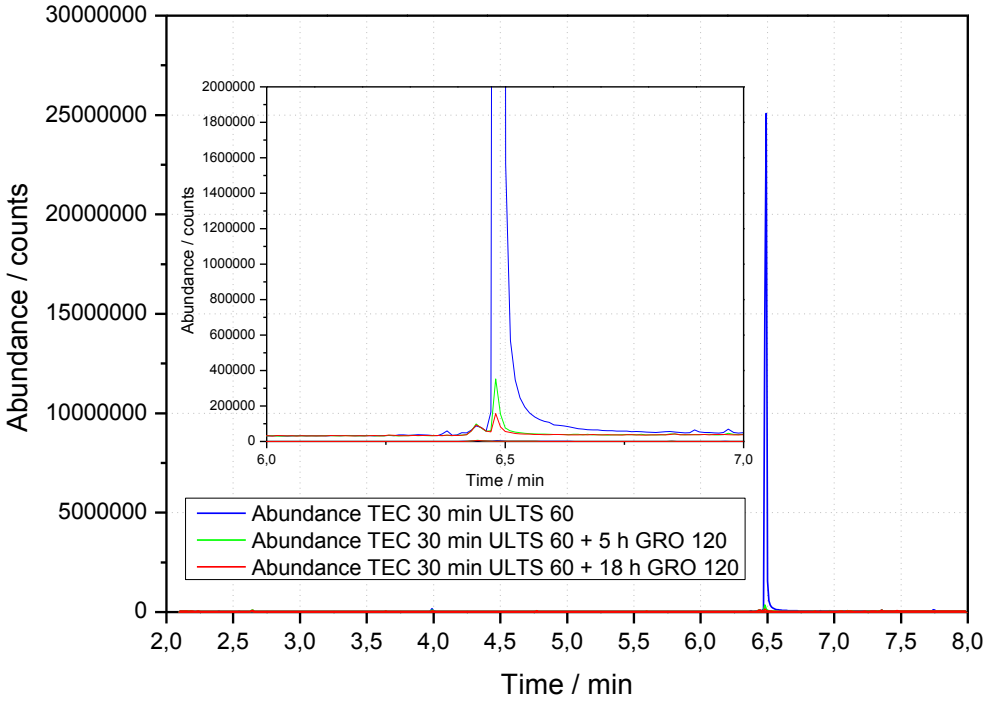

Figure 93: GC-MS measurements. Triethylcitrate within an electrode dried for 30 min within an air circulating compartment dryer at a temperature of 60°C (red line); triethylcitrate within an electrode dried for30 min within an air circulating compartment dryer at a temperature of 60°C and subsequently dried for 5 h within a glass tube furnish at a temperature of 120°C (blue line); triethylcitrate within an electrode dried for30 min within an air circulating compartment dryer at a temperature of 60°C and subsequently dried for 18 h within a glass tube furnish at a temperature of 120°C (black line)

Table 41: Quantitative evaluation of the amount of triethylcitrate within an electrode after several drying processes

Drying process	Amount of TEC after drying process [ppm]
30 min ULTS 60	926
30 min ULTS 60 + 5 h GRO 120	< 8
30 min ULTS 60 + 18 h GRO 120	< 8

The GC-MS measurements confirm the assumption that the plasticizer triethylcitrate is removed completely during the first and second drying step of the electrodes at fine vacuum and a temperature of around 120°C (chapter 0, page 46). Hence, the plasticizer shouldn´t influence the electrochemical performance of the electrodes.

As already mentioned, to enhance the possible amount of the partial water soluble plasticizers glyceryltriacetate or triethylcitrate within the electrode-paste the standard processing solvent “distilled water” was partially substituted by ethanol abs. to investigate the influence of the modified processing solvent on the performance of the electrode. In this connection five standard silicon/graphite composite electrode-pastes according to chapter 4.1.2.2 (page 49) were prepared, whereby the following H_2O dist./ethanol abs. solvent-mixtures were investigated as processing solvents:

- 0 v% ethanol abs. and 100 v% H_2O dist.
- 10 v% ethanol abs. and 90 v% H_2O dist.
- 20 v% ethanol abs. and 80 v% H_2O dist.
- 30 v% ethanol abs. and 70 v% H_2O dist.
- 40 v% ethanol abs. and 60 v% H_2O dist.

At this juncture it must be declared, that the following measurements don´t deliver the previous values due to the use of a nano-silicon powder from a different order. The silicon supplying company manufactures the silicon by the use of a batch operation and the qualities of the nano-silicon powder tremendously varies. The following measurements are among themselves comparable and enable a statement of the change in performance due to the modification of the electrodes.

Figure 94 - Figure 98 show the cyclovoltammogramms of uncalendered silicon/graphite composite electrodes as contrasted with calendered silicon/graphite composite electrodes with the use of the above mentioned H_2O dist./ethanol abs. solvent-mixtures as processing solvents. Table 42 - Table 51 illustrate the specific charge and discharge capacities and the efficiencies generated from the particular cyclovoltammogramms.

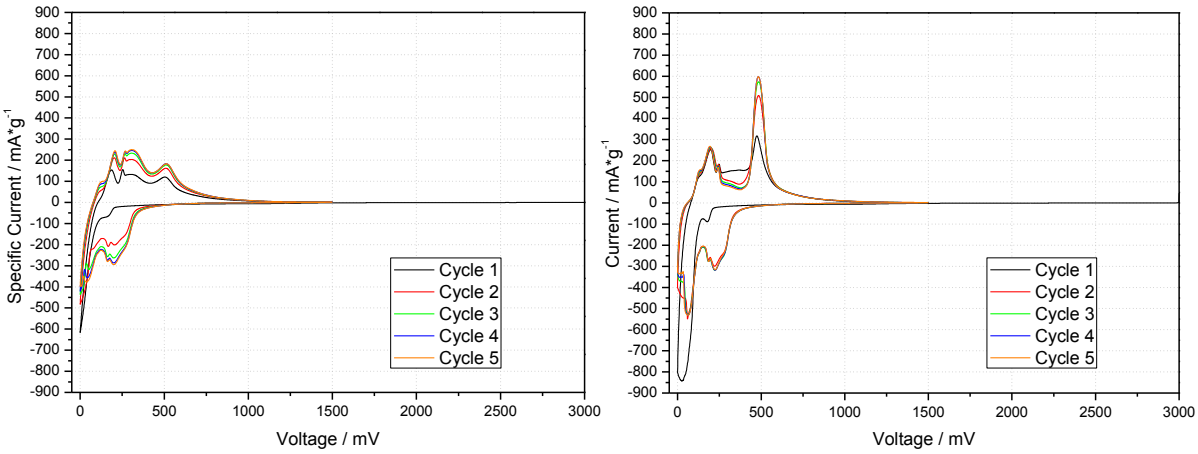

Figure 94: Cyclovoltammogramm of an uncalendered silicon/graphite composite electrode [m (active layer) = 2,190 mg] vs. Li/Li^+ (left) and a calendered silicon/graphite composite electrode (calendering rate: 20 %) [m (active layer) = 2,200 mg] vs. Li/Li^+ (right) with distilled water as processing solvent; EC/DEC (3:7, v:v), 1 M $LiPF_6$, 2 v% VC

Table 42: Specific charge capacity, specific discharge capacity and efficiency generated from the uncalendered silicon/graphite composite electrode cyclovoltammogramm in Figure 94 (left); processing solvent: 100 v% distilled water

Cycle	Specific Charge Capacity [$mAh \cdot g^{-1}$]	Specific Discharge Capacity [$mAh \cdot g^{-1}$]	Efficiency [%]
1	687	565	82
2	831	798	96
3	907	885	98
4	948	929	98
5	965	947	98

Table 43: Specific charge capacity, specific discharge capacity and efficiency generated from the calendered silicon/graphite composite electrode cyclovoltammogramm in Figure 94 (left); processing solvent: 100 v% distilled water

Cycle	Specific Charge Capacity [$mAh \cdot g^{-1}$]	Specific Discharge Capacity [$mAh \cdot g^{-1}$]	Efficiency [%]
1	1041	902	87
2	1040	1004	97
3	1031	1004	97
4	1023	999	98
5	1017	993	98

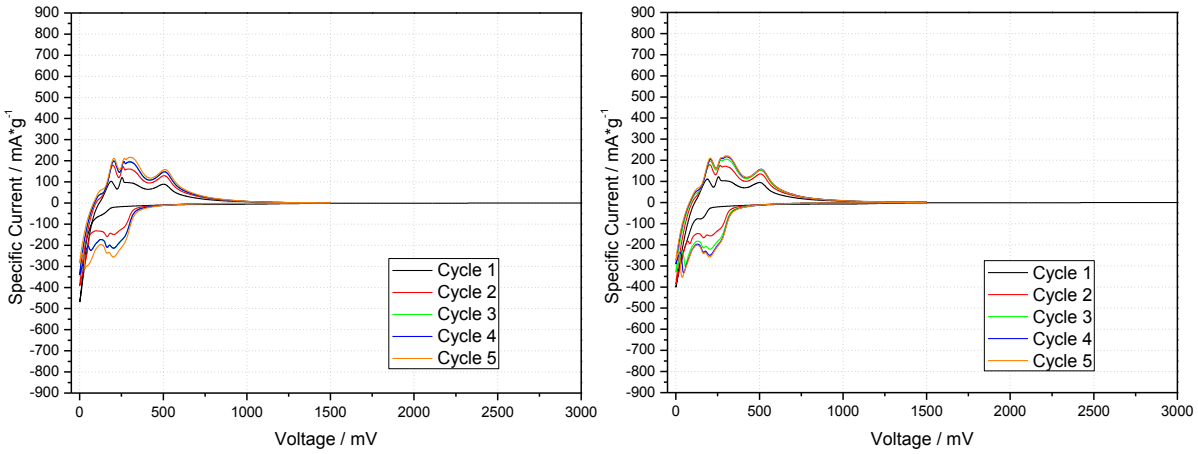

Figure 95: Cyclovoltammogramm of an uncalendered silicon/graphite composite electrode [m (active layer) = 2,060 mg] vs. Li/Li$^+$ (left) and a calendered silicon/graphite composite electrode (calendering rate: 20 %) [m (active layer) = 1,970 mg] vs. Li/Li$^+$ (right) with a mixture of 90 v% distilled water and 10 v% ethanol abs. as processing solvent; EC/DEC (3:7, v:v), 1 M $LiPF_6$, 2 v% VC

Table 44: Specific charge capacity, specific discharge capacity and efficiency generated from the uncalendered silicon/graphite composite electrode cyclovoltammogramm in Figure 95 (left); processing solvent: mixture of 90 v% distilled water and 10 v% ethanol abs.

Cycle	Specific Charge Capacity [mAh·g^{-1}]	Specific Discharge Capacity [mAh·g^{-1}]	Efficiency [%]
1	499	386	77
2	626	597	95
3	709	687	97
4	742	723	97
5	754	734	97

Table 45: Specific charge capacity, specific discharge capacity and efficiency generated from the calendered silicon/graphite composite electrode cyclovoltammogramm in Figure 95 (right); processing solvent: mixture of 90 v% distilled water and 10 v% ethanol abs.

Cycle	Specific Charge Capacity [mAh·g^{-1}]	Specific Discharge Capacity [mAh·g^{-1}]	Efficiency [%]
1	563	441	78
2	691	658	95
3	774	750	97
4	808	788	97
5	823	804	98

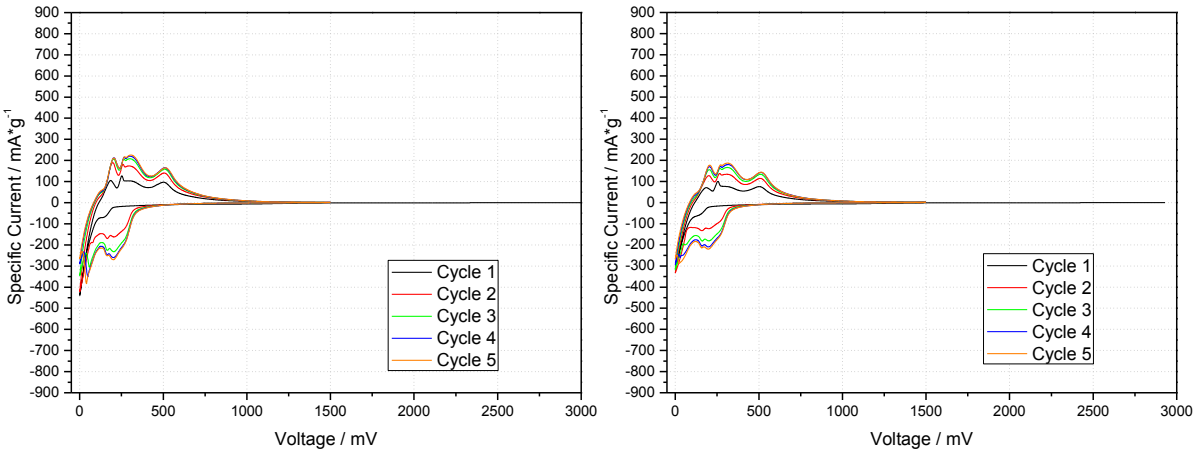

Figure 96: Cyclovoltammogramm of an uncalendered silicon/graphite composite electrode [m (active layer) = 2,200 mg] vs. Li/Li^+ (left) and a calendered silicon/graphite composite electrode (calendering rate: 20 %) [m (active layer) = 2,290 mg] vs. Li/Li^+ (right) with a mixture of 80 v% distilled water and 20 v% ethanol abs. as processing solvent; EC/DEC (3:7, v:v), 1 M $LiPF_6$, 2 v% VC

Table 46: Specific charge capacity, specific discharge capacity and efficiency generated from the uncalendered silicon/graphite composite electrode cyclovoltammogramm in Figure 96 (left); processing solvent: mixture of 80 v% distilled water and 20 v% ethanol abs.

Cycle	Specific Charge Capacity [$mAh \cdot g^{-1}$]	Specific Discharge Capacity [$mAh \cdot g^{-1}$]	Efficiency [%]
1	551	439	80
2	707	676	96
3	798	775	97
4	832	814	98
5	850	831	98

Table 47: Specific charge capacity, specific discharge capacity and efficiency generated from the calendered silicon/graphite composite electrode cyclovoltammogramm in Figure 96 (right); processing solvent: mixture of 80 v% distilled water and 20 v% ethanol abs.

Cycle	Specific Charge Capacity [$mAh \cdot g^{-1}$]	Specific Discharge Capacity [$mAh \cdot g^{-1}$]	Efficiency [%]
1	445	340	76
2	565	537	95
3	660	638	97
4	709	689	97
5	726	707	97

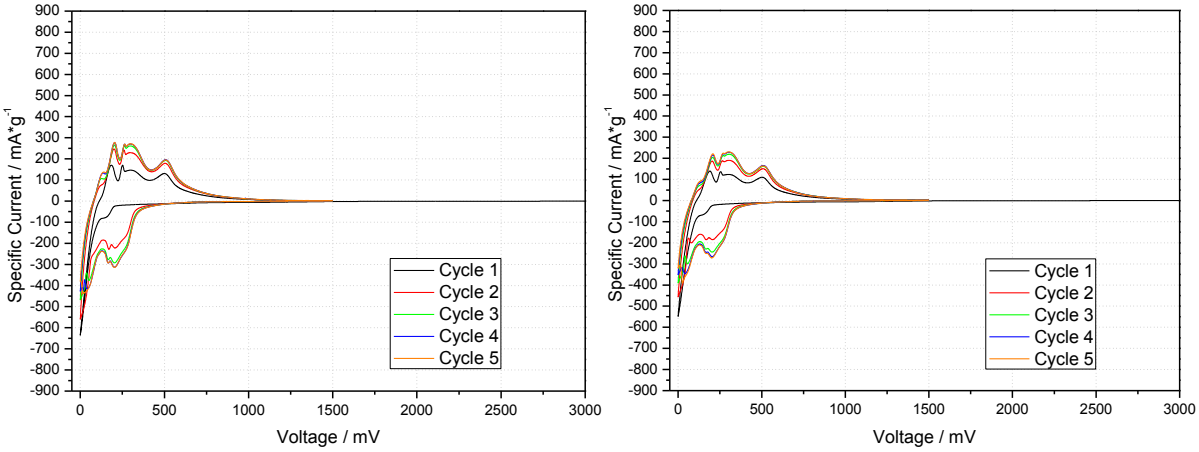

Figure 97: Cyclovoltammogramm of an uncalendered silicon/graphite composite electrode [m (active layer) = 1,690 mg] vs. Li/Li^+ (left) and a calendered silicon/graphite composite electrode (calendering rate: 20 %) [m (active layer) = 2,280 mg] vs. Li/Li^+ (right) with a mixture of 70 v% distilled water and 30 v% ethanol abs. as processing solvent; EC/DEC (3:7, v:v), 1 M $LiPF_6$, 2 v% VC

Table 48: Specific charge capacity, specific discharge capacity and efficiency generated from the uncalendered silicon/graphite composite electrode cyclovoltammogramm in Figure 97 (left); processing solvent: mixture of 70 v% distilled water and 30 v% ethanol abs.

Cycle	Specific Charge Capacity [$mAh \cdot g^{-1}$]	Specific Discharge Capacity [$mAh \cdot g^{-1}$]	Efficiency [%]
1	744	608	82
2	934	897	96
3	1006	982	98
4	1038	1018	98
5	1036	1018	98

Table 49: Specific charge capacity, specific discharge capacity and efficiency generated from the calendered silicon/graphite composite electrode cyclovoltammogramm in Figure 97 (right); processing solvent: mixture of 70 v% distilled water and 30 v% ethanol abs.

Cycle	Specific Charge Capacity [$mAh \cdot g^{-1}$]	Specific Discharge Capacity [$mAh \cdot g^{-1}$]	Efficiency [%]
1	605	489	81
2	726	693	96
3	796	772	97
4	824	803	97
5	828	810	98

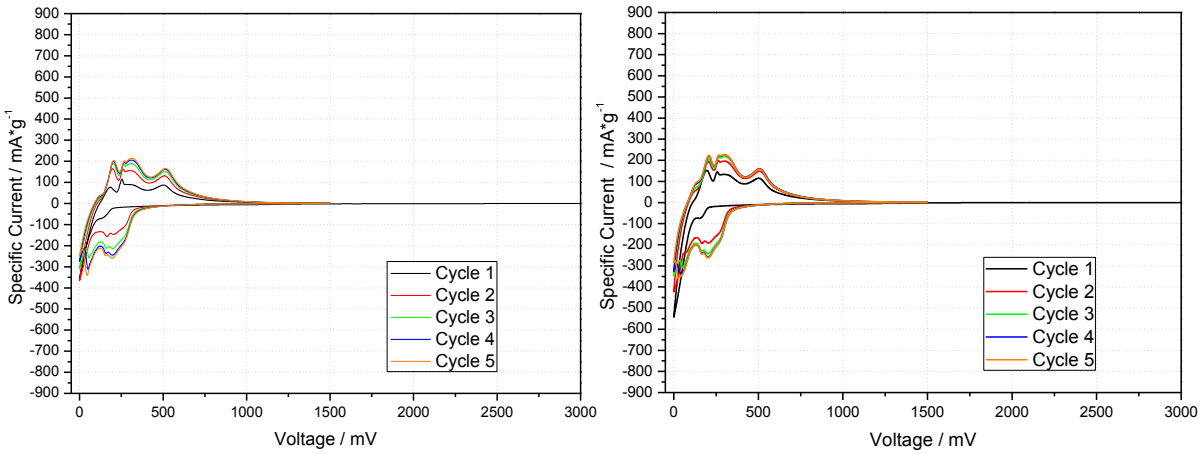

Figure 98: Cyclovoltammogramm of an uncalendered silicon/graphite composite electrode [m (active layer) = 2,190 mg] vs. Li/Li^+ (left) and a calendered silicon/graphite composite electrode (calendering rate: 20 %) [m (active layer) = 2,320 mg] vs. Li/Li^+ (right) with a mixture of 60 v% distilled water and 40 v% ethanol abs. as processing solvent; EC/DEC (3:7, v:v), 1 M $LiPF_6$, 2 v% VC

Table 50: Specific charge capacity, specific discharge capacity and efficiency generated from the uncalendered silicon/graphite composite electrode cyclovoltammogramm in Figure 98 (left); processing solvent: mixture of 60 v% distilled water and 40 v% ethanol abs.

Cycle	Specific Charge Capacity [$mAh \cdot g^{-1}$]	Specific Discharge Capacity [$mAh \cdot g^{-1}$]	Efficiency [%]
1	496	383	77
2	646	616	95
3	741	719	97
4	792	774	98
5	818	802	98

Table 51: Specific charge capacity, specific discharge capacity and efficiency generated from the calendered silicon/graphite composite electrode cyclovoltammogramm in Figure 98 (right); processing solvent: mixture of 60 v% distilled water and 40 v% ethanol abs.

Cycle	Specific Charge Capacity [$mAh \cdot g^{-1}$]	Specific Discharge Capacity [$mAh \cdot g^{-1}$]	Efficiency [%]
1	665	546	82
2	772	739	96
3	817	794	97
4	847	826	98
5	843	823	98

On consideration of the cyclovoltammogramms in Figure 94 - Figure 98 there are no obvious parasitic reactions caused by the use of an alternative H2O dist./ethanol abs. mixture as processing solvent observable. Notably are the sharp, high current peaks of the with 100 v% H_2O distilled as processing solvent manufactures calendered silicon/graphite composite electrode. These peaks are indicative of better reaction kinetics of this electrode. The specific charge and discharge capacities generated from the cyclovoltammogramms (Table 42 - Table 51) slightly vary. To make a clear statement about the performance of the electrodes processed with different processing solvents constant current cycling measurements were performed. Figure 99 shows the specific discharge capacities generated from the constant current cycling measurements of a standard processed calendered silicon/graphite composite electrodes in comparison to calendered silicon/graphite composite electrodes using the H_2O dist./ethanol abs. mixtures as electrode processing solvents. There are no obvious differences observable.

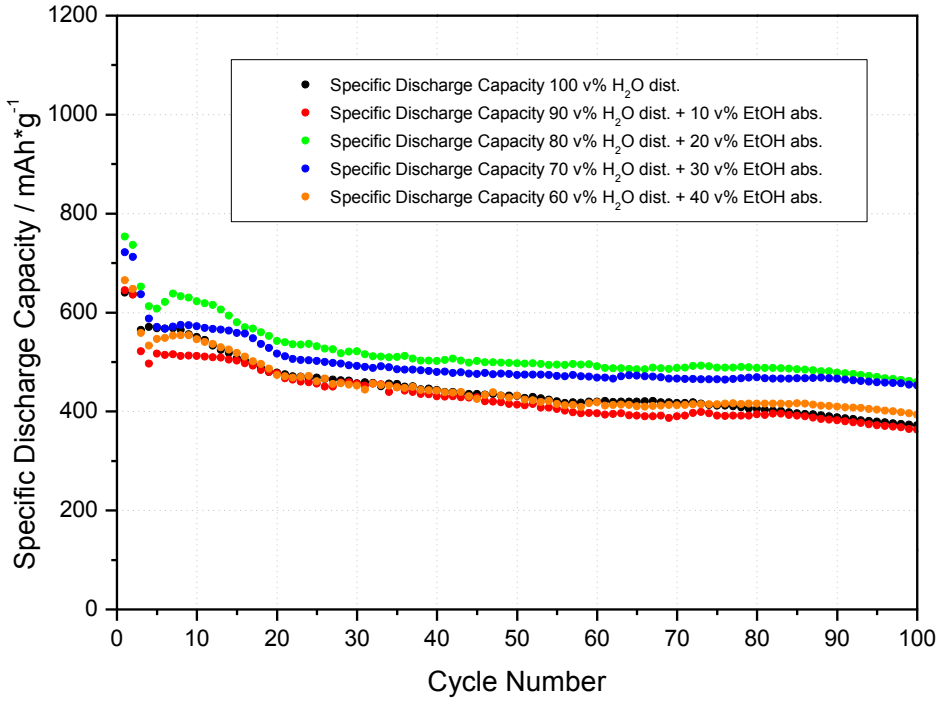

Figure 99: Specific discharge capacities generated of the constant current cycling measurements of a calendered silicon/graphite composite electrodes (calendering rate: 20 %) vs. Li/Li$^+$ with the use of different processing solvent mixtures; EC/DEC (3:7, v:v), 1 M $LiPF_6$, 2 v% VC; test program 2

6.2.2 Water Soluble Plasticizers – 1,2 Propanediol and Glycerin

In this connection a standard silicon/graphite composite electrode-paste according to chapter 4.1.2.2 (page 49) was prepared. 20 w% (calculated from the used overall mass of the electrode-paste) of the plasticizer 1,2 propanediol or glycerin were added after point 1 of the dispersing sequence (dissolving the Na-CMC binder in distilled water; page 49).

Figure 100 shows a cyclovoltammogramm of an uncalendered silicon/graphite composite electrode as contrasted with an uncalendered silicon/graphite composite electrode with the addition of 20 w% 1,2 propanediol or glycerin.

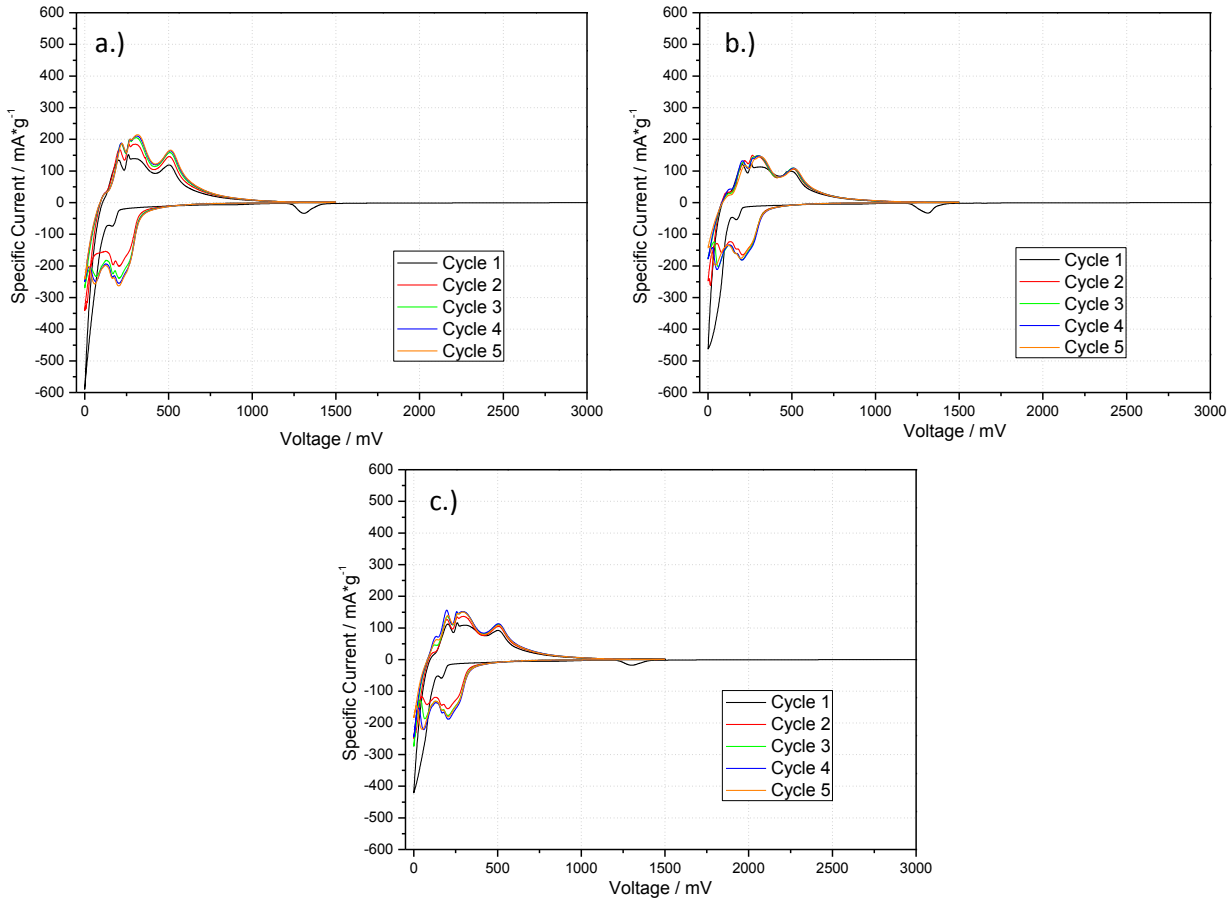

Figure 100: Cyclovoltammogramm of a.) an uncalendered silicon/graphite composite electrode [m (active layer) = 1,450 mg] vs. Li/Li$^+$; b.) an uncalendered silicon/graphite composite electrode [m (active layer) = 1,980 mg] with 20 w% 1,2 propanediol vs. Li/Li$^+$; c.) an uncalendered silicon/graphite composite electrode [m (active layer) = 1,890 mg] with 20 w% glycerin vs. Li/Li$^+$; EC/DEC (3:7, v:v), 1 M $LiPF_6$, 2 v% VC

Table 52, Table 53 and Table 54 illustrate the specific charge and discharge capacities and the efficiencies generated from the cyclovoltammogramms in Figure 100.

Table 52: Specific charge capacity, specific discharge capacity and efficiency generated from the cyclovoltammogramm of the uncalendered silicon/graphite composite electrode in Figure 100 a.)

Cycle	Specific Charge Capacity [mAh·g^{-1}]	Specific Discharge Capacity [mAh·g^{-1}]	Efficiency [%]
1	711	559	79
2	701	679	97
3	748	733	98
4	769	757	98
5	779	768	99

Table 53: Specific charge capacity, specific discharge capacity and efficiency generated from the cyclovoltammogramm of the uncalendered silicon/graphite composite electrode with 20 w% 1,2 propanediol in Figure 100 b.)

Cycle	Specific Charge Capacity [mAh·g^{-1}]	Specific Discharge Capacity [mAh·g^{-1}]	Efficiency [%]
1	600	477	80
2	543	524	96
3	537	523	97
4	550	538	98
5	522	513	98

Table 54: Specific charge capacity, specific discharge capacity and efficiency generated from the cyclovoltammogramm of the uncalendered silicon/graphite composite electrode with 20 w% glycerin in Figure 100 c.)

Cycle	Specific Charge Capacity [mAh·g^{-1}]	Specific Discharge Capacity [mAh·g^{-1}]	Efficiency [%]
1	550	440	80
2	523	499	96
3	564	547	97
4	593	577	97
5	586	573	98

The cyclovoltammogramms in Figure 100 show that the addition of the plasticizers causes no obvious parasitic reactions. The specific charge and discharge capacities and the efficiencies generated from the cyclovoltammogramms are nearly coincident. Thus, it can be determined that the addition of the plasticizer glyceryltriacetate or triethylcitrate during the electrode preparation process has no negative influence on the performance of the silicon/graphite composite electrode.

Figure 101 shows the constant current cycling measurements of the uncalendered silicon/graphite composite electrodes without and with the addition of 20 w% 1,2 propanediol or glycerin.

These measurements almost confirm the results gained from the cycolvoltammetric measurements, but there is a slight capacity fading of the with the plasticizer 1,2 propanediol or glycerin processed electrodes over 50 cycles observable. As already mentioned this capacity fading can be constituted by a modification of the electrode porosity. An increase in the porosity of the electrodes determines an increase in the active electrode surface. This fact leads to an obvious, continuous electrolyte decomposition and consequently to a worsening of the electrode performance.

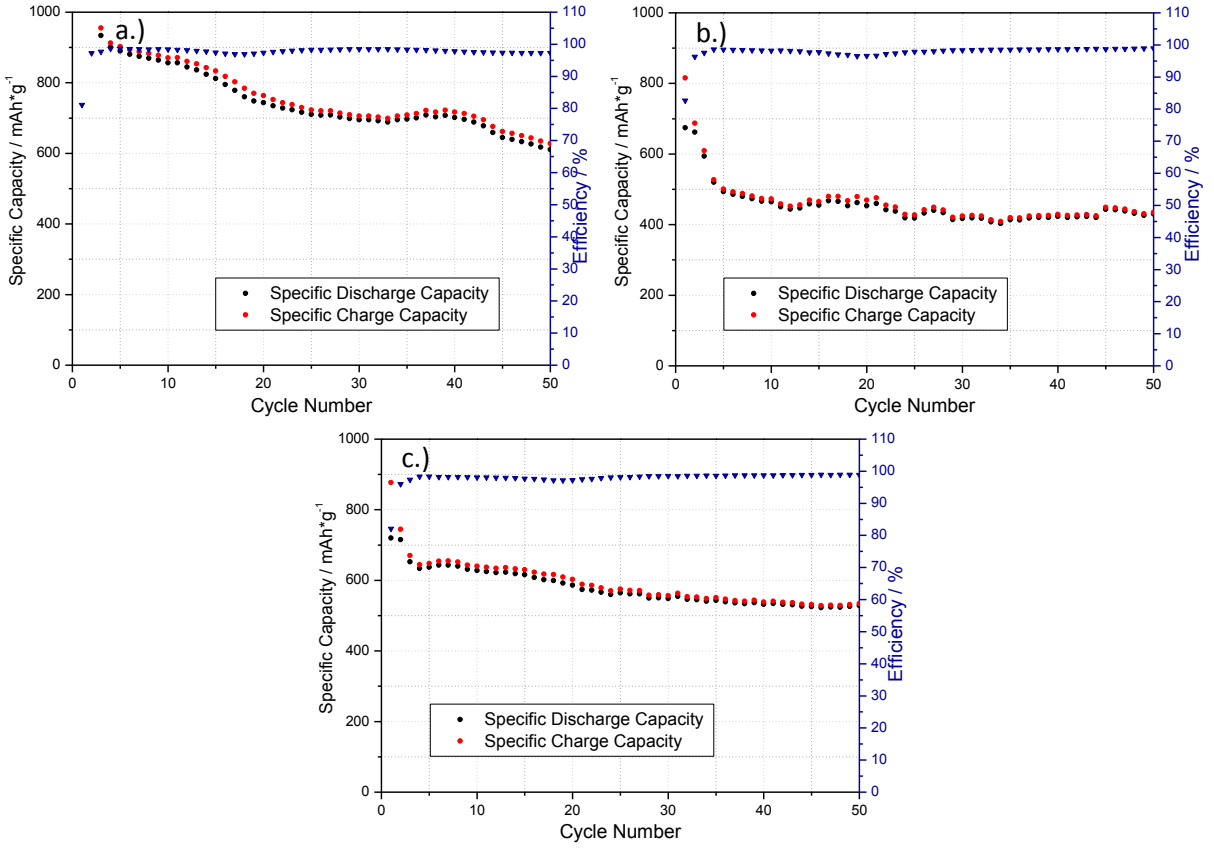

Figure 101: Constant current cycling of a.) an uncalendered silicon/graphite composite electrode [m (active layer) = 1,420 mg] vs. Li/Li$^+$; b.) an uncalendered silicon/graphite composite electrode [m (active layer) = 2,030 mg] with 20 w% 1,2 propanediol vs. Li/Li$^+$; c.) an uncalendered silicon/graphite composite electrode [m (active layer) = 1,820 mg] with 20 w% glycerin vs. Li/Li$^+$; EC/DEC (3:7, v:v), 1 M $LiPF_6$, 2 v% VC; test program 2

Figure 102 shows a cyclovoltammogramm of a calendered (calendering rate: 20 %) silicon/graphite composite electrode as contrasted with a calendered (calendering rate: 20 %) silicon/graphite composite electrode with the addition of 20 w% 1,2 propanediol or glycerin.

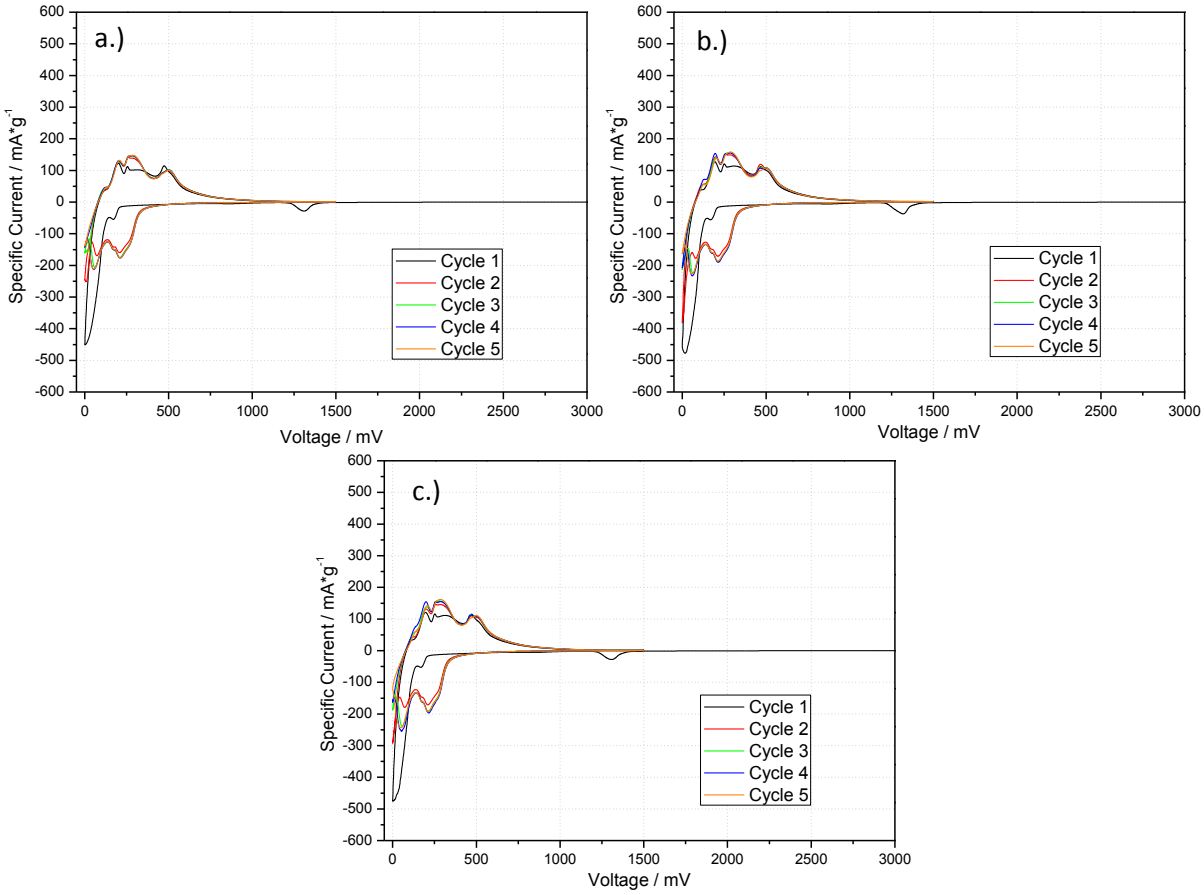

Figure 102: Cyclovoltammogramm of a.) a 20 % calendered silicon/graphite composite electrode [m (active layer) = 2,170 mg] vs. Li/Li$^+$; b.) a 20 % calendered silicon/graphite composite electrode [m (active layer) = 1,960 mg] with 20 w% 1,2 propanediol vs. Li/Li$^+$ (right); c.) a 20 % calendered silicon/graphite composite electrode [m (active layer) = 1,920 mg] with 20 w% glycerin vs. Li/Li$^+$; EC/DEC (3:7, v:v), 1 M $LiPF_6$, 2 v% VC

Table 55, Table 56 and Table 57 illustrate the specific charge and discharge capacities and the efficiencies generated from the cyclovoltammogramms in Figure 102.

Table 55: Specific charge capacity, specific discharge capacity and efficiency generated from the cyclovoltammogramm of the calendered silicon/graphite composite electrode in Figure 102 a.)

Cycle	Specific Charge Capacity [mAh·g^{-1}]	Specific Discharge Capacity [mAh·g^{-1}]	Efficiency [%]
1	577	465	81
2	524	505	96
3	531	515	97
4	528	514	97
5	522	509	98

Table 56: Specific charge capacity, specific discharge capacity and efficiency generated from the cyclovoltammogramm of the calendered silicon/graphite composite electrode with 20 w% 1,2 propanediol in Figure 102 b.)

Cycle	Specific Charge Capacity [mAh·g^{-1}]	Specific Discharge Capacity [mAh·g^{-1}]	Efficiency [%]
1	633	502	79
2	591	567	96
3	577	563	97
4	587	573	98
5	563	553	98

Table 57: Specific charge capacity, specific discharge capacity and efficiency generated from the cyclovoltammogramm of the calendered silicon/graphite composite electrode with 20 w% glycerin in Figure 102 c.)

Cycle	Specific Charge Capacity [mAh·g^{-1}]	Specific Discharge Capacity [mAh·g^{-1}]	Efficiency [%]
1	603	483	80
2	562	540	96
3	579	563	97
4	595	579	97
5	574	562	98

As was expected the cyclovoltammogramms of the 20 % calendered electrodes also don´t show any obvious parasitic reactions. The specific charge and discharge capacities and the efficiencies generated from the cyclovoltammogramms are nearly coincident and don´t differ from the values of the uncalendered electrodes.

Figure 103 shows the constant current cycling measurements of the 20 % calendered silicon/graphite composite electrodes without and with the addition of 20 w% 1,2 propanediol or glycerin.

The measurements almost confirm the results gained from the cycolvoltammetric measurements of the 20 % calendered electrodes and don´t show distinct improvements in comparison to the uncalendered electrodes.

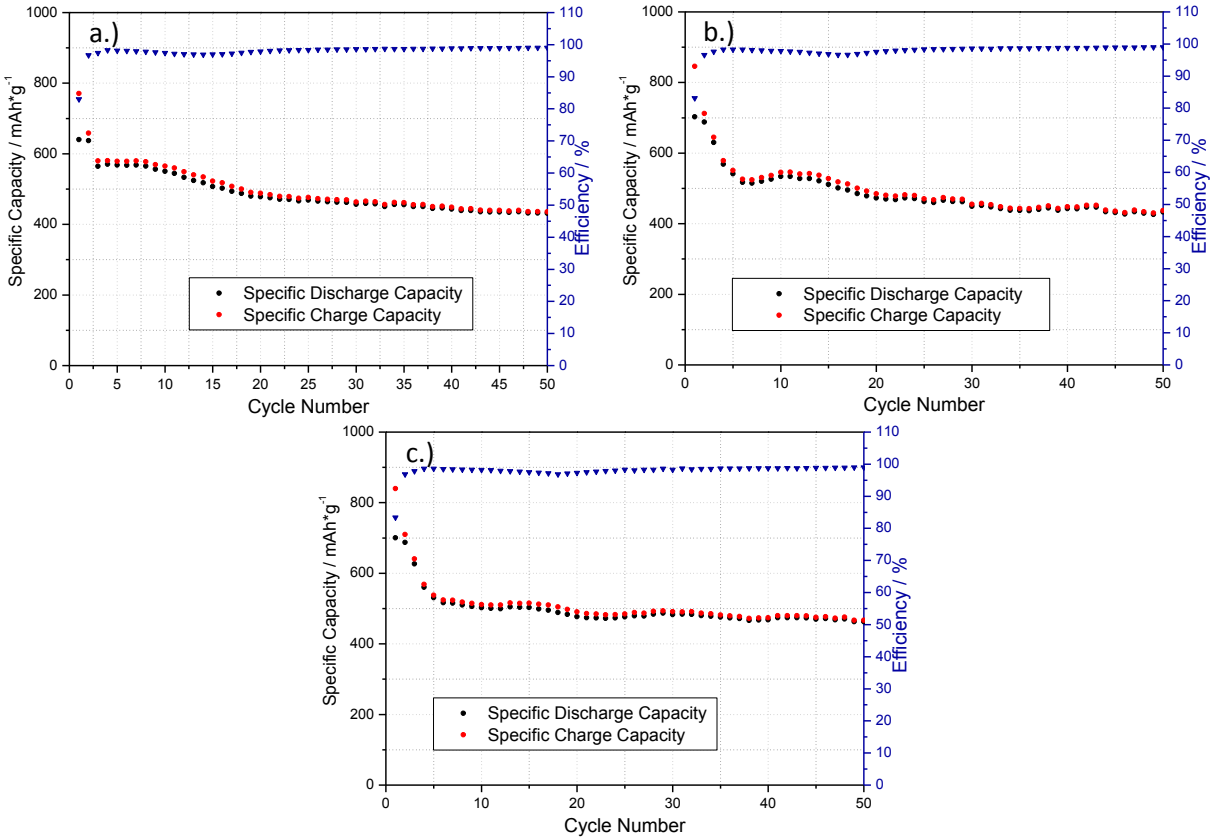

Figure 103: Constant current cycling of a.) a 20 % calendered silicon/graphite composite electrode [m (active layer) = 2,180 mg] vs. Li/Li$^+$; b.) a 20 % calendered silicon/graphite composite electrode [m (active layer) = 2,040 mg] with 20 w% 1,2 propanediol vs. Li/Li$^+$; c.) a 20 % calendered silicon/graphite composite electrode [m (active layer) = 1,940 mg] with 20 w% glycerin vs. Li/Li$^+$; EC/DEC (3:7, v:v), 1 M $LiPF_6$, 2 v% VC; test program 2

7 Conclusion

„Der härteste und wichtigste Kampf des 21. Jahrhunderts wird ohne Waffen geführt. Die Werkzeuge dieses Kampfes heißen: Energieeffizienz, Energie sparen und erneuerbare Energien.“[108]

Franz Alt

Facing recent and future challenges in the field of electrochemical energy storage, the miniaturization of portable electronic devices and at least the partial replacement of fossil fuels in the scope of the automotive industry, the lithium-ion battery technology seems to be the key technology. But to satisfy all these requirements an enhancement of the specific energy ($Wh \cdot kg^{-1}$) and the energy density ($Wh \cdot l^{-1}$) is essential. One opportunity to accomplish this purpose is to substitute the common graphitic carbon anode materials by intermetallic anode materials, like for example silicon. But until now silicon didn´t prevail against the graphitic carbons due to several disadvantages, like the enormous volume changes of the active material during the lithiation/delithiation process, which leads to a rapid decay of the capacity.

Hence, the object of this work was the improvement of high capacity silicon anodes for lithium-ion batteries. In this connection two possible approaches were pursued - one is the modification of the electrode preparation process and secondary the modification of a high purity nano-scaled silicon powder.

The common binders for negative silicon or silicon/carbon composite electrodes are sodium-carboxymethylcellulose or other cellulose based binder systems. Cellulose-derivates constitute thermosetting properties and although these properties are favorable for the cycling stability of silicon and silicon/carbon composite electrodes, they impede the electrode processing. An exfoliation of the brittle electrode-paste from the current collector foil during the drying process and a worse consistency against mechanical load during the manufacturing of the electrodes, like rolling and pressing, are two possible consequences of the thermosetting properties of cellulose based binder systems. In this context, the influence of the addition of a plasticizer to the electrode-paste was determined. Two partially water soluble plasticizers, glyceryltriacetate and triethylcitrate, and two water soluble plasticizers, 1,2 propanediol and glycerin, were investigated. The addition of a plasticizer simplifies the electrode manufacturing process and has nearly no unfavorable effect on the electrode performance. It can be assumed that each of the above mentioned plasticizers are removed completely or at least partially during the first and second drying step of the electrodes at fine vacuum and a temperature of around 120°C. In the case of electrodes, which are manufactured with a plasticizer, there is only a slight capacity fading over 50 cycles observable. This can be

constituted by a modification of the porosity of the electrode. An increase in the porosity of the electrode would determine an increase in the active electrode surface, which leads to a continuous electrolyte decomposition and, hence, to a modification in the performance of the electrode.

The second approach to enhance the specific energy respectively the energy density of a lithium-ion battery was the modification of a high purity nano-scaled silicon powder. In this case we proceed on the assumption, that the presence of a hetero-atom within high purity, nano-scaled silicon powder causes a decrease of the free enthalpy of the lithium/silicon alloy and a formation of a higher lithiated phase is consequently favored. The modification was done by means of preliminary fractional alloying from the gaseous phase with the materials sodium and potassium and by solid state diffusion with a sodium-potassium alloy and the materials calcium and magnesium. To investigate the different preliminary fractional alloyed silicon powders electrodes were manufactured and electrochemical and analytical measurements were performed. In summary it can be said, that the preliminary fractional alloying of the high purity, nano-scaled silicon powder D with sodium, potassium and the sodium/potassium alloy has a positive effect on the performance of the active material, whereby the best results could be achieved with sodium. Based on the above mentioned theory X-ray diffraction measurements of the cycled and with sodium preliminary fractional alloyed silicon D electrodes were performed. There was a change in the crystal structure of the cycled and sodium preliminary fractional alloyed silicon D electrode in comparison to the cycled high purity silicon D electrode observable. Unfortunately, the results gained from the X-ray diffraction measurements don´t provide a clear statement concerning the arising lithium/silicon phase. To get more information about the formed silicon/lithium phase an improvement of the experimental setup and the special ex-situ XRD cell would be meaningful and is at present content of further works on this topic.

8 Appendix

8.1 List of Abbreviations

8.1.1 Miscellaneous

A	anode
aq	aqueous
C	cathode
c	concentration
CCCV	constant current constant voltage
CE	counter electrode
C_{irr}	irreversible capacity
CV	cyclovoltammogramm
E	(equilibrium) cell voltage
E^0	standard (redox) potential
EDX	energy-dispersive X-ray spectroscopy
EMF	electromotive force
EV	electric vehicle
F	Farady constant
g	gaseous
G	free (reaction) enthalpy
GRO	glass tube furnish
H	(reaction) enthalpy
HEV	hybrid electric vehicle
HRTEM	high resolution transmission electron microscopy
I	current
IHP	inner Helmholtz plane
µ	chemical potential
Na-CMC	sodium carboxy methylcellulose

NHE	normal hydrogen electrode
η	overpotential
OCV	open circuit voltage
OHP	outer Helmholtz plane
ox	oxidation
P	power
p	pressure
Q	charge
R	universal gas constant
RE	reference electrode
red	reduction
RTIL	room temperature ionic liquid
S	(reaction) entropy
SEM	scanning electron microscope
T	temperature
t	time
U	voltage
ULTS	air circulation compartment dryer
V	volume
WE	working electrode

8.1.2 Chemicals

AN	acetonitrile
DBP	dibutyl phthalate
DEC	diethyl carbonate
DIDP	diisodecyl phthalate
DINP	diisononyl phthalate

DIOX	1,3-dioxolane
DMC	dimethyl carbonate
DME	dimethoxy ethane
DMSO	dimethyl sulfoxide
EC	ethylene carbonate
EMC	ethylmethyl carbonate
F_2O_3	fluorine oxide
GBL	γ-butyrolactone
KS 6	special graphite
$LiAsF_6$	lithium hexafluoroarsenate
$LiBF_4$	lithium tetrafluoroborate
$LiClO_4$	lithium perchlorate
$LiCoO_2$	lithium cobalt oxide
$LiCoPO_4$	lithium cobalt phosphate
$LiFePO_4$	lithium iron phosphate
$LiMnO_4$	lithium manganese oxide
$LiMnPO_4$	lithium manganese phosphate
$LiMoO_2$	lithium molybdenum oxide
$LiNiPO_4$	lithium nickel phosphate
$LiPF_6$	lithium hexafluorophosphate
LiTf	lithium triflat
$LiTi_5O_{12}$	lithium titanium oxide
LiTFSI	lithium trifluorosulfonimide
Na-CMC	sodium carboxymethylcellulose
MA	methyl acetate
MF	methyl formate
Mn_2O_4	manganese oxide
MSC	methansulfonyl chloride

MoO_x	molybdenum oxide
n-BU	n-butylamine
PC	propylene carbonate
PVC	polyvinyl chloride
PVdF	polyvinylidene fluoride
$PYR_{13}FSI$	N-methyl-N-propyl pyrrolidinium bis(fluorosulfonyl)imide
silicon D	nano-scaled silicon powder of the firm Evonik (former degussa)
silicon L	nano-scaled silicon powder of the firm Los Alamos
TiO_2	titanium oxide
TMS, SL	sulfolane
THF	tetrahydrofuran
3Me2Ox	3-methyl-2-oxazolidinone
2MeTHF	2-methyltetrahydrofuran
VC	vinylene carbonate
WO_2	tungsten oxide

9 References

1. **J.-M. Tarascon, M. Armand.** *Nature.* 2001, 414, pp. 359-367.

2. Karlsruher Insitut für Technologie. [Online] [Cited: 07 07, 2011.] http://www.itas.fzk.de/tatup/103/flwe10a.htm.

3. Motorlexikon. [Online] [Cited: 05 12, 2011.] http://www.motorlexikon.de/?I=9478.

4. **M. Trzesniowski.** *Rennwagentechnik - Grundlagen, Konstruktion, Komponenten, Systeme.* Wiesbaden/Germany : Vieweg+Teubner Verlag / Springer Fachmedien GmbH, 2010.

5. **U. Kasavajjula, C. Wang, A. J. Appleby.** *Journal of Power Sources.* 2007, 163, pp. 1003-1039.

6. GRS-Batterien. [Online] [Cited: 07 26, 2011.] http://www.grs-batterien.de/fileadmin/user_upload/Download/Wissenswertes/Infomaterial_2010/GRS_welt_der_batterien.pdf.

7. Technick.net. [Online] [Cited: 04 18, 2011.] http://www.technick.net/public/code/cp_dpage.php?aiocp_dp=guide_bpw2_c01_01.

8. Tec Channel. [Online] [Cited: 04 18, 2011.] http://www.tecchannel.de/pc_mobile/notebook/402123/aktuelle_und_zukuenftige_akkutechnologien/index3.html.

9. **R. M. Dell, D. A. J. Rand.** *Understanding Batteries.* Cambridge/England : The Royal Society of Chemistry, 2001.

10. Bioanalytical Systems Inc. [Online] [Cited: 04 18, 2011.] http://www.basinc.com/library/history/97/.

11. Leuze Verlag. [Online] [Cited: 04 28, 2011.] http://www.leuze-verlag.de/gt/heft/aufsatz/200507%5CGT-1600-1610.pdf.

12. Fareastgizmos.com. [Online] [Cited: 04 28, 2011.] http://www.fareastgizmos.com/other_stuff/sony_monthly_lithium_ion_battery_production_to_reach_74_million_units_in_2010.php.

13. **R. Narayan, B. Viswanathan.** *Chemical and Electrochemical Energy Systems.* India : Universities Press (India) Limited, 1998.

14. **V. S. Bagotsky.** *Fundamentals of Electrochemistry.* Hoboken/New Jersey : John Wiley & Sons, Inc., 2006.

15. **J. O. Besenhard.** *Handbook of Battery Materials.* Weinheim/Germany : Wiley-VCH Verlag GmbH, 1999.

16. **H. A. Kiehne.** *Battery Technology Handbook.* Renningen-Malsheim/Germany : Expert Verlag GmbH, 2000.

17. **P. W. Atkins.** *Physikalische Chemie.* Weinheim/Germany : Wiley-VCH Verlag GmbH, 2001.

18. **G. Kickelbick.** *Chemie für Ingenieure.* München/Germany : Pearson Education Deutschland GmbH, 2008.

19. **C. God.** Doctoral Thesis. University of Technology Graz : s.n., 2011.

20. **L. Bergmann, C. Schaefer.** *Lehrbuch der Experimentalphysik-Elektromagnetismus.* Berlin/Germany : Walter de Gruyter GmbH & Co KG, 1999.

21. Lemon Car Competition. [Online] [Cited: 04 17, 2011.] https://egmanual.poly.edu/index.php?title=Lemon_Car.

22. **C. Obermaier.** *Nanostrukturierung mittelks Rasterkraftmikroskopie und Elecktrochemie.* Göttingen/Germany : Cuvillier Verlag, 2005.

23. **C. H. Hamann, A. Hamnett, W. Vielstich.** *Electrochemistry.* Weinheim/Germany : Wiley-VCH Verlag GmbH, 1998.

24. **K. J. Vetter.** *Electrochemical Kinetics: Theoretical and Experimental Aspects.* New York/USA : Academic Press Inc., 1967.

25. **Z. Ahmad.** *Principles of Corrosion Engineering and Corrosion Control.* Oxford/United Kingdom : Elsevier Ltd., 2006.

26. Corrosion Doctors. [Online] [Cited: 04 19, 2011.] http://www.corrosion-doctors.org/Corrosion-Kinetics/Overpotential-definition.htm.

27. **N. Kanani.** *Electroplating: Basic Principles, Processes and Practice.* Elsevier Ltd. : Oxford/United Kingdom, 2004.

28. TU Berlin. [Online] [Cited: 07 26, 2011.] http://www.mdt.tu-berlin.de/fileadmin/fg184/Lehre/Projekte/projekt-battery-model-andre.pdf.

29. Wikipedia. [Online] [Cited: 04 18, 2011.] http://de.wikipedia.org/wiki/Elektrische_Ladung.

30. A123. [Online] [Cited: 01 11, 2011.] http://www.a123systems.com/a123/products.

31. **G.-A. Nazri, G. Pistoia.** *Lithium Batteries: Science and Technology.* Dordrecht/Netherlands : Kluwer Academic Publishers, 2004.

32. **C. Julien, Z. Stoynov.** *Materials for Lithium-Ion Batteries.* Dordrecht/Netherlands : Kluwer Academic Publishers, 2000.

33. **M. Winter, J. O. Besenhard, M. E. Spahr, P. Novak.** *Advanced Materials.* 1998, 10, pp. 725-763.

34. **S. Koller.** Doctoral Thesis. *About the Nature of the Electrochemical Formation of Binary Lithium-Silicon Intermetallic Phases from Nonaqueous Electrolytes.* University of Technology Graz : s.n., 2009.

35. **V. V. Kharton.** *Handbook of Solid State Electrochemistry.* Weinheim/Germany : Wiley-VCH Verlag GmbH, 2009.

36. **N. S. Hochgatterer.** Zellulosechemie in der Lithium-Ionen Technologie. *Doctoral Thesis.* University of Technology Graz : s.n., 2008.

37. **J. Maier.** *Journal of Power Sources.* 2007, 174, pp. 569-574.

38. **X. Y. Song, K. Kinoshita.** *Journal of the Electrochemical Society.* 1996, 143, pp. L120-L123.

39. **M. Wakihara.** *Materials Science and Engineering.* 2001, R33, pp. 109-134.

40. **J. L. Tirado.** *Materials Science anmd Engineering.* 2003, R 40, pp. 103-136.

41. **J. R. Dahn.** *Physical Reviews B.* 1991, 44, pp. 9170-9177.

42. **T. Ohzuku, Y. Iwakoshi, K. Sawai.** *Journal of the Electrochemical Society.* 1993, 140, pp. 2490-2498.

43. **H. Azuma, H. Imoto, S. Yamada, K. Sekai.** *Journal of Power Sources.* 1999, 81-82, pp. 1-7.

44. **J. R. Dahn, T. Zheng, Y. Liu, J. S. Xue.** *Science.* 1995, 270, pp. 590-593.

45. **Y. Liu, J. S. Xue, T. Zheng, J. R. Dahn.** *Carbon.* 1996, Vol. 2, 37, pp. 193-200.

46. **Dey, A. N.** *Journal of the Electrochemical Society.* 1971, 118, pp. 1547-1549.

47. **R. A. Sharma, R. N. Seefurth.** *Journal of the Electrochemical Society.* 1976, 123, pp. 1763-1768.

48. **J. Yang, M. Winter, J. O. Besenhard.** *Solid State Ionics.* 1996, 90, pp. 281-287.

49. **J. O. Besenhard, J. Yang, M. Winter.** *Journal of Power Sources.* 1997, 68, pp. 87-90.

50. **B. Fuchsbichler, C. Stangl, H. Kren, F. Uhlig, S. Koller.** *Journal of Power Sources.* 2011, 196, pp. 2889-2892.

51. **C.-M. Park, J.-H. Kim, H. Kim, H.-J. Sohn.** *Chemical Society Reviews.* 2010, 39, pp. 3115-3141.

52. **Y. P. Wu, E. Rahm, R. Holze.** *Electrochimica Acta.* 2002, 47, pp. 3491-3507.

53. **K. Zaghib, C.M. Julien, J. Prakasch.** *New Trends in Intercalation Compunds for Energy Storage Conversion.* New Jersey/USA : The Electrochemical Society, Inc., 2003.

54. **H. Gabrisch, R. Yazami, B. Fultz.** *Journal of the Electrochemical Society.* 2004, 151, pp. A891-A897.

55. Wikipedia. [Online] [Cited: 08 2011, 04.] http://de.wikipedia.org/wiki/Kobalt.

56. **D. D. MacNeil, Z. Lu, J. R. Dahn.** *Journal of the Electrochemical Society.* 2002, 149, pp. A912-A919.

57. **J. Jiang, K. W. Eberman, L. J. Krause, J. R. Dahn.** *Journal of the Electrochemical Society.* 2005, 152, pp. A1874-A1878.

58. **M. M. Thackeray, A. de Kock, M. H. Rossouw, D. Liles.** *Journal of the Electrochemical Society.* 1992, 139, pp. 363-366.

59. **G. Amatucci, J.-M. Tarascon.** *Journal of the Electrochemical Society.* 2002, 12, pp. K31-K46.

60. **R. J. Gummow, M. M. Thackeray.** *Journal of the Electrochemical Society.* 1994, 141, pp. 1178-1182.

61. **A. Yamada.** *Journal of Solid State Chemistry.* 1996, 122, pp. 160-165.

62. **X. Li, Y. Xu, C. Wang.** *Journal of Alloys and Compounds.* 479, pp. 310-313.

63. **D. Morgan, A. Van der Ven, G. Ceder.** *Electrochemical and Solid State Letters.* 2004, 7, pp. A30-A32.

64. **W. F. Howard, R. M. Spotnitz.** *Journal of Power Sources.* 2007, 165, pp. 887-891.

65. **A. K. Padhi, K.S. Nanjundaswamy, J. B. Goodenough.** *Journal of the Electrochemical Society.* 1997, 144, pp. 1188-1194.

66. **M. Yoshio, R. J. Brodd, A. Kozawa.** *Lithium-Ion Batteries - Science and Technologies.* New York/USA : Springer Science + Business Media, 2009.

67. **W.-R. Liu, M.-H. Yang, H.-C. Wu, S. M. Chiao, N.-L. Wu.** *Electrochemical and Solid State Letters.* 2005, 8 (2), pp. A100-A103.

68. **H. Buqa, M. Holzapfel, F. Krumeich, C. Veit, P. Novak.** *Journal of Power Sources.* 161, pp. 617-622.

69. **J. Li, R. B. Lewis, J. R. Dahn.** *Electrochemical and Solid State Letters.* 2007, 10 (2), pp. A17-A20.

70. **B. Lestriez, S. Bahri, I. Sandu, L. Roue, D. Guyomard.** *Electrochemistry Communications.* 2007, 9, pp. 2801-2806.

71. **N. S. Hochgatterer, M. R. Schweiger, S. Koller, P.R. Raimann, T. Wöhrle, C. Wurm, M. Winter.** *Electrochemical and Solid State Letters.* 2008, 11, pp. A76-A80.

72. **G. T. Kim, S. S. Jeong, M. Joost, E. Rocca, M. Winter, S. Passerini, A. Balducci,.** *Journal of Power Sources.* 2011, 196, pp. 2187-2194.

73. **A. Lewandowski, A. Swiderska-Mocek.** *Journal of Power Sources.* 2009, 194, pp. 601-609.

74. **M. Galinski, A. Lewandowski, I. Stepniak.** *Electrochimica Acta.* 2006, 51, pp. 5567-5580.

75. **G. B. Appetecchi, M. Montanino, A. Baldussi, S. F. Lux, M. Winter, S. Passerini.** *Journal of Power Sources.* 2009, 192, pp. 599-605.

76. **K. Xu.** *Chemical Reviews.* 2004, 104, pp. 4303-4418.

77. **T. Nakajima, H. Groult (eds.).** *Fluorinated Materials for Energy Conversion.* Amsterdam/Netherlands : Elsevier, 2005.

78. **J. T. Dudley, D. P. Wilkinson, G. Thomas, R. LeVae, S. Woo, H. Blom, C. Horvath, M. W. Juzkow, B. Denis, P. Juric, P. Aghakian, J. R. Dahn.** *Journal of Power Sources.* 1991, 35, pp. 59-82.

79. **Y. Matsuda, M. Morita, K. Kosaka.** *Journal of the Electrochemical Society.* 1983, 130, pp. 101-104.

80. **S. Koller, M. Schmuck.** Batteries and Supercapacitors. *Lecture.* University of Technology Graz : s.n., 2010.

81. **D. Aurbach, K. Gamolsky, B. Markovsky, Y. Gofer, M. Schmidt, U. Heider,.** *Electrochimica Acta.* 2002, 47, pp. 1423-1439.

82. **B. B. Owens.** *Journal of Power Sources.* 2000, 90, pp. 2-8.

83. **K. M. Kim, J. M. Ko, N.-G. Park, K. S. Ryu, S. H. Chang.** *Solid State Ionics.* 2003, 161, pp. 121-131.

84. **J. Saunier, F. Alloin, J.Y. Sanchez, G. Caillon.** *Journal of Power Sources.* 2003, 119-121, pp. 454-459.

85. **P. Novak, F. Joho, R. Imhof, J.-C. Panitz, O. Haas.** *Journal of Power Sources.* 1999, 81-82, pp. 212-216.

86. **J. Li, C. Daniel, D. Wood.** *Journal of Power Sources.* 2011, 196, pp. 2452-2460.

87. **P. Arora, Z. Zhang.** *Chemical Reviews.* 2004, 104, pp. 4419-4462.

88. Büchi Labortechnik. [Online] [Cited: 05 25, 2011.] http://www.buechigmbh.de/Glasofen-B-585-Drying.3314.0.html.

89. Wikipedia. [Online] [Cited: 06 17, 2011.] http://de.wikipedia.org/wiki/Cyclovoltammetrie.

90. **C. Bayer.** Diploma Thesis. *Elektrolytkomponenten für Hochleistungs-Lithium-Ionen Batterien.* University of Technology Graz : s.n., 2008.

91. Wikipedia. [Online] [Cited: 07 2011, 05.] http://en.wikipedia.org/wiki/Scanning_electron_microscope.

92. Wikipedia. [Online] [Cited: 08 05, 2011.] http://en.wikipedia.org/wiki/X-ray_diffraction.

93. Wikipedia. [Online] [Cited: 08 18, 2011.] http://en.wikipedia.org/wiki/Gas_chromatography%E2%80%93mass_spectrometry.

94. **B. A. Boukamp, G. C. Lesh, R. A. Huggins.** *Journal of the Electrochemical Society.* 1981, 128, pp. 725-728.

95. **H. Li, X. Huang, L. Chen, G. Zhou, Z. Zhang, D. Yu, Y. J. Mo, N. Pei.** *Solid State Ionics.* 2000, 135, pp. 181-191.

96. **P. Limthongkul, Y.-I. Jang, N. J. Dudney, Y.-M. Chiang.** *Journal of Power Sources.* 119-121, pp. 604-609.

97. **M. N. Obrovac, L. Christensen.** *Electrochemical and Solid State Letters.* A93-A96, pp. A93-A96.

98. **T. D. Hatchard, J. R. Dahn.** *Journal of the Electrochemical Society.* 151, pp. A838-A842.

99. **J. Li, J. R. Dahn.** *Journal of the Electrochemical Society.* 154, pp. A156-A161.

100. **Y. Kubota.** *Journal of Applied Physics.* 2007, 102, pp. 053704-1-053704-6.

101. Wikipedia. [Online] [Cited: 08 05, 2011.] http://de.wikipedia.org/wiki/Natrium#cite_note-crc-5.

102. Uni Basel. [Online] [Cited: 08 05, 2011.]
http://www.physik.unibas.ch/Praktikum/VPII/SternGerlach/Kalium_Sicherheitsdatenblatt.pdf.

103. European Council for Plasticisers and Intermediates. [Online] [Cited: 06 21, 2011.]
http://www.ecpi.org/default.aspx?page=5.

104. Plasticicers and Flexible PVC Information Centre. [Online] [Cited: 06 21, 2011.]
http://www.plasticisers.org/.

105. Umwelt-Bundesamt. [Online] [Cited: 06 21, 2011.]
http://www.umweltbundesamt.de/gesundheit/stoffe/weichmacher.htm.

106. Wikipedia. [Online] [Cited: 07 07, 2011.]
http://de.wikipedia.org/wiki/Liste_der_in_der_Europ%C3%A4ischen_Union_zugelassenen_Lebensmittelzusatzstoffe.

107. National Institute of Standards and Technology. [Online] [Cited: 07 07, 2011.]
http://webbook.nist.gov/chemistry/.

108. Die Klimaschutz Baustelle. [Online] [Cited: 08 29, 2011.] http://www.die-klimaschutz-baustelle.de/klimawandelzitate_energie.html.